



UNIVERSITY OF AMSTERDAM



MSc Physics and Astronomy
Track: Science for Energy and Sustainability

MASTER THESIS

Hyperuniform disordered light trapping for ultra-thin solar cells using substrate conformal imprint lithography

by

Alexander Lambertz

UvA-ID: 12795496

VU-ID: 2685923

August 31, 2021

60 ECTS

September 2020 - June 2021

Supervisors:

Dr. Esther Alarcon-Llado
Nasim Tavakoli

Examiners

Dr. Esther Alarcon-Llado



Declaration of Authorship

I, Alexander LAMBERTZ, declare that this thesis titled, "Hyperuniform disordered light trapping for ultra-thin solar cells using substrate conformal imprint lithography" and the work presented in it are my own. I confirm that:

- This work was done wholly or mainly while in candidature for a Msc degree at these Universities.
- Where any part of this thesis has previously been submitted for a degree or any other qualification at these Universities or any other institution, this has been clearly stated.
- Where I have consulted the published work of others, this is always clearly attributed.
- Where I have quoted from the work of others, the source is always given. With the exception of such quotations, this thesis is entirely my own work.
- I have acknowledged all main sources of help.
- Where the thesis is based on work done by myself jointly with others, I have made clear exactly what was done by others and what I have contributed myself.

Signed:

A handwritten signature in black ink that reads "Alex Lambertz". The signature is written in a cursive, slightly slanted style.

Alexander Lambertz

Date:

31-08-2021

UNIVERSITEIT VAN AMSTERDAM
VRIJE UNIVERSITEIT AMSTERDAM

Abstract

Physics and Astronomy
AMOLF

Master of Science

Hyperuniform disordered light trapping for ultra-thin solar cells using substrate conformal imprint lithography

by Alexander LAMBERTZ

Ultra-thin silicon-based photovoltaic technologies offer the prospect of saving beyond 90 % high-quality Si in comparison to conventional c-Si cells and modules, provided they can be supplied competitively in terms of cost and efficiency. As an indirect bandgap material, crystalline silicon absorbs light poorly especially in the near-infrared region, requiring absorbing layers many times thicker than amorphous Si or compound PV materials. Light-trapping structures applied to ultra-thin films mitigate transmission losses, yet add complexity to fabrication processes as they usually involve sub-micron features in order to reach short-circuit currents of thick devices.

In this work, hyperuniform disordered nanopatterns for light trapping were analyzed through theoretical and numerical methods and fabricated on free-standing ultra-thin silicon wafers and thinned IBC solar cells by means of substrate conformal imprint lithography. The hyperuniform platform offers unprecedented ability to tailor diffraction and was shown to outperform optimized periodic gratings in a series of FDTD simulations, where up to 68 % and 87 % solar absorbance at 1 μm - and 10 μm thickness were achieved, respectively. An existing coupled-mode theory approach to estimate absorption with hyperuniform light trapping was evaluated and further developed, which serves as a starting point for computer-based design optimizations. Three substrate conformal imprint lithography stamps with 4 cm^2 areas of different HUD designs were fabricated and used to imprint on substrates from (10-30) μm thickness as well as IBC solar cells. After etch-transfer of the imprint into the substrate, 80 % absorbance of solar irradiance in a 20 μm -thick silicon wafer even before the application of anti-reflective coatings was found. For the experimental work, a handling platform was developed that affords imprinting on fragile, ultra-thin substrates and facilitates bonding/debonding to and from arbitrary carriers.

The investigations furthermore revealed the robustness of hyperuniform patterns against fabrication imperfections, which was warranted through Fourier analysis of scanning-electron micrographs at different production stages and the developed techniques enable further processing of (patterned) ultra-thin substrates for surface passivation and anti-reflective coatings. The manufactured stamps are suitable for additional inquiries, such as patterning the anti-reflection layer or back-reflector, or can be used as a mask to grow or deposit nano particles with hyperuniform distribution, thus opening the door to plasmonic or resonant dielectric hybrid photonic materials with novel qualities.

Contents

Declaration of Authorship	iii
Abstract	v
1 Introduction	1
1.1 Background and motivation	1
1.2 Thin Film Solar Cells	2
1.3 Stealthy hyperuniform point patterns and networks	3
1.4 Scope and thesis outline	6
2 Light-trapping in thin substrates	9
2.1 Electromagnetic theory of waveguides	9
2.1.1 Maxwell's and the wave equation	9
2.1.2 Total internal reflection	10
2.1.3 Waveguided modes of a (silicon) slab in air	11
2.2 Coupled-mode theory approach for HUD light trapping	13
2.3 Numerical methods and FDTD simulation	20
2.3.1 Python script for calculating waveguided modes of a triple-layered stack	21
2.3.2 Dispersion diagram of a slab of silicon	23
2.3.3 Full-wave 3D simulation of HUD patterned absorber	23
2.4 Results and Discussion	25
3 Manufacturing hyperuniform patterns substrates	33
3.1 Thin wafer handling systems	33
3.2 Master fabrication with electron-beam lithography	36
3.3 Stamp fabrication	42
3.4 Preparation of samples and SCIL imprint	43
3.5 Reactive-ion etching for pattern transfer	45
3.6 Removal of residual imprint-resist layers	47
3.7 Results and Discussion	47
4 Conclusion & Outlook	55
Acknowledgements	58
Bibliography	59
A Mode solver and absorption with HUD-patterns	67
B Step-by-Step from Bonding to Patterned Devices	75
C Analysis of SEM images	83

Chapter 1

Introduction

The aim of this work is to enable fast fabrication of hyperuniform disordered (HUD) large-area nanostructures on ultra-thin silicon substrates as well as thinned IBC solar cells, facilitate their characterization and further to investigate hyperuniform light trapping from a theoretical and numerical standpoint. This introductory chapter reviews the current situation, builds motivation for developing high-efficiency ultra-thin c-Si solar cells, makes acquaintance with hyperuniform patterns and networks, and finally gives an outline of the thesis.

1.1 Background and motivation

Development of direct solar energy conversion technologies through photovoltaic cells and modules has increased substantially in the past decades, because they can help replace fossil fuels as an energy source and thereby contribute to a reduction of greenhouse gas (GHG) emissions. The link between the global use of fossil fuels, atmospheric GHG concentrations, and climate change has been recognized by the Intergovernmental Panel on Climate Change (IPCC) [1] and the goal set in the Paris agreement [2] requires all participating nations to increase their efforts in renewable energy production. In a sustainable development scenario, electricity production from photovoltaic technologies is projected to increase more than fourfold from 2019 to 2030 [3], which requires higher cell efficiencies, lower module costs as well as an increase in surface area used for PV installations [4].

From 2010 to 2020, the rise of installed solar energy capacity from about 40 GW to more than 700 GW [5] has significantly changed the land- and cityscape with PV panels being installed mainly on rooftops of private and commercial buildings and large solar parks built in areas previously unused or used for other purposes [6]. While efforts to meet the Paris agreement still need to increase, public opinion about the change of landscape by renewable energy technologies has already become an opposing force in some regions [7][8][9].

Since many more sun-exposed surfaces need to be covered with PV panels, besides efficiency their implementability in areas where they do not compete with other applications needs to increase, while their perceptibility and cost need to reduce substantially.

Thin-film solar cells can potentially tackle all of these challenges as they offer flexibility, (partial) transparency and integrability, all-the-while using less material and offering capability for high-throughput fabrication. Due to their thinness, lower-grade substrates can be used without jeopardizing the open circuit voltage [10] and "bottom-up" techniques to grow silicon *in situ* are on their way to become economically feasible [11][12].

1.2 Thin Film Solar Cells

Thin film solar cells currently lack behind their thick counterparts in both price and efficiency [13]. The lower efficiency can be explained by incomplete absorption of incident radiation in the thin absorbing layers. Fig. 1.1 shows the short-circuit current (J_{sc}) versus absorber thickness for the popular thin-film technologies, Copper Indium Gallium (di)Selenide (CIGS), Cadmium Telluride (CdTe), amorphous- (α -Si), and crystalline silicon (c-Si). The short-circuit current density is computed from

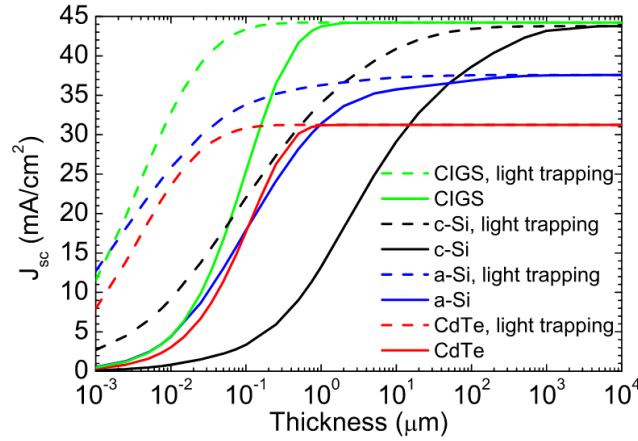


FIGURE 1.1: Short-circuit current J_{sc} as a function of absorber thickness in semi-log scale. Different absorber materials are denoted by color, where green corresponds to CIGS (Copper Indium Gallium Selenide), black and blue to crystalline- and amorphous silicon, respectively, and red to CdTe (Cadmium Telluride). Solid lines represent single pass values of J_{sc} , while dashed lines correspond to the lambertian light-trapping limit. Reprinted from [14].

the rate of photons delivered to the earth's surface with energies above the bandgap of the respective materials, where each collected photon is assumed to contribute the charge of one electron to the current density through its absorption. The solid lines in fig. 1.1 correspond to short-circuit current densities versus thickness for a single pass of incident light, while the dashed lines represent the lambertian limit of J_{sc} against thickness, which assumes a homogeneous angular distribution of light upon its entry into the absorbing layer. In the case of c-Si (black lines), the difference in short-circuit current between single-pass absorption and lambertian limit is substantial for thicknesses between 0.1 μm and 100 μm , indicating that effective light-trapping can afford a significant thickness reduction accompanied by only a minute J_{sc} decrease.

Despite many parties being involved in research and fabrication nano-textured ultra-thin silicon solar cells on a laboratory scale, with reported cells reaching a J_{sc} of 25.3 mA cm^{-2} at 2.75 μm thickness [15], (29.0-34.5) mA cm^{-2} at 10 μm thickness [16][17], or 37.8 mA cm^{-2} at 43 μm thickness [18], the performance of actual devices in general falls far below the values obtained from numerical results, as compared in fig. 1.2 below. Most real devices shown in fig. 1.2 are located close to the single pass reference with only three surpassing the double pass limit up to a thickness of 10 μm , all of which stay far below the lambertian limit corresponding to their thickness. The numerical results, on the other hand, are seen to exceed even the lambertian limit in some cases. This discrepancy highlights the difficulty of fabricating ultra-thin solar

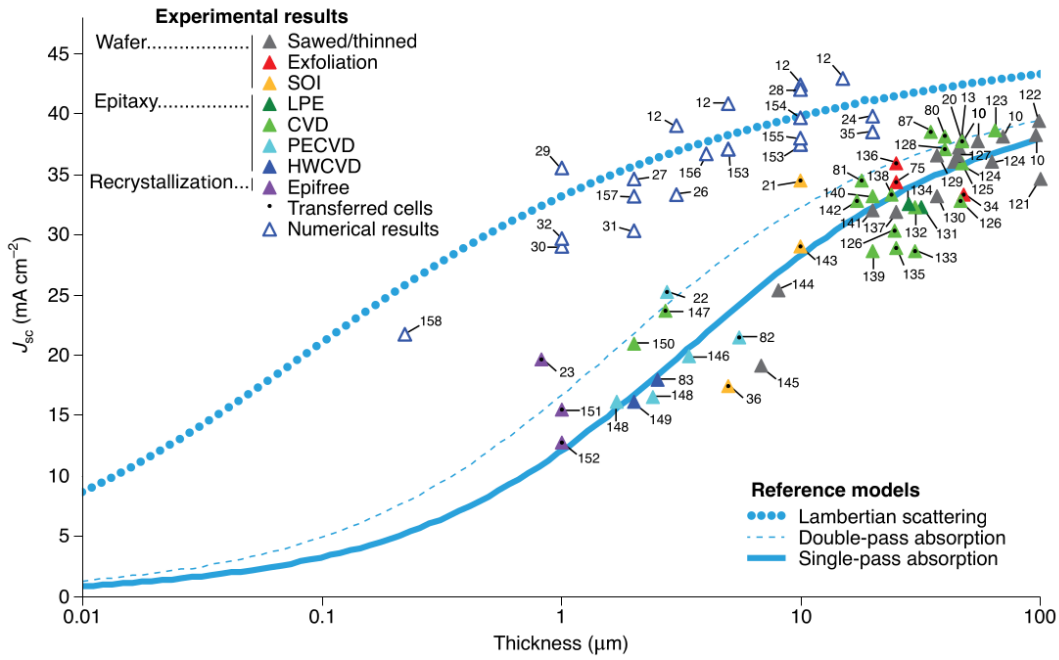


FIGURE 1.2: Short-circuit current of state-of-the-art thin-film crystalline silicon solar cells versus absorber thickness. Numerical results are shown as hollow symbols and actual devices as filled triangles with color denoting their method of fabrication. The blue lines correspond to single pass- (solid), double pass- (dashed), and lambertian (dotted) absorption limits. Adapted from [19].

cells with light trapping schemes, which do not penalize the short-circuit current by e.g. added series resistance or increased surface- or interface recombination. The record short-circuit current cited above were all achieved using either periodic or random nanostructures to trap incident light, though investigations have led to the conclusion that periodic patterns with a certain degree of correlated disorder are able to trap light more efficiently than either purely periodic or random texturing [20]. Arising as a special case of disordered materials, the hyperuniform disordered patterns tested in this work present a range of interesting qualities, which are explained in more detail in the following section.

1.3 Stealthy hyperuniform point patterns and networks

Discovered quite recently in 2003, peculiarities of hyperuniform disordered (HUD) states of matter have been recognized by disciplines besides physics, including polymeric chemistry [21] and biological tissues [22]. Disordered hyperuniformity is similar to crystal structures, since neither exhibit large-scale density fluctuations, yet the Bragg-peaks associated with the order in crystals are absent in HUD structures, such that they share similarities also with amorphous materials like liquids or glasses [23] [24][25]. The hyperuniform arrangement thus presents itself as an underlying, or hidden order state in-between the limiting cases of a perfect crystal and a totally random system as a Poissonian point distribution. Since the discovery of hyperuniformity in the distribution of photo-receptors in the eyes of a chicken [26], many more natural systems have been found to exhibit similar properties, including the

density-fluctuations in the early universe [27], jammed hard-particle packing problems [28], organization of adapted immune systems [29], and amorphous cellular geometries [30].

The hyperuniform state can mathematically be described by an ensemble-averaged structure factor $S(\vec{k})$ of infinite point configurations in a d -dimensional Euclidean space with the following form [26]:

$$S(\vec{k}) = 1 + \rho \tilde{h}(\vec{k}) , \quad (1.1)$$

where ρ denotes the number density and $\tilde{h}(\vec{k})$ the Fourier-transform of the total correlation function $h(\vec{r}) = 1 - g_2(\vec{r})$, with pair-correlation function $g_2(\vec{r})$ of the system, which depends only on the radial distance $\vec{r} \equiv r$ and number-density ρ for statistically homogeneous and isotropic systems. Furthermore, the forward scattering contribution to the diffraction pattern is discarded in the definition of (1.1). In case $S(\vec{k}) = 0$ when $|\vec{k}| \rightarrow 0$, the ensemble classifies as hyperuniform, which is equivalent to the statement that infinite-wavelength fluctuations vanish.

By imposing further constraints on the structure factor, (sub-)classes of hyperuniform arrangements with peculiar properties are found, for example super-ideal gases with $S(\vec{k}) = 1$ or stealth-materials with $S(\vec{k}) = 0$ for a set of wavevectors \vec{k} [31]. In particular, the stealthy-hyperuniform ensembles, where the structure factor vanishes for a range of k -vectors below some critical value k_c , or $S(\vec{k}) = 0 \forall k \in [0, k_c]$, have many applications in (optical) science and nanophotonics, since they offer complete and isotropic photonic bandgaps with tunable properties [32]. These applications include waveguides, optical (resonant) modulators, couplers and insulators [31][32], directional LEDs [33], lenses [34], as well as light-trapping in solar cells presented in this thesis.

The hyperuniform designs under investigation belong to the stealthy hyperuniform class and were reported before in an article currently in review [35]. They are classified by their targeted structure factor, which can be described by a gate function that equals one only when $k \in [k_1, k_2]$, and zero for other k -vectors. Since both k_1 and k_2 are positive, real numbers, $k_1 = k_c$ denotes the critical wavevector value of stealth-materials below which the structure factor vanishes, while in the interval $[k_1, k_2]$ the structure acts as a super-ideal gas with $S(k) = 1$. For a structure factor of this kind, one may define a so-called "stealthiness parameter" $\chi = k_1/k_2$, which indicates the fraction of wavevectors for which $S(k)$ vanishes. In the following, k_1 and k_2 will be called the "characteristic HUD numbers", since they classify a hyperuniform distribution with a specified structure factor, whose intensity is (ideally) limited to wavevectors of certain $k \in [k_1, k_2]$. A hyperuniform point-distribution exhibiting these properties is obtained by an iterative algorithm that probes point-to-point correlations in a configuration previously obtained from for example a periodic- or random starting distribution. The algorithm then corrects the pair-correlations according to the desired structure factor by computing the photonic band structure through a plane-wave expansion method [25][31][32][36]. After a few iterations, a hyperuniform disordered point pattern is obtained and upon placing cylinders of a certain radius at the positions of the points, a binary material with one element or compound comprising the cylinders and another as the background material is obtained.

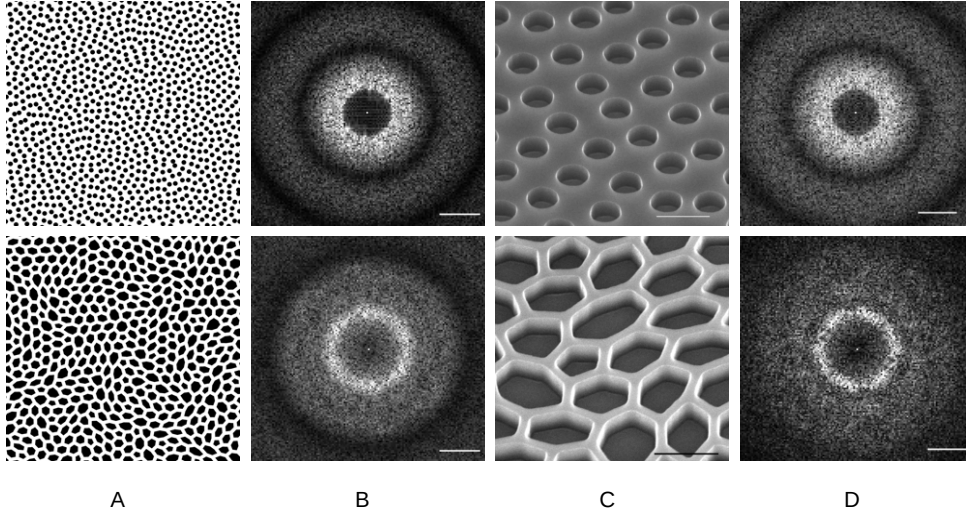


FIGURE 1.3: Two of the hyperuniform disordered structures under investigation. The top row shows a hyperuniform point-pattern, where **A** visualizes $(10 \times 10) \mu\text{m}^2$ of the design, **B** the momentum-space image of the design, **C** a scanning electron-microscope image of the design fabricated on silicon, **D** Fourier-transformed image of the fabricated sample. The bottom row shows a hyperuniform wall-network as designed **A**, its Fourier-transform **B**, the design fabricated on silicon **C**, and again a k-space image of the same in **D**. The scale bars in **B** & **D** are $10 \mu\text{m}^{-1}$ and 500 nm in **C** and the brightness of the Fourier-space images has been normalized to the shown regions.

The top row in fig. 1.3 shows the HUD point pattern and corresponding momentum-space image, as well as a tilted scanning electron-microscope image of the structure fabricated on a silicon sample with electron-beam lithography and a Fourier-transform of a $(10 \times 10) \mu\text{m}^2$ area of the sample.

A hyperuniform wall-network, shown in the lower row of fig. 1.3, can be obtained from a HUD-point pattern by employment of a Delaunay's-triangulation tessellation protocol [37][38]. Starting point for the hyperuniform algorithm in this case is a regular triangular lattice, from which a HUD-distribution with characteristic numbers k_1, k_2 is generated. The wall-network resembles a distorted honeycomb structure and possesses interesting photonic properties, such as a large TE-polarization bandgap, whose center frequency is tunable by the thickness of the walls [38].

Another way of obtaining hyperuniform disordered patterns is inspired by spinodal decomposition, as observed in the separation of a single-phase fluid or solid solution into two phases [39]. The spinodal configuration can be described by a superposition of sine-waves with fixed wavenumber(s) but random amplitudes, phases and orientations [40]. By deliberately choosing a range of wavevectors $k_1 \leq k \leq k_2$ for the sine-waves and dispersing them for example on a 2D-plane with random phases, amplitudes and orientations, a pattern with the desired structure factor is automatically obtained. If the amplitude is represented as height in this example, setting a height threshold will allow the generation of a binary system with almost arbitrary filling-fraction [41].

The spinodal structure generated this way for [35] and under investigation here is visualized in the top row of fig 1.4. It should be noted that a spinodal pattern of this

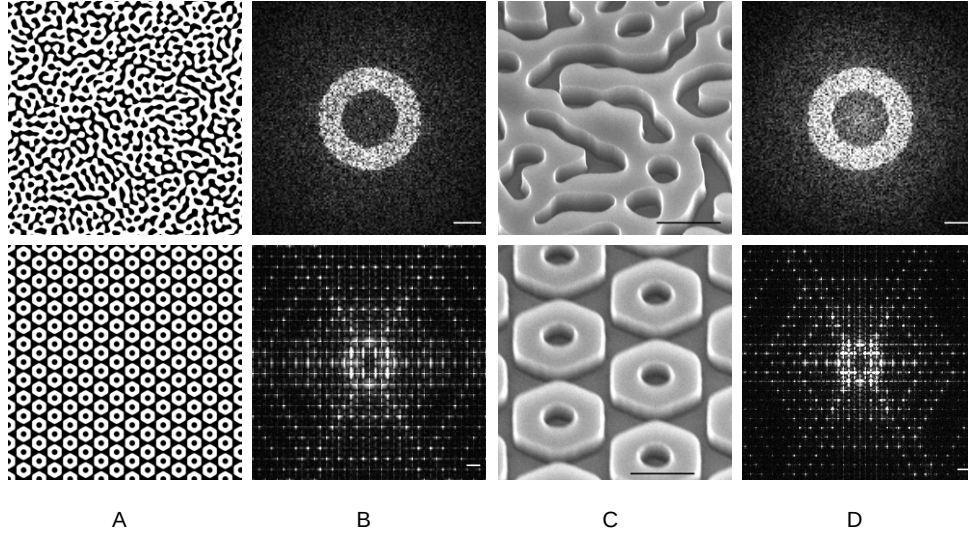


FIGURE 1.4: A spinodal (top row) and an optimized periodic structure (bottom row) are shown. **A** visualizes $(10 \times 10) \mu\text{m}^2$ of the design in real-space, **B** the same in momentum-space, **C** a scanning electron-microscope image of the design fabricated on silicon, **D** Fourier-transformed image of the fabricated sample. The scale bars in **B** & **D** are $10 \mu\text{m}^{-1}$ and 500 nm in **C** and the brightness of the Fourier-space images has been normalized to the shown regions.

kind is not strictly stealthy-hyperuniform, but retains some residual intensity below the critical wavevector value k_1 . Also shown in the same figure in the bottom row is an optimized periodic structure, which is compared to the three hyperuniform designs besides an unpatterned reference case. All of the designs were generated by the 'Theoretical Nanophotonics and Quantum Optics Group' under Dr.M. Florescu at Surrey University [42] and made available for the use in this work.

1.4 Scope and thesis outline

The nanopatterns presented in the previous chapter have been manufactured on a suspended $1 \mu\text{m}$ -thick silicon membrane in fields of $(100 \times 100) \mu\text{m}^2$ or $(150 \times 150) \mu\text{m}^2$ using electron-beam lithography. After infiltrating the exposed valleys with a polymeric resist (refractive index $n=1.52$) acting as an anti-reflective coating, an absorbance beyond 65 % under AM1.5G [43] illumination was experimentally confirmed [35]. In order to implement this improvement of almost 60 % over an unpatterned slab¹ in a high-throughput industrial fabrication process, for example in roll-to-roll [44][45] or roll-to-plate [46], a faster route for obtaining these structures not relying on electron-beam lithography needs to be found.

The goal of this project can be summarized as in the following research questions:

¹Absorbance of a $1 \mu\text{m}$ -thick, unpatterned slab with anti-reflective coating and silver back-reflector is simulated in ch. 2, fig. 2.16.

How can centimeter-scale hyperuniform patterns be obtained quickly on thin, fragile substrates and their characterization facilitated, and what is the measured and simulated absorbance enhancement over an unpatterned reference case?

In the course of addressing the main concerns, also the following sub-questions are answered:

- How does the choice of HUD-pattern parameters influence the expected absorption?
- What limits complete absorption in ultra-thin Si-layers with HUD structures?
- How can thin substrates be safely handled and made ready for texturing?
- Are patterns produced with substrate conformal imprint lithography equivalent to those obtained through electron-beam lithography?
- Is the fast fabrication technique suitable for post-processing thinned commercial solar cells?

The following is organized in three chapters, in which these sub-questions are answered chronologically. Chapter 2 contains theoretical and numerical considerations and calculations, where an approach from coupled-mode theory is refined and further developed to obtain absorption estimates for HUD patterned slabs, which are experimentally analyzed through a series of FDTD simulations. Chapter 3 focuses on fabricating actual devices, for which a thin-wafer handling platform is developed and stamps featuring HUD structures are produced, which in turn are used to imprint on thin silicon slabs and thinned-down commercial IBC cells and the patterns are transferred into the absorbing layers by reactive-ion etching. The conclusion in chapter 4 combines and contrasts the results from ch. 2 and 3 and gives an outlook to the prospective performance of a full device, supplemented with suggestions for further improvements and investigations.

Chapter 2

Light-trapping in thin substrates

In this chapter, the absorption of light in a thin, hyperuniformly patterned slab of silicon is approximated via coupled-mode theory and experimentally validated through finite-difference time-domain (FDTD) simulation. Beginning with a short introduction to electromagnetic theory in sec. 2.1.1, the phenomenon of total internal reflection described in sec. 2.1.2 is followed by the classification of waveguides and waveguided modes sec. 2.1.3. A coupled-mode theory approach for estimating the limit of absorption in a slab is presented in sec. 2.2, which utilizes waveguided mode data obtained through numerical computation via an algorithm proposed in sec. 2.3.1 as well as a commercial finite-difference eigenmode solver in sec. 2.3.2. Following a series of FDTD simulations of absorbance in slabs featuring different (HUD-) patterns and thicknesses in sec. 2.3, the results from individual sections are compared and discussed in sec. 2.4.

2.1 Electromagnetic theory of waveguides

2.1.1 Maxwell's and the wave equation

The propagation of electromagnetic waves in vacuum and matter is described by Maxwell's equations. In the absence of free charge- ($\rho = 0$) and current- ($\vec{j} = 0$) densities, they can be simplified to (2.1-2.4) [47]:

$$\vec{\nabla} \cdot \vec{E} = 0, \quad (2.1)$$

$$\vec{\nabla} \cdot \vec{B} = 0, \quad (2.2)$$

$$\vec{\nabla} \times \vec{E} = -\frac{\partial}{\partial t} \vec{B}, \quad (2.3)$$

$$\vec{\nabla} \times \vec{B} = \frac{\partial}{\partial t} \vec{E}, \quad (2.4)$$

where \vec{E} , \vec{B} denote the electric field and magnetic flux density, respectively, and c the speed of light in vacuum [47].

Inside of a medium, (2.4) takes on a different form in order to include the response of the material (i.e. polarization, magnetization, induced currents) to the propagation of electromagnetic waves:

$$\vec{\nabla} \times \vec{H} = \frac{\partial}{\partial t} \vec{D}, \quad (2.5)$$

where the relation between the magnetic field \vec{H} and magnetic flux density \vec{B} , and the relation between the electric field \vec{E} and the electric flux density \vec{D} , for a lossless, linear, homogeneous, and isotropic medium are given by:

$$\vec{D} = \epsilon_r \vec{E}, \quad (2.6)$$

$$\vec{B} = \mu_r \vec{H}. \quad (2.7)$$

Here, $\epsilon_r = \epsilon/\epsilon_0$ and $\mu_r = \mu/\mu_0$ denote the relative permittivity and permeability of the medium, respectively. From (2.5), (2.6) and (2.7), the wave equation below is obtained, as shown in detail in appendix A:

$$\nabla^2 \vec{E} = \frac{\epsilon_r \mu_r}{c^2} \frac{\partial^2}{\partial t^2} \vec{E}, \quad (2.8)$$

where the fraction $\epsilon_r \mu_r / c^2$ denotes the inverse square of the phase velocity v^{-2} of the wave in the medium, which may equivalently be expressed with the refractive index $n = \sqrt{\epsilon_r \mu_r} = c/v$ [48]. A solution for (2.8) is given by the plane wave equation:

$$\vec{E}(\vec{x}, t) = \vec{E}_0 \exp \left[i \left(\vec{k} \vec{x} - \omega t \right) \right], \quad (2.9)$$

where the wavevector $\vec{k} = n \cdot \vec{k}_0$, with free space wavevector $k_0 = 2\pi/\lambda$ and wavelength λ . Inserting (2.9) into (2.8) yields the dispersion relation:

$$|\vec{k}|^2 = \frac{\omega^2}{v^2} = \frac{n^2 \omega^2}{c^2}. \quad (2.10)$$

The wavevector $k = 2\pi n/\lambda$ indicates the phase-change of the wave with respect to distance in the medium, similar to ω representing the temporal change of phase.

2.1.2 Total internal reflection

A difference in the refractive index n of two dissimilar materials can give rise to the phenomenon of total internal reflection at their mutual boundary, by which the transmission of an electromagnetic wave through the interface is inhibited and only reflection takes place. For a wave in a medium A with refractive index n_A interfaced with medium B of n_B and in case of $n_A > n_B$, there exists an angle θ_c between the normal of the interface and wave's plane of incidence, at which Snellius' law of refraction in (2.11) becomes an inequality,

$$n_A \sin(\theta_A) = n_B \sin(\theta_B) \quad (2.11)$$

$$\rightarrow \theta_c \geq \arcsin \frac{n_A}{n_B}.$$

For all angles $\theta > \theta_c$ the wave experiences total internal reflection and becomes confined to the material with greater refractive index, which is therefore termed waveguide. The reflected portions of the incident amplitudes r are calculated using Fresnel's equations, given in (2.12) and (2.13), and depend on the orientation of electric and magnetic field-vectors with respect to the interface [48]:

$$r_{TE} = \frac{n_1 \cos \phi_1 - n_2 \cos \phi_2}{n_1 \cos \phi_1 + n_2 \cos \phi_2}, \quad (2.12)$$

$$r_{TM} = \frac{n_2 \cos \phi_1 - n_1 \cos \phi_2}{n_2 \cos \phi_1 + n_1 \cos \phi_2}, \quad (2.13)$$

where the subscript TE/TM denotes an orthogonal polarization of the electric/-magnetic field at the interface, respectively. With Snellius' equation (2.11), they can equivalently expressed as:

$$r_{\text{TE}} = \frac{n_1 \cos \phi_1 - \sqrt{n_2^2 - n_1^2 \sin^2 \phi_1}}{n_1 \cos \phi_1 + \sqrt{n_2^2 - n_1^2 \sin^2 \phi_1}}, \quad (2.14)$$

$$r_{\text{TM}} = \frac{n_2 \cos \phi_1 - n_1 \sqrt{n_2^2 - n_1^2 \sin^2 \phi_1}}{n_2 \cos \phi_1 + n_1 \sqrt{n_2^2 - n_1^2 \sin^2 \phi_1}}. \quad (2.15)$$

If ϕ_1 exceeds the critical angle, the expressions inside the roots become negative and $|r| \equiv 1$, while r is a real fraction $0 < r < 1$ for angles smaller than the critical value. Since r is complex in case of total internal reflection, a phase-shift Φ of the reflected wave occurs, which can be expressed by [49]:

$$\Phi_{\text{TE}} = 2 \tan^{-1} \frac{\sqrt{\sin^2 \phi_1 - \left(\frac{n_2}{n_1}\right)^2}}{\cos \phi_1}, \quad (2.16)$$

for TE polarization and for TM

$$\Phi_{\text{TM}} = 2 \tan^{-1} \frac{\sqrt{\frac{n_1^2}{n_2^2} \sin^2 \phi_1 - 1}}{\frac{n_2}{n_1} \cos \phi_1}. \quad (2.17)$$

A totally internally reflected wave is termed a *standing wave*, if its phase is the same at periodic positions inside the waveguide. The *boundary conditions* for standing waves may be satisfied by multiple combinations of frequency and propagation angles inside a waveguide, giving rise to the *modes* of a waveguide, which will further be explained by example of a symmetrical waveguide in air.

2.1.3 Waveguided modes of a (silicon) slab in air

Consider a dielectric medium, infinite in both x and z , and of height h in the direction of y , surrounded by air for all $|y| > h/2$ as depicted in fig. 2.1(a). For a wave propagating in the z -direction inside the waveguide with its normal field vectors oriented at an angle θ towards the interface. The portion of the field in the y -direction is bound by total internal reflection, the boundary condition for the y -component of the field, defined in fig. 2.1(b) as $k_y = k_0 n_1 \cos(\theta)$, is deduced as follows:

Starting from the lower interface, the wave travels a distance of h to the upper interface and experiences a phase change of $\phi_t = k_y h = k_0 n_1 \cos(\theta) h$ during propagation. The total internal reflection at the interface induces a phase change ϕ_i , given by the Fresnel coefficients (2.16-2.17). After reflection at the upper boundary, another distance h is covered towards the lower interface and upon the second reflection and corresponding phase change ϕ_i there, one period is completed and the starting condition recovered. If the total phase change corresponding to a period is an integer multiple m of 2π , the boundary condition

$$2\pi \cdot m = 2\phi_t + 2\phi_i \quad (2.18)$$

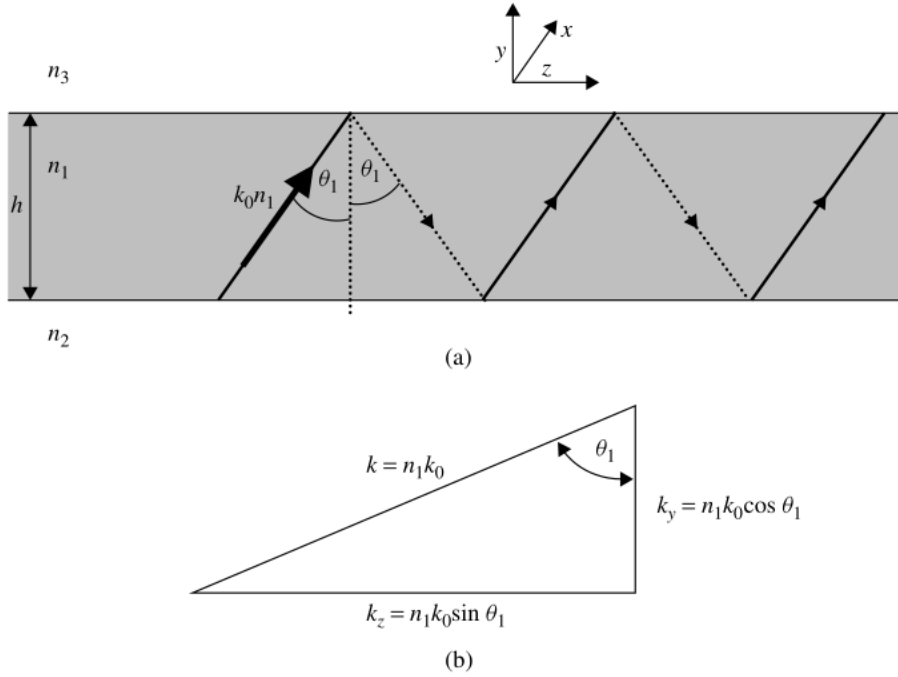


FIGURE 2.1: **a)** Planar waveguide (grey) with refractive index n_1 in air ($n_2 = n_3 = 1$). The free-space wave vector k_0 becomes $k = k_0 \cdot n_1$ inside the waveguide and the wave propagates at an angle θ_1 relative to the normal of the air-waveguide interfaces. **b)** The wavevector $k = n_1 k_0$ is split into two mutually orthogonal parts, $k_z = k \sin \theta_1$ parallel to the interface and $k_y = k \cos \theta_1$ normal to it. Adapted from [49].

is satisfied and a standing wave confined to the waveguide is observed.

Such waves are termed *modes* with mode number m , where the projection of wavevector k inside the waveguide onto the interface $k_z = k_0 n_1 \sin \theta_1$ is known as the propagation constant β . Also referred to as the mode's wavevector k_m , $k_m = \beta = k_z = k_0 n_1 \sin(\theta_1)$ is an invariant for a wave across all layers in a multi-layer structure [50]. A *mode* is also said to have an effective refractive index $n_m = n_1 \sin(\theta_1)$, such that

$$k_m = \beta = k_0 n_m = k_0 n_1 \sin(\theta_1). \quad (2.19)$$

The modes of a waveguide are further classified by their polarization. Since the phase shift ϕ_i experienced by a wave upon reflection at an interface depends on the orientation of the electric and magnetic field vectors relative to that interface, solutions to the boundary condition are slightly different if the electric field is oriented parallel or perpendicular to the plane of incidence. From the preceding, it becomes clear that only a finite number of modes exist for a wave of frequency ω in such a system, with the highest mode number found through the critical angle θ_c :

$$m_{\max} = \left[\frac{k \cos \theta_c}{\pi} \right]_{\text{int}}, \quad (2.20)$$

with wavevector $k = \frac{\omega}{c} n$ and where the highest mode number m_{\max} is given as the largest integer number that is smaller than the right-hand side expression, indicated by the brackets with subscript "int".

So far, only the ray-optical approach was utilized to arrive at the eigenvalue

equation (2.18). The form of this equation can be validated through solving the wave equation (2.8), which is shown in appendix A.

The absorption coefficient

In absorptive media, the refractive index is in fact a complex number $\tilde{n} = n + i\kappa$, of which the real part corresponds to the ‘normal’ refractive index n and the imaginary part κ denotes the extinction coefficient according to Beer-Lambert’s law [51]:

$$\left(\frac{dE}{dz}\right)^2 = \frac{I}{I_0} = \exp[-2k_0\kappa z] = \exp[-\alpha z], \quad (2.21)$$

where the absorption coefficient $\alpha = 2k_0\kappa$ was introduced. As a consequence of the complex refractive index in absorptive media, also the wavevector becomes complex:

$$\tilde{k} = k' + ik'' = \frac{2\pi n}{\lambda} + i\frac{2\pi\kappa}{\lambda}. \quad (2.22)$$

Let us reconsider the propagation constant β for the complex case.

$$\tilde{\beta} = k'_z + ik''_z = \beta + i\frac{\alpha_z}{2} = k_0 n_1 \sin \theta_1 + ik''_z.$$

From the sketch in fig. 2.1b, it is evident that the distance d travelled by the wave per unit length in z is given by $d(z) = z/\sin(\theta_1)$, such that the imaginary part of the mode’s effective refractive index should also depend on the propagation angle and thus the actual distance travelled per unit length in z . Similar to N , an effective extinction coefficient K can be defined as:

$$K = \kappa / \sin \theta_1,$$

and consequentially

$$k''_z = k_0 K = k_0 \frac{\kappa}{\sin \theta_1} = k_0 \frac{n}{N} \kappa.$$

The implication of the above is that absorption is increased as the angle of incidence becomes smaller, i.e. if $\beta \rightarrow k_0$. On the other hand, since the confinement-factor η of the mode to the waveguide given in (2.23) also decreases as the angle of incidence becomes smaller, it has been suggested [52] that especially in the case of thin waveguides, the absorption coefficient of the waveguide $\alpha_{\text{wg}} = \alpha \cdot \eta$. If $2k_0\kappa$, $2k_0K$, or α_{wg} better approximate the modes’ attenuation will be assessed when comparing the mode profiles with those found via finite-difference time-domain simulation in sec. 2.4.

$$\eta = \frac{\int_{-\frac{h}{2}}^{\frac{h}{2}} E_x(y) dy}{\int_{-\infty}^{\infty} E_x(y) dy} \quad (2.23)$$

2.2 Coupled-mode theory approach for HUD light trapping

The dominant strategy for enhancing absorption in thin substrates is to couple incident light to the quasi-guided modes of the structure and thereby greatly enhance

the optical path length in the absorber [53][54]. In the previous section 2.1.3, the phenomenon of total internal reflection was shown to give rise to waveguided modes and an algorithm for obtaining the mode characteristics was introduced. The presence of a diffractive grating on one or more surfaces of the waveguide renders certain portions of the guided modes excitable by normally incident radiation. These portions are referred to as guided resonances [55]. The absorption spectrum of a single guided resonance of a waveguide is given in (2.24), which is taken from the "Coupling of modes" chapter from Hermann Haus' book on optoelectronics [56] and modified by Yu, Raman, and Fan [57]:

$$a(\omega) = \frac{\gamma_i \gamma_e}{(\omega - \omega_0)^2 + (\gamma_i + N\gamma_e)^2 / 4}, \quad (2.24)$$

with excitation frequency ω and where γ_i describes the intrinsic loss rate due to absorption by the material, γ_e the leakage rate to free-space channels outside the absorber, ω_0 the frequency of the resonance, and N the number of channels that are coupled with coupling rate γ_e , which is assumed equal for all N channels.

Integration of the spectrum yields the spectral cross-section (2.25), which carries the unit of frequency,

$$\sigma = \int_{-\infty}^{\infty} a(\omega) d\omega. \quad (2.25)$$

The interpretation of (2.25) given by Yu et al is as follows: "For an incident spectrum with bandwidth $\Delta\omega \gg \sigma$, a resonance contributes an additional $\sigma/\Delta\omega$ to the spectrally-averaged absorption coefficient." [57].

Assuming weak variation of γ_i and γ_e in the frequency interval $[\omega, \omega + \Delta\omega]$, integration of (2.24) yields

$$\sigma = \frac{2\gamma_i \gamma_e}{N\gamma_e + \gamma_i} \arctan \left[\frac{2(\omega - \omega_0)}{N\gamma_e + \gamma_i} \right]_{-\infty}^{\infty} = \frac{2\pi\gamma_i \gamma_e}{N\gamma_e + \gamma_i}, \quad (2.26)$$

since the value-space of arctan is limited to $(-\frac{\pi}{2}, \frac{\pi}{2})$. The right-hand term can be rearranged to obtain:

$$\sigma = \frac{2\pi\gamma_i}{N + \frac{\gamma_i}{\gamma_e}} \approx \frac{2\pi\gamma_i}{N}, \quad (2.27)$$

where the approximation is valid when either $\gamma_e \gg \gamma_i$, as in the overcoupling regime [57], or if the number of channels $N \gg \gamma_i/\gamma_e$.

In order to obtain the cumulative absorption from all resonances in the frequency range, a summation over the individual contributions σ is performed and the result normalized by the incident spectral bandwidth $\Delta\omega$,

$$\bar{A} = \sum_m \frac{\sigma_{\max}}{\Delta\omega} = \frac{1}{\Delta\omega} \sum_m \frac{2\pi\gamma_{i,m}}{N_m}. \quad (2.28)$$

(2.28) has been considered and applied to obtain an estimation for absorption for photonic devices and thin-film solar cells [52][58][59][60]. The following passage considers the ramifications of employing hyperuniform texturing instead of periodic gratings considered in [57].

The absorption spectrum in the vicinity of a guided resonance of a hyperuniform pattern is not necessarily in the form of a sharp Lorentzian as in case of a periodic array, but rather forms a band delimited by the characteristic values k_1, k_2 of the

HUD pattern employed as seen in fig. 2.2. For a periodic grating of distance parameter a , one would find the guided resonances at the intersections of the mode bands with horizontal lines that are equally distributed with a $2\pi/a$ -spacing. With a hyper-

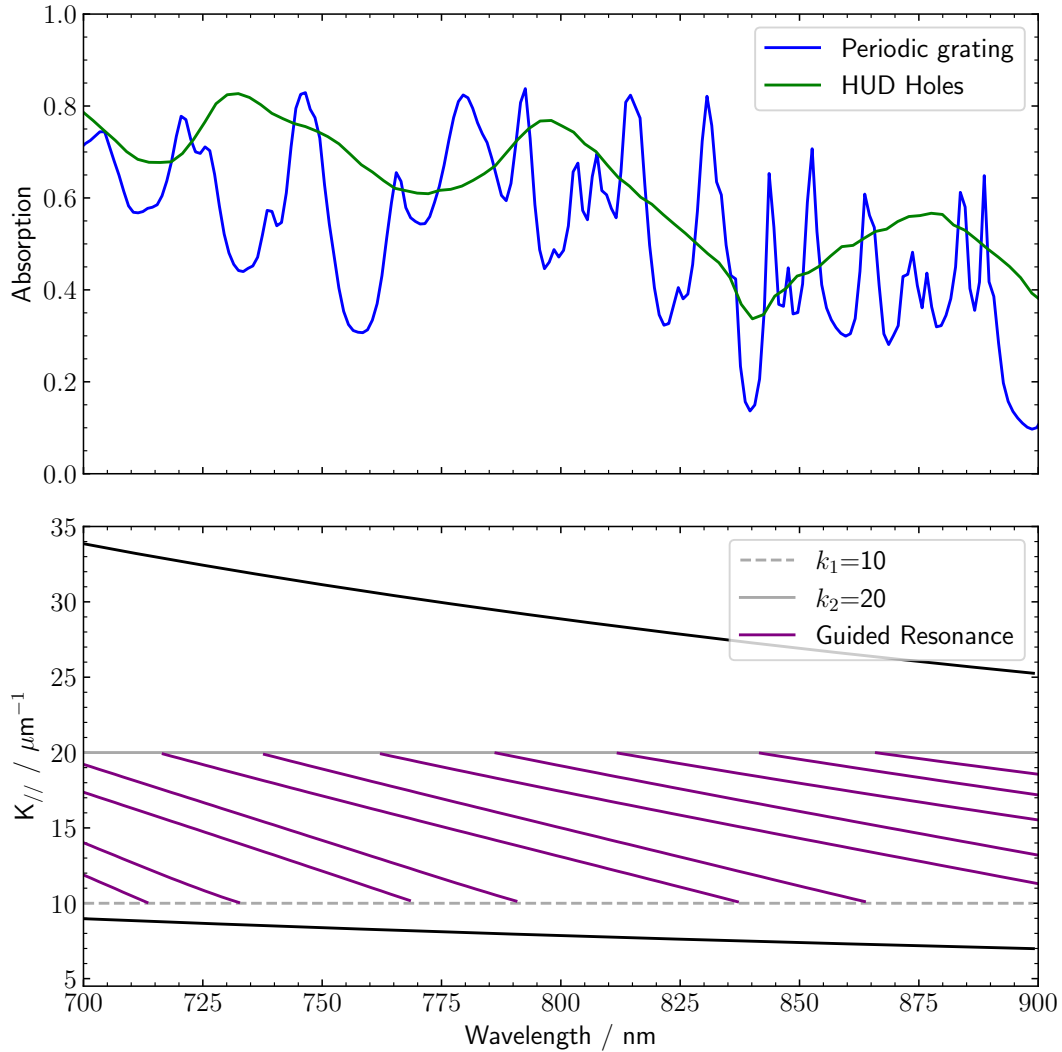


FIGURE 2.2: Upper graph: Comparison of the absorption-spectrum between a periodically grating- and a hyperuniformly patterned $1\text{ }\mu\text{m}$ slab of silicon for the wavelength range $[700,900]\text{ nm}$, obtained through FDTD-simulation in sec. 2.3. Lower graph: Guided resonance-portions of the guided modes with exemplary HUD characteristic values k_1 and k_2 of 10 and 20, respectively. These are calculated for a $1\text{ }\mu\text{m}$ slab of silicon with using a finite-element mode solver as explained in sec. 2.3.2. The ruler denotes a spectral width Δk_m of an arbitrarily chosen guided resonance m . The upper/lower black curves represent the dispersion-relation in silicon/air, respectively.

runiform grating, the nature of the resonances is no longer fully discrete, but instead they appear as sub-bands of the mode dispersion diagram. From the preceding, an equivalent phenomenon is expected in gratings featuring random roughness, which are understood as periodic structures where parameter $a \rightarrow \infty$ [61].

The **number of resonances** M per guided resonance m in the frequency interval $[\omega, \omega + \delta\omega]$ is found through considering an in-plane isotropic dispersion relation $\omega = c_0 k_0 n_m$. The resonances with $k = k_0 n_m$ form a ring in the two-dimensional $k_{//}$ -space of radius $k_0 n_m$ and width $\delta\omega$, where for a sample area $L \times L \gg \lambda^2$ each resonance occupies an area of $\Delta k^2 = (\frac{2\pi}{L})^2$ [62]. Note that only one resonance in the orthogonal direction k_{\perp} is assumed, since the thickness of the slab is in the order of wavelength λ . The number of resonances per guided resonance is then given as:

$$M_m = \frac{2\pi\omega n_m^2}{c_0^2} \frac{L^2}{(2\pi)^2} \delta\omega, \quad (2.29)$$

and the total number from all guided resonances is found through a summation over m , yielding [57](S10):

$$M = \sum_{m=1}^{m_{\text{tot}}} \frac{2\pi\omega n_m^2}{c_0^2} \frac{L^2}{(2\pi)^2} \delta\omega. \quad (2.30)$$

The **number of channels** N to which an individual resonance can couple in case of a periodic grating are calculated by considering the area in the $k_{//}$ -plane of the free-space wavevector k_0 , $A_{k_0} = \pi k_0^2$, and dividing it by the area of the unit cell $A_p = (\frac{2\pi}{a})^2$ of the periodic grating, such that $N = \frac{\pi\omega^2}{c^2} (\frac{a}{2\pi})^2$. Each channel is thus a plane wave in free-space with wave vector $k_0 \geq k_{//}$, where $k_{//} \equiv \beta$ is the propagation constant of the mode to which this channel couples [57].

For hyperuniform structures, the propagation constants β are often larger than k_0 , such that no guided resonance can couple to free-space radiation by normal refraction but only through interaction with the HUD structure. It is assumed that all light incident onto the hyperuniform pattern is redirected to acquire any parallel wavevector $k_{//} \in [k_1, k_2]$ through this interaction, where the distribution is further assumed to be homogeneous. A portion of the parallel wavevectors $\delta k \subset [k_1, k_2]$ is suitable to couple to an individual resonance k_m , while the HUD structure allows light trapped by the resonance to couple back to free space. For a simplified case of monochromatic excitation, guided resonances appear as individual rings in-between the bounding circles with radii of the characteristic HUD values k_1, k_2 in the $k_{//}$ -plane, shown in green in fig. 2.3. Each guided resonance ring consists of

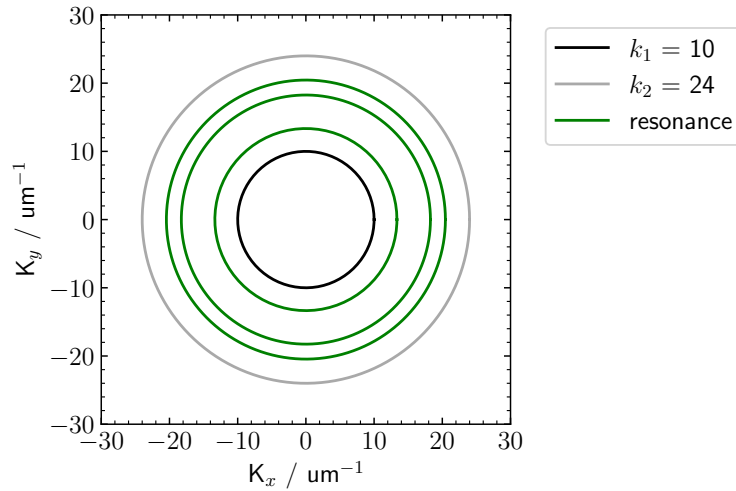


FIGURE 2.3: $K_{//}$ -plane representation of modes at 500 nm wavelength within characteristic HUD boundaries $k_1 = 10 \mu\text{m}^{-1}$ and $k_2 = 24 \mu\text{m}^{-1}$.

multiple resonances, each of which occupy an area $\Delta k^2 = \left(\frac{2\pi}{L}\right)^2$, invoked by the sample area $L \times L$. If all channels supported by the HUD structure in k -space with area $A_{\text{HUD}} = \pi(k_2^2 - k_1^2)$ are assumed as output ports, the number of channels can roughly be estimated as:

$$N = \frac{A_{\text{HUD}}}{A_{\text{resonance}}} = \frac{\pi(k_2^2 - k_1^2)}{(\Delta k)^2}. \quad (2.31)$$

The **intrinsic loss rate** $\gamma_{i,m}$ of a mode describes the rate at which the modes amplitude is decreased due to material absorption and can be approximated via the relation [57]:

$$\gamma_{i,m}(\lambda) = \alpha_m(\lambda) \cdot v_G(\lambda) \approx \alpha_m(\lambda) \frac{c}{n_m}, \quad (2.32)$$

where $\alpha_m(\lambda)$ and v_G denote the mode's absorption coefficient and group velocity, respectively. For a small frequency interval $\delta\omega$, group velocity $v_G = c \left(n + \omega \frac{\partial n}{\partial \omega}\right)^{-1}$ approaches the phase velocity $v_p = c/n$, since $\partial n \rightarrow 0$ as shown in the approximation on the right-hand side in (2.32).

With these definitions, (2.28) can be rewritten and simplified to:

$$\tilde{A} = \sum_m \frac{4\pi\alpha_m k_m}{(k_2^2 - k_1^2)}. \quad (2.33)$$

(2.33) represents an effective absorption at frequency ω , which can be expressed as the product of (bulk-) absorption coefficient α_0 multiplied with thickness W of the absorber and an enhancement factor $F \equiv \tilde{A}/(\alpha_0 W)$ [57]. Fig. 2.4 shows \tilde{A} and $\alpha_0 \cdot W$ plotted against wavelength in semi-logarithmic scale, where the values of k_m and $\alpha_m = 2k_0\kappa$ are populated using mode data computed with an algorithm developed for this thesis and described in the following section 2.3.1. An enhancement of \tilde{A} over the bulk absorption is seen throughout the wavelength range.

In order to estimate the total absorption for a section of the solar spectrum according to (2.33), the analytical solutions for lambertian light-trapping in textured solar cells, derived by M.A. Green, are employed [63]. These consider a patterned slab with perfect metallic reflector on the rear. There are several approximations provided by the author that are more or less accurate depending on the magnitude of the absorption coefficient α times the device thickness W , since the radial distribution of light-intensity from a lambertian scatterer also depends on the product αW . The average path length of a light ray approaches $1W$ in case of strong absorption ($\alpha W > 5$), but increases up to $4W$ in case of very weak absorption ($\alpha W < 0.2$) [63](ch: Asymptotic behavior).

The product αW in these formulas can be identified with \tilde{A} from 2.33, since the absorption \tilde{A} is unitless and the thickness is incorporated through the magnitude of m , which is the number of modes taking part in the summation. Since the path length enhancement factor $f_p \in [1, 4]$ depends on the magnitude of \tilde{A} , the latter needs to be considered in order to choose the most accurate approximation for the total absorption in the slab.

The modified equation (7a) from Green including f_p is reproduced below:

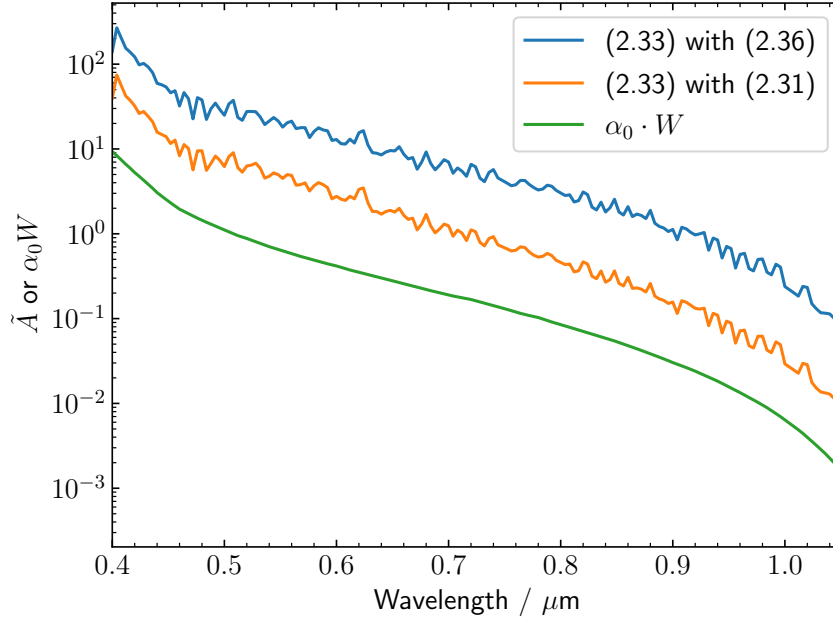


FIGURE 2.4: Comparison of the absorption \tilde{A} from (2.33) and (bulk-) absorption coefficient α_0 multiplied with thickness W for a $1\ \mu\text{m}$ thick silicon slab. The difference between the orange and blue curves arises from an alternative enumeration of N_m in (2.31) and (2.36), respectively.

$$A(\omega) = \frac{1 - \exp(-f_p \cdot \tilde{A})}{1 - (1 - \frac{1}{n_m}) \exp(-f_p \cdot \tilde{A})} \quad (2.34)$$

It may be inferred, since \tilde{A} already includes an enhancement arising from the coupled-mode theory estimation, $f_p = 1$ should be set. At any rate, for an upper limit of total absorption also $f_p = 4$ is considered.

Using (2.34) it is now possible to calculate the integrated, spectrally averaged absorption IA by convolution of (2.34) with the AM1.5 solar spectrum [43], shown in fig. 2.5, integrated over the wavelength range $[400, 1050]\ \text{nm}$:

$$\text{IA} = \frac{1}{\int_{\omega} F(\omega) d\omega} \int_{\omega} A(\omega) F(\omega) d\omega, \quad (2.35)$$

where $F(\omega)$ describes the number of photons per square meter and second at the frequency ω as obtained from the AM1.5 spectrum.

(2.35) has been employed by Tavakoli et al. in order to predetermine a set of characteristic HUD values k_1, k_2 , which in turn were used as starting points for full-wave FDTD simulations to find the optimum k_1, k_2 values experimentally [35]. The article is under review at the time of writing this report, but the optimizations have been concluded and suggest the values $k_1 = 10$ and $k_2 = 20$, approximately. Based on these results, the optimized HUD structures presented in this work were generated and scaled up to show enhanced light trapping on large-area substrates and solar cells with soft imprint techniques, thereby paving the way for high-throughput manufacture of highly-efficient thin-film photovoltaic devices.

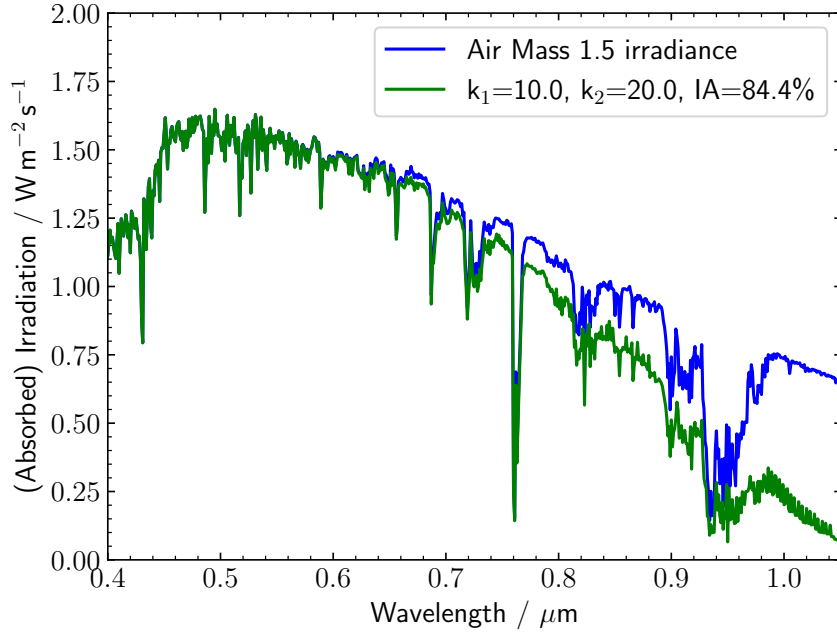


FIGURE 2.5: AM1.5 solar irradiance data and absorbed fraction thereof calculated with (2.34) for $k_1 = 10$ and $k_2 = 20$ versus wavelength. Integrated absorption (IA) given in the legend is computed via (2.35).

Predetermining the HUD values is performed by plotting (2.35) for $k_1, k_2 \in [5, 100] \mu\text{m}^{-1}$ as seen in fig. 2.6 for a path length enhancement of $f_p = 1$ (left) and $f_p = 4$ (right) across the entire spectral bandwidth.

It should be noted that the derivation of (2.33) in [35] differs from the above and the final result shown in the supporting information of the article features an extra effective refractive index n_m in the denominator of (2.33), since the enumerations of N_m and M are based on a different approach in the article. Another alternate enumeration of N_m based on rigorous adherence to [57] was suggested by Prof. F. Koenderink [64] and involves geometric construction of the overlap between the HUD-supported diffraction region and the light-cone in k -space, which is sketched below in fig. 2.7 with permission from Prof. Koenderink. From fig. 2.7, the overlap between the colored regions can be estimated as a fraction of the ring with area $A = \pi(k_2^2 - k_1^2)$, given by twice the subtended angle $2\phi = 2 \arctan(k_0/k_m) \approx n_m^{-1}$, divided by 2π . The number of channels follows from the area fraction $A_{\text{frac}} = A(\pi n_m)^{-1}$ by division through the k -space area per channel $A_{\text{channel}} = (\Delta k)^2 = (L/2\pi)^2$:

$$N'_m = \frac{A_{\text{frac}}}{A_{\text{channel}}} = (k_2^2 - k_1^2) \frac{1}{n_m} \left(\frac{L}{2\pi} \right)^2. \quad (2.36)$$

(2.36) holds approximately for small angles ϕ and $(k_2 - k_1) \leq 2k_0$, where it is further assumed that the ring intersects $k = (0, 0)$ roughly at $k_m = \frac{k_2 - k_1}{2}$. Plugging (2.36) instead of (2.31) into (2.28) yields an alternate version of \tilde{A} in (2.33), which differs to the former by an extra factor of πn_m in the numerator.

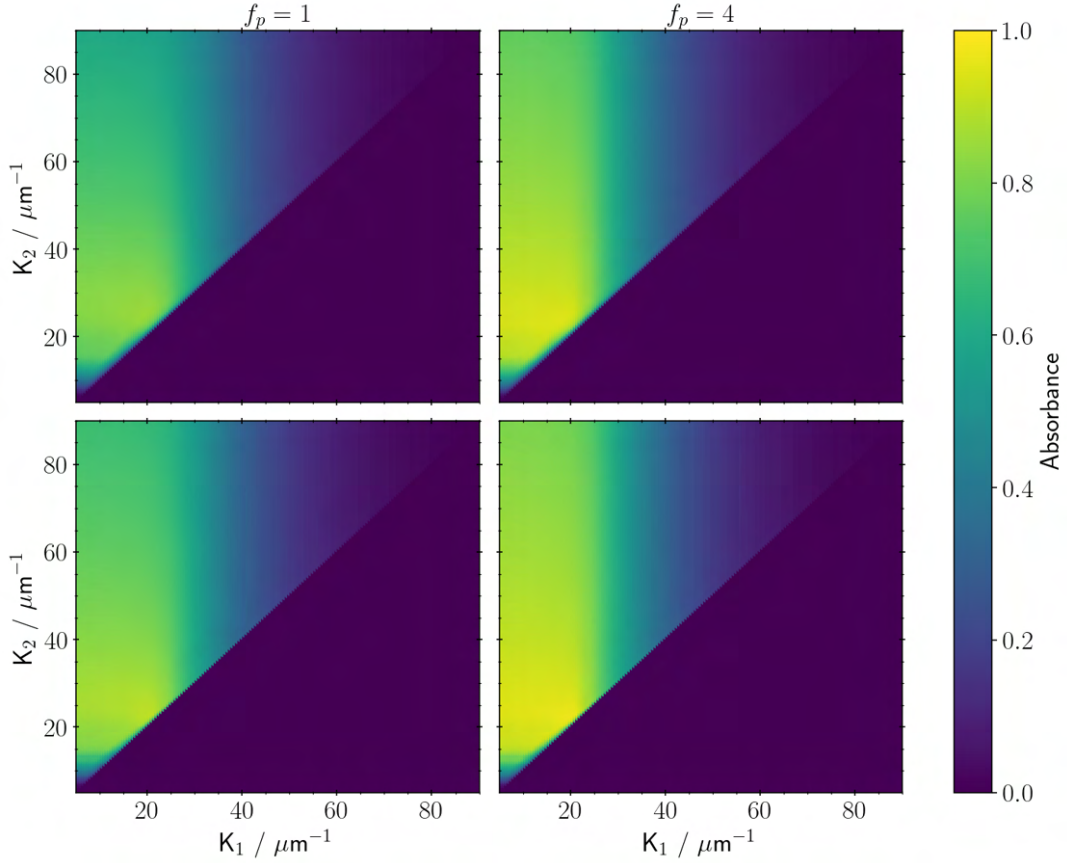


FIGURE 2.6: Absorbance for HUD patterned $1\text{ }\mu\text{m}$ -thick Si slab, calculated with (2.35) and $f_p = 1$ in the left column and $f_p = 4$ in the right, visualized by color versus characteristic HUD values $k_1, k_2 \in [5, 90]\mu\text{m}^{-1}$. On the top row, the mode data was calculated with the python solver (sec. 2.3.1) for a Si slab in air and using the extinction coefficient $K = \kappa$ (cp. with sec. 2.1.3). Absorption is maximized at $k_1 = 20\text{ }\mu\text{m}^{-1}$ and $k_2 = 26\text{ }\mu\text{m}^{-1}$ (left) and $k_1 = 18\text{ }\mu\text{m}^{-1}$ and $k_2 = 23.5\text{ }\mu\text{m}^{-1}$ (right). On the bottom row, the mode data was obtained through the FDE solver for the slab with anti-reflective coating (sec. 2.3.2) and absorption is maximized for $k_1 = 21\text{ }\mu\text{m}^{-1}$ and $k_2 = 23\text{ }\mu\text{m}^{-1}$ (left) and $k_1 = 20.5\text{ }\mu\text{m}^{-1}$ and $k_2 = 22.5\text{ }\mu\text{m}^{-1}$ (right).

2.3 Numerical methods and FDTD simulation

Finite-Difference Time-Domain (FDTD) simulation describes a numerical method of obtaining solutions for Maxwell's equations in any given system using a finite number of elements (mesh-cells) and time-steps to model dynamic electromagnetic processes. The boundary conditions for every pair of adjacent mesh-cells are evaluated at each time-increment until the total simulation time or a predefined condition has been reached. It is thus not possible to retrieve exact solutions with FDTD, but all results will retain a size-adjustable numerical error. In this work, FDTD is utilized to calculate the guided modes of a thin slab of silicon as well as the absorption of light in a (textured) slab with back-reflector and anti-reflective coating. The guided modes of a thin slab of silicon are found using the finite difference Eigenmode (FDE) solver of Ansys-Lumerical simulation software [65], which computes the time-independent

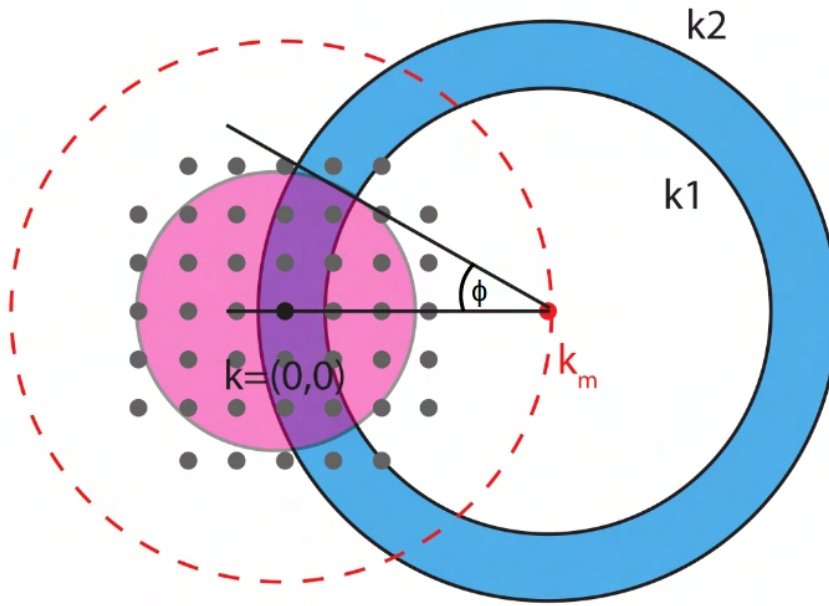


FIGURE 2.7: Geometrical evaluation of the number of channels N_m , to which a resonance m with wavevector k_m can couple through virtue of the HUD-structure with characteristic numbers k_1, k_2 . Channels in free space are found in the colored circle around $k = (0,0)$ with radius k_0 and are shown as dots with a pitch Δk obtained from considering a sample area $L \times L$ with $\Delta k = \frac{2\pi}{L}$. Reprinted with permission from [64].

field-solutions of a one- or two-dimensional system with symmetry along the orthogonal directions.

Absorption on the other hand is found by illuminating the system with a short light-pulse of well-defined spectrum and intensity and computing its spatial dispersion after a certain duration or until the remaining intensity has decayed below a preset threshold. Decay pathways are due to absorption within the materials of the simulation or through the boundaries of the finite simulation volume, which for this purpose are modeled as perfectly-matching layers (PML) without back-reflection. The integrated absorption IA values given in the legends of the following figures are calculated through convolution of the AM1.5 irradiance data shown in fig. 2.5 with the absorption spectrum $A(\omega)$, integrated over the incident spectral range [400,1050] nm according to (2.35), where the absorption spectrum \tilde{A} is replaced by the absorption $A(\omega)$ found through FDTD simulation $\tilde{A} \rightarrow A(\omega)$. The following section 2.3.1 introduces a simple mode solver programmed in python for this work and is compared to the solutions obtained via the FDE-solver included with Lumerical (sec. 2.3.2). The subsequent section 2.3 focuses on the full-wave simulation in 3D, and finally the results of all sections in this chapter are compared and discussed in sec. 2.4.

2.3.1 Python script for calculating waveguided modes of a triple-layered stack

Using the boundary condition (2.18) from sec. 2.1.3 and n and κ of the chosen materials, one may calculate the modes of propagation of plane-waves confined by total internal reflection.

The script can be configured to use any dielectric material in each of the three layers

and is capable of importing tabulated n, κ -values, such as Green's [66] values for silicon from refractiveindex.info [67].

One may then set the desired wavelength range and intermediate steps, as well as the desired precision to which propagation constants shall be approximated. Lastly, the thickness of the central layer is defined, upon which the calculation and subsequent data-export to a file, as well as a set of different graphical representations can be initiated.

The algorithm probes sequential values of θ_1 and computes $\phi_i(\theta_1)$ and $\phi_t(\theta_1)$, which are inserted into (2.18) yielding a value for m . Subsequently, the deviation of m from an integer is calculated and compared with the desired precision. If the latter is not reached, the next iteration probes smaller deltas of θ_1 -values inside the last interval that 'encircled' the true θ_1 , *et cetera*. The script in form of an import-friendly library (module), or an interactive Jupyter notebook is freely available and provided with lots of comments and instructions on github [68][69] and an exemplary execution of the notebook is found in appendix A.

Plotting the propagation constant β obtained from the algorithm above for a crystalline silicon waveguide of 1 μm - and 10 μm thickness in air against wavelength, one obtains the dispersion diagram shown in fig. 2.8. The upper/lower black curves in fig. 2.8 represent the dispersion in silicon/air, respectively.

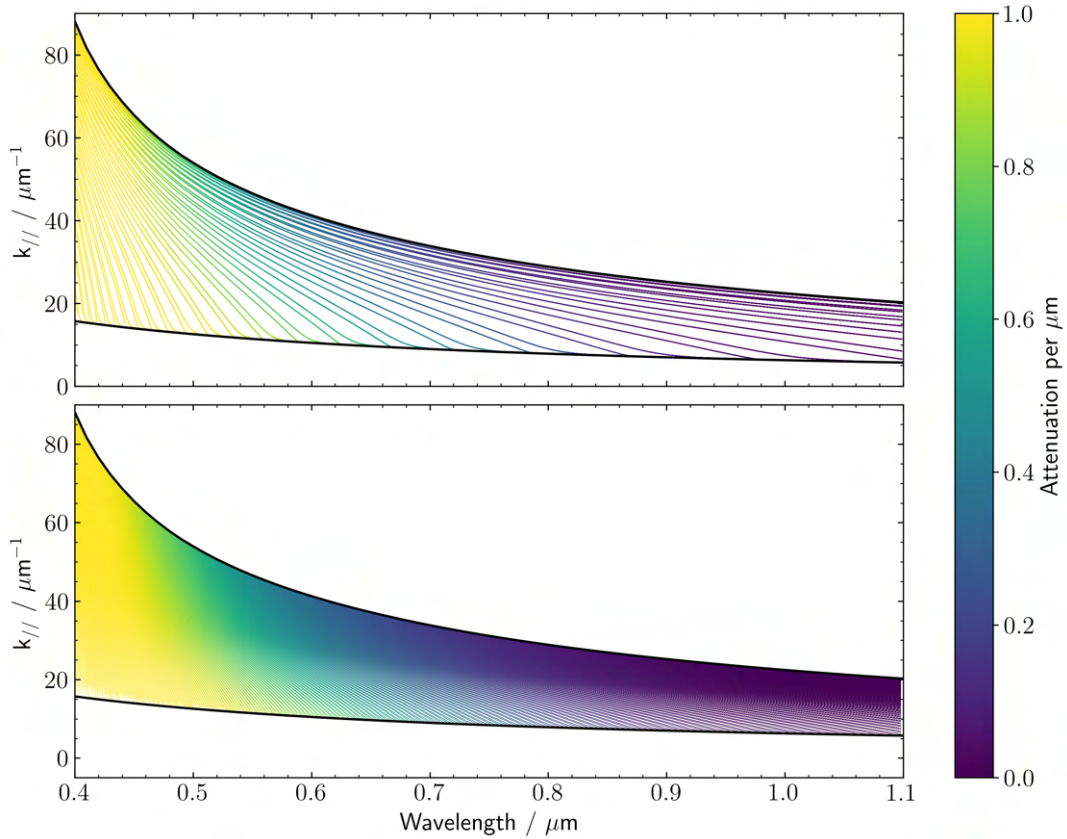


FIGURE 2.8: Propagation constant β against wavelength λ in a 1 μm (top) and 10 μm (bottom) slab of silicon in air in 1D.

2.3.2 Dispersion diagram of a slab of silicon

In order to setup the eigenmode solver, the stack consisting of the silver substrate, the 1 μm silicon waveguide, a 72 nm anti-reflection coating, and the upper air boundary are built in the software. The anti-reflection coating (AR) is set with a refractive index of 1.82 nm across the spectral bandwidth, which was found the optimum value by previous FDTD simulations [35]. Subsequently, the FDE object is created and X:Y-proportional 1D-solver mode selected (cylindrical symmetry), and the layers of the stack are all normal to z . The stack is visualized in fig. 2.9 below, which shows an X-Z view of the setup.

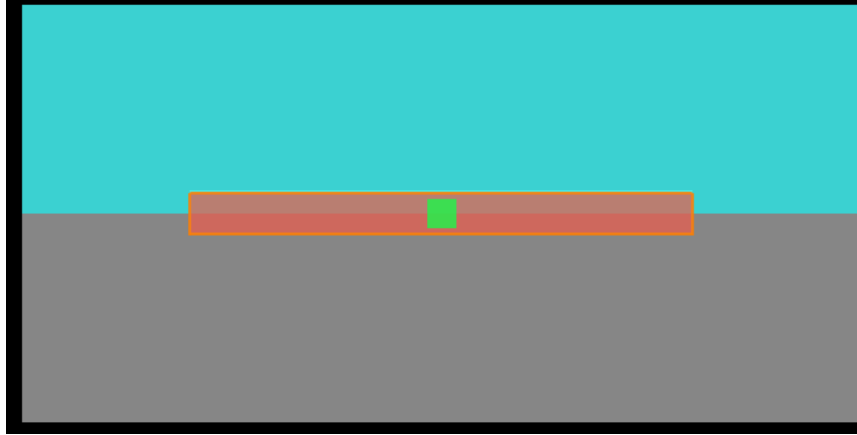


FIGURE 2.9: X-Z view of the waveguide stack in the FDE eigensolver software. The layers are denoted by color, from the bottom up: silver substrate (grey), 1 μm silicon waveguide (red), AR-coating $n=1.82$ (white), upper air boundary (turquoise). The waveguide overrides all other layers, due to its top mesh priority. The square in the center visualizes the position of the FDE solver object.

The conditions at the boundaries of the FDE solver are set to perfectly-matching layers (PML) in the x -/ y -direction, and in z are not changeable in FDE, since this is the normal direction to the cross-sectional simulation mesh. The mode data is calculated in the wavelength range [400,1050] nm, using 200 intermediate steps and 200 test modes are evaluated in the range of the effective index $n_{\text{air}} < n_m < n_{\text{Si}}$. In contrast to the mode solver developed for this thesis in sec. 2.3.1, the FDE also computes radiative modes, which are not confined by total internal reflection. Comparison with the previous results is facilitated by filtering the mode data above guided modes $n_{\text{air}} < n_m < n_{\text{Si}}$ and brought to the form used by the python3-script. Both steps are done via the ".ImportLumerical()" -function of the latter. The calculated dispersion relations for thicknesses 1 μm and 10 μm are displayed in fig. 2.10.

2.3.3 Full-wave 3D simulation of HUD patterned absorber

Full-wave 3D simulations presented in this chapter are conducted with FDTD-solver of Lumerical [65]. The software allows for import of GDSII design files, such that the same designs that are fabricated into soft stamps for experiments on real substrates (sec. 3.4) are used to simulate the absorption in the FDTD software. In order to incorporate the long-range correlations of the hyperuniform patterns, unit cells with large transverse dimensions of 10-15 μm are required, which in turn demand large amounts of memory and processing power at high mesh accuracy. Hence,

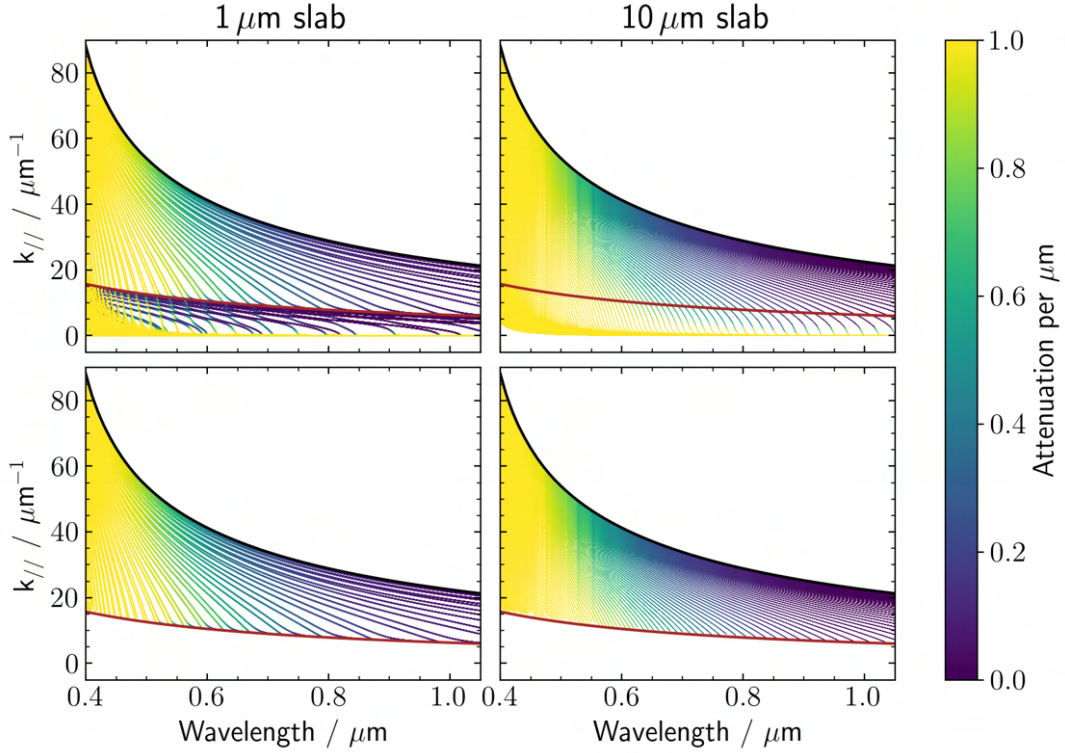


FIGURE 2.10: Dispersion diagram calculated with the FDE solver for a 1 μm (left) and 10 μm (right) Si-slab with Ag back-reflector and 72 nm AR coating ($n=1.82$) on top. The upper row shows all modes calculated by the solver, while only guided modes with $n_{\text{air}} < n_m < n_{\text{Si}}$ are displayed on the lower row.

the Dutch supercomputer "Cartesius" is utilized, which allows up to 480 nodes with 24 CPUs and 64 GB RAM per node to be allocated for parallel computation of the simulations [70].

Each simulation is build up step-wise from a small transverse area of $1 \mu\text{m}^2$ that can be run on most modern computers in a short time and checked for convergence. If no errors occur, both the x - and y -dimensions are increased to (2, 5, and 10) μm consecutively, while for each a design excerpt of according size is imported and another convergence check executed. The simulations are run until the remaining error falls below a predetermined threshold, which is set to 10^{-4} unless otherwise indicated in the respective graphs. The simulation volume is visualized in fig. 2.11 below, where the dimension perpendicular to the stack amounts to $8.3 \mu\text{m}$ and a total of seven monitors are used at different locations recording transmitted power. The boundaries are set to PML above and below the stack, while being chosen as periodic in the transverse direction in the plane of the stack. For improved stability, the lower PML boundary is placed inside the silver layer at a distance of 250 nm from the Si-Ag interface. A monitor close to the latter and another close to the interface allow to determine the energy lost in the Ag-layer as well as the amount transmitted through the PML. Above the source at the top, another monitor records the energy leaving the system through the upper PML boundary and two more are placed very close above and below the pattern, such that energy absorbed in those $\approx 200 \text{ nm}$ can be discerned from the bulk. The anti-reflective coating of 72 nm is hardly visible at this scale and did not receive a notation in the figure. An additional mesh-refinement

region is placed around the patterned region with a margin of 50 nm, in which individual mesh-cells may not be set larger than a threshold of 10 nm by the "conformal-variant 0" automatic-meshing algorithm provided with the software. The material

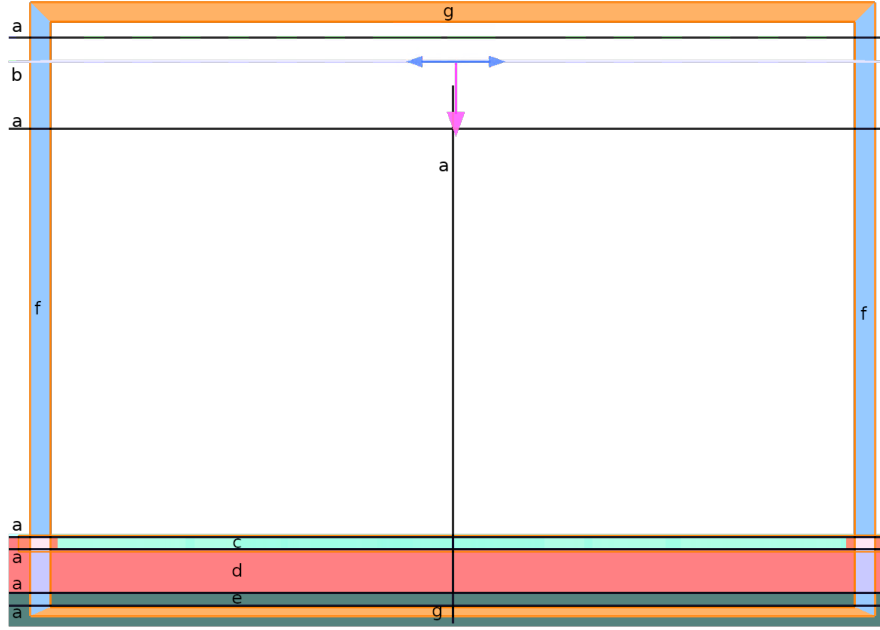


FIGURE 2.11: XZ-view of the simulation volume. There are six horizontal and one vertical monitor recording transmitted power at **a**, the light-source at **b**, the hyperuniform structure at **c**, silicon at **d**, and the silver back reflector at **e**. The boundaries of the simulation are set to periodic at **f** and perfectly-matching layers at **g**. The dimension are $8.3\ \mu\text{m}$ in the vertical (z -) direction and $(1, 2, 5, \text{ or } 10)\ \mu\text{m}$ in both horizontal directions, depending on the respective case.

properties of silicon and silver are approximated as Lorentz-oscillators with a total of 43 and 10 terms, respectively. The residual weighed rms-error in the wavelength range of interest is approx. 1.1 % for Si and 7.1 % for Ag. Plots showing the quality of the fits are found in fig. 2.12. There is a dip of the model in the imaginary part for silicon around wavelength 850 nm, which could not be avoided without causing significant over-estimation of the dielectric function for wavelengths $\lambda > 900\ \text{nm}$.

2.4 Results and Discussion

The waveguided modes calculated with the python3-solver in sec. 2.3.1 show approximately the same amount of modes as the FDE solutions from sec. 2.3.2. In case of $1\ \mu\text{m}$ -Si the verification is simple due to the small amount of modes at that thickness. The imaginary part of the wavevector $\alpha/2$ on the other hand appears larger for the FDE solutions than for the python3-data, especially in the small-wavelength range. This is confirmed by choosing a random test mode from the FDE output and finding a corresponding one in the python3 data by comparing the $k_m(\lambda)$ -profile with all modes and calculating the least difference. Once the mode in closest agreement is found, the imaginary and real parts of the propagation constant are plotted

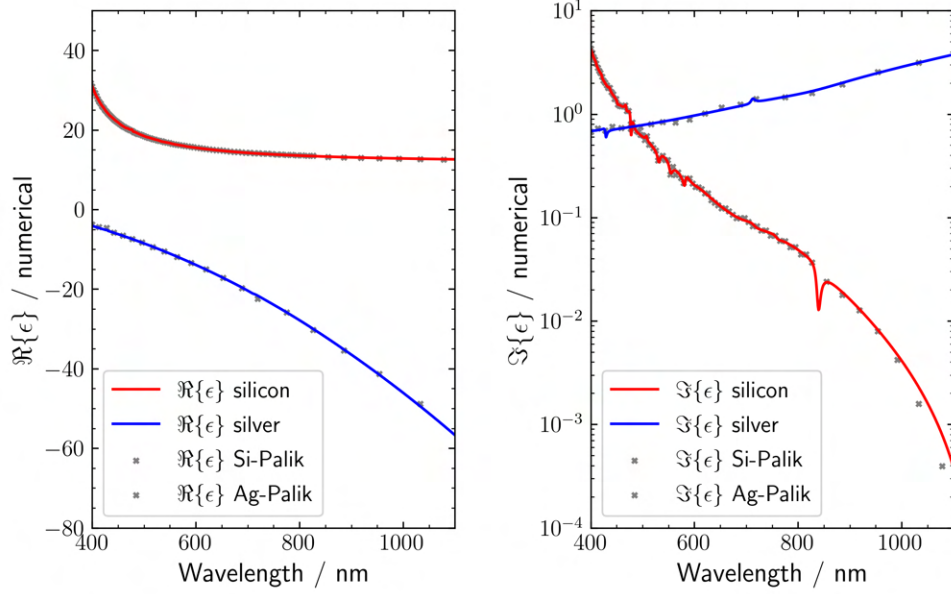


FIGURE 2.12: Dielectric function fits of the materials used in the FDTD simulations. The visible dip of the Si-model’s imaginary part of the index is an unintentional artifact of the fit.

individually for both versions, as shown in fig. 2.13. In the same figure, the question about the definition of extinction coefficient κ raised at the end of sec. 2.1.3 can be qualitatively evaluated. For the test mode shown in fig. 2.13, the attenuation for all versions of κ falls below the values calculated with the FDE solver for all wavelengths $\lambda < 900$ nm. The approximation using $K = \kappa / \sin(\theta)$ deviates less from the FDE solution, especially in the range $700 \text{ nm} < \lambda < 900 \text{ nm}$, where both curves intersect at $\lambda \approx 900$ nm. Incorporating the propagation angle into the extinction coefficient results in a better approximation of the FDE results, but for a large range of wavelengths the imaginary part still differs by about a factor of 1.4. Near the light-line of air ($\lambda \approx 1 \mu\text{m}$), the definition including the confinement factor proves most accurate. The algorithm for comparing individual modes from different sources is included in the python3-notebook [68].

The coupled-mode theory approximation of absorption in the patterned slabs based on either the mode data calculated with the python3-script or the FDE-solver’s output presents several interesting features. From the preceding paragraph about the difference in extinction coefficient in both solvers, a difference in estimated absorption is expected and also the prediction for optimum characteristic HUD values k_1, k_2 is found to depend on the specific mode characteristics. The comparison made in sec. 2.2 for different path length enhancement factors f_p relates to the approximation of absorption in the weakly-absorptive limit. Using $f_p = 4$ results in an upper limit of absorption and the prediction for the optimum k_1, k_2 is only marginally affected by choosing a value of $f_p = 1$ throughout the wavelength range. Fig. 2.6 shows little diminution of absorbance with respect to variations of the characteristic HUD numbers in the vicinity of the optimum k_1, k_2 values. The discrepancy of k_1, k_2 arising from the different sets of mode data employed and compared with the values in [35] based on a different theoretical approach motivates to perform FDTD optimizations for improved HUD designs and further evaluate and develop the coupled-mode theory approach.

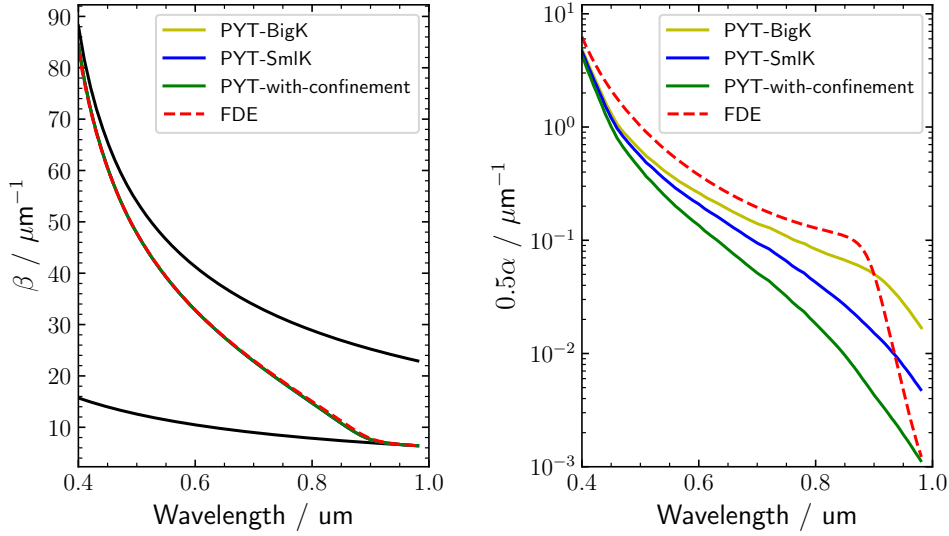


FIGURE 2.13: Comparison of mode solver output from python3-script and proprietary FDE solver from sections 2.3.1 and sec. 2.3.2, respectively. The propagation constant β is compared in the left-hand graph and the extinction coefficient κ times wavevector k_0 , or $k_0\kappa = \frac{\alpha}{2}$ is compared on the right-hand side. The simple mode solver is denoted with "PYT" and the FDE solver is labeled "FDE". The suffix "BigK", "SmlK", or "with-confinement" corresponds to different definitions of the extinction coefficient as explained in sec. 2.1.3, where the first mentioned $K = \kappa / \sin \theta$ is calculated similarly to the effective refractive index N , the second $k = \kappa$ the extinction coefficient at wavelength λ from Green's tabulated values for silicon [66], and the last named using $\alpha_{\text{wg}} = \alpha \cdot \eta$ with confinement η as in [52].

For the k_1, k_2 -values upon which the designs utilized in this work were generated, the absorption spectrum calculated with the different sets of mode data are displayed together with the FDTD result for the hyperuniform disordered arrangement of holes with the same characteristic HUD numbers. The graphs in fig. 2.14 corresponding to the coupled-mode theory approach over-estimate absorption throughout the wavelength range, where solutions found with the FDE solver result in a larger integrated absorption than those from the python mode solver on account of the difference in absorption coefficients. Both solutions found via the coupled-mode approach exceed the lambertian limit, while the FDTD results fall below the lambertian limit for all wavelengths. The lambertian spectrum shown relates to the Yablonovitch $4n^2$ absorption limit [71] of the material and is taken from [35], where in addition an anti-reflective coating was considered. An absorption exceeding the lambertian limit based on theoretical calculations was reported before with light-trapping schemes involving multi-resonant absorption [72][73].

The results from the FDTD simulation with hyperuniform patterns are summarized in graphs below. Since light-trapping is afforded by long-range correlations in the spatial distribution of the patterns, the total absorption depends on the size of the transverse simulation area, where for larger unit cells excerpts of the design higher absorption is expected. The spectra computed with different unit-cell areas for the Spinodal pattern is visualized in fig. 2.15 below. The spectrally-averaged integrated absorption (IA) given in the legend of the figure show a difference of 2% when the transverse area is increased from $1 \mu\text{m}^2$ to $(2 \mu\text{m})^2$. With an increase to

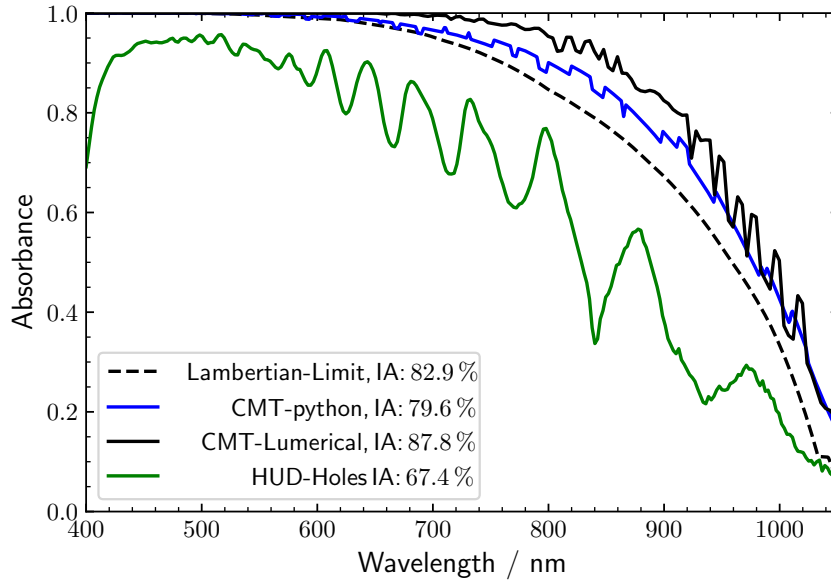


FIGURE 2.14: Comparison of absorption spectrum for 1 μm slab of silicon with Ag-mirror among the coupled-mode theory approach with python-/FDE mode data, FDTD simulation and lambertian limit.

(10 μm)² cross-sectional area the total absorption yields 68.4%, which is about 4 % higher than in the 1 μm^2 case.

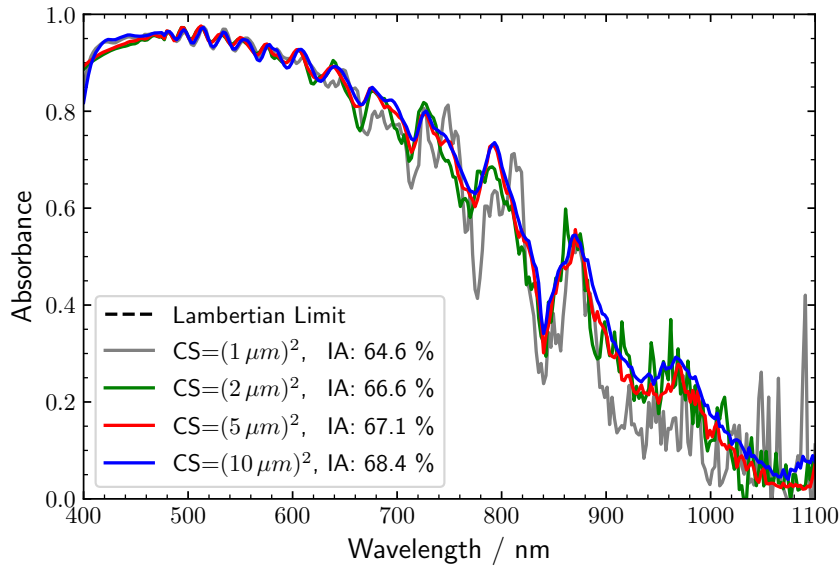


FIGURE 2.15: Comparison of absorption spectrum for 1 μm slab of silicon with Ag-mirror among the different transverse dimensions or cross-sections (CS), which are obtained from FDTD simulation.

It should be borne in mind that the values around 850 nm wavelength are underrepresented, due to the model of the dielectric function ϵ visualized in fig. 2.12, where the same dips below the tabulated data points from literature.

The comparison among the HUDS, Spinodal, periodic and a flat reference slab for the case of 1 μm^2 absorber thickness is found in fig. 2.16. From the values given

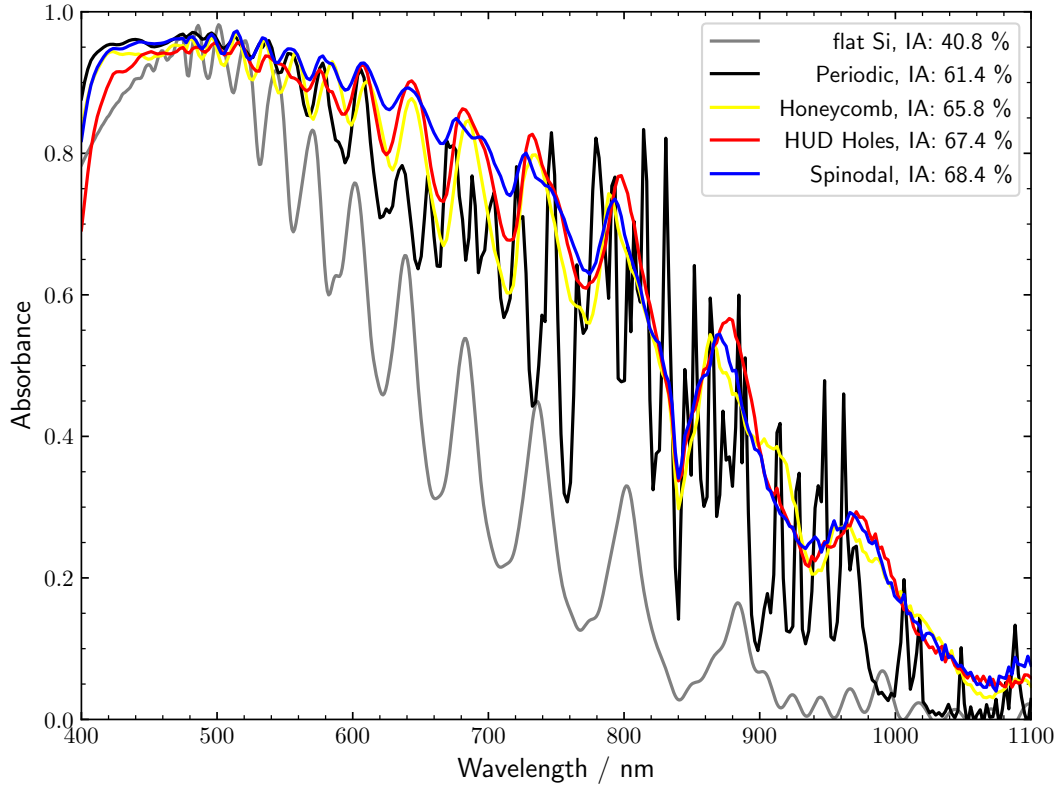


FIGURE 2.16: Comparison of absorption spectra for 1 μm slab of silicon with Ag-mirror and anti-reflective coating among the different hyperuniform and Spinodal design as well as a planar reference slab.

in the figure's legend, one deduces an absolute increase in total absorption in the range (21-27) % for periodic and hyperuniform structures compared to a flat device, where all models feature a 72 nm-thick anti-reflective coating with a constant index of refraction of $n = 1.82$ and zero loss as well as an Ag-back-reflector. The highest absorbance of about 68 % is found for the Spinodal texture. The pronounced Fabry-Pérot-resonances seen in the flat reference are diminished and stretched by the application of the hyperuniform and Spinodal patterns, where the Spinodal shows the least oscillations of all. In case of the periodic grating, the lattice constant and unit-cell parameters of the same give rise to a different kind of sharp resonances resulting in strong differences in absorbance with respect to little changes of the incident wavelength under consideration. These features are typical for periodic gratings rendering implementation of a specific instance less universal, but require careful determination of the employed parameters for the respective application.

Turning to an absorber-thickness of 10 μm , the following figure shows a comparison among a bare slab in air, another with anti-reflection coating ($n=1.82$) and thirdly a slab with both AR and a silver back-reflector. The values given in the legend reveal an IA for the last-named configuration of about 74 %. Without the Ag-layer but with anti-reflection, the absorbance is about equal to the 1 μm -slab with Spinodal pattern and roughly 44 % higher than for a slab without AR. The deviation around $\lambda = 850\text{ nm}$ due to the dielectric-function model again needs to be taken into account. Concerning the same, the flat reference slab with Ag-mirror and AR can be utilized to estimate the error in integrated absorption, when a region around the wavelength where the deviation occurs is taken to be either 1 or 0 in absorbance and

subsequently compared to the original. This is done in fig. 2.18, where the deviation in integrated absorption is given in the legend and found to be in the order of $\pm 2\%$ absolute.

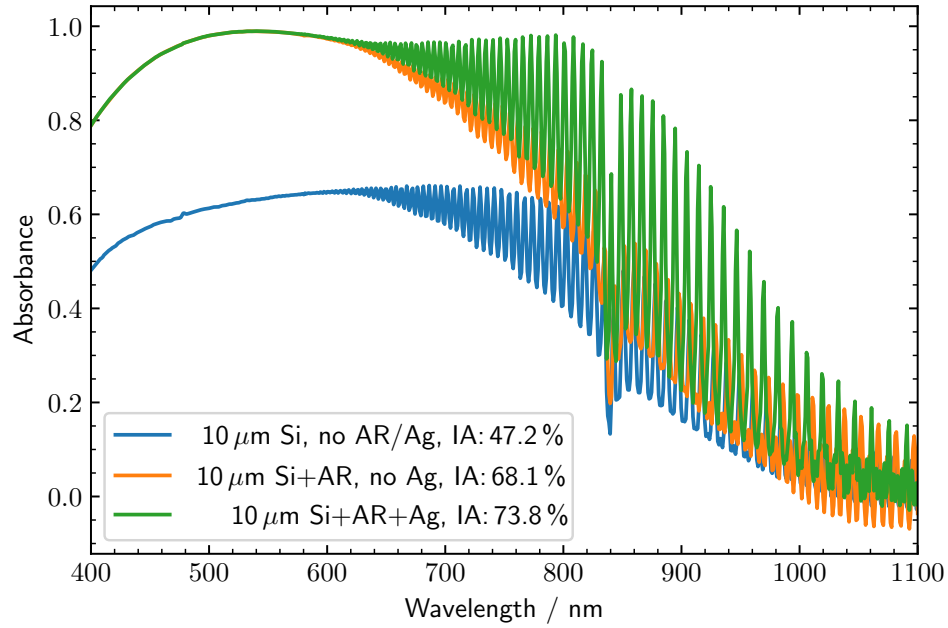


FIGURE 2.17: Comparison of absorption spectra for an unpatterned 10 μm-slab of silicon with and without Ag-mirror, as well as without anti-reflective coating for the latter case.

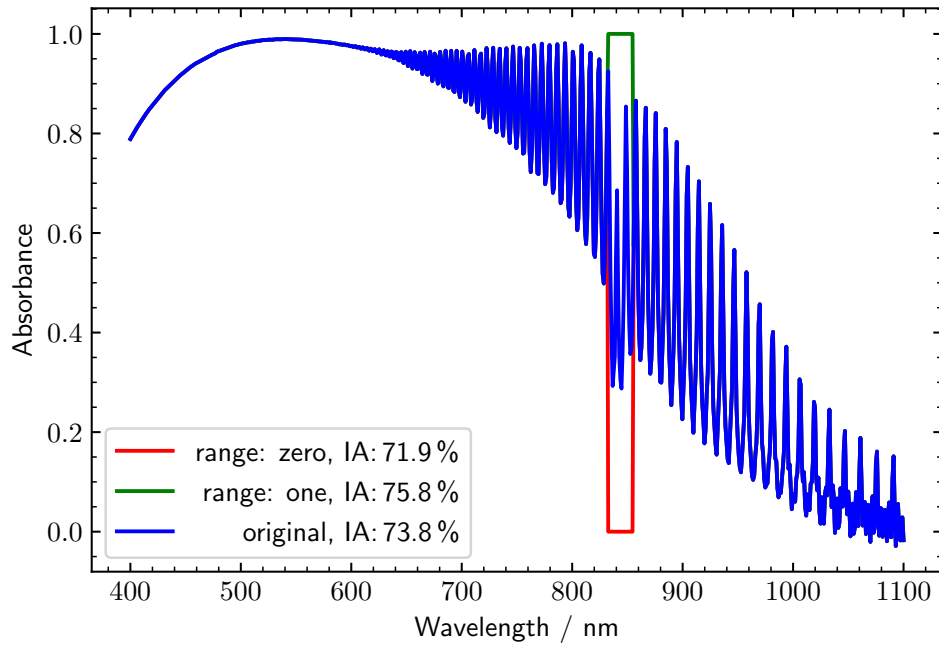


FIGURE 2.18: Comparison of absorption spectra for an unpatterned 10 μm-slab of silicon with and without Ag-mirror, as well as without anti-reflective coating for the latter case.

Finally, the absorbance enhancement by employing the HUD, Spinodal, and periodic patterns into the top 200 nm of 10 μm -thick absorbers are shown in fig. 2.19. As before, the Spinodal outperforms the other patterns, but the difference to the hyperuniform holes and honeycomb structure remains within the limits of uncertainty due to the dielectric function model. The oscillations from Fabry-Pérot resonances in fig. 2.19 are spaced much closer in comparison to the 1 μm -slab on account of the anti-proportionality of the free spectral-range to the thickness of the slab [74].

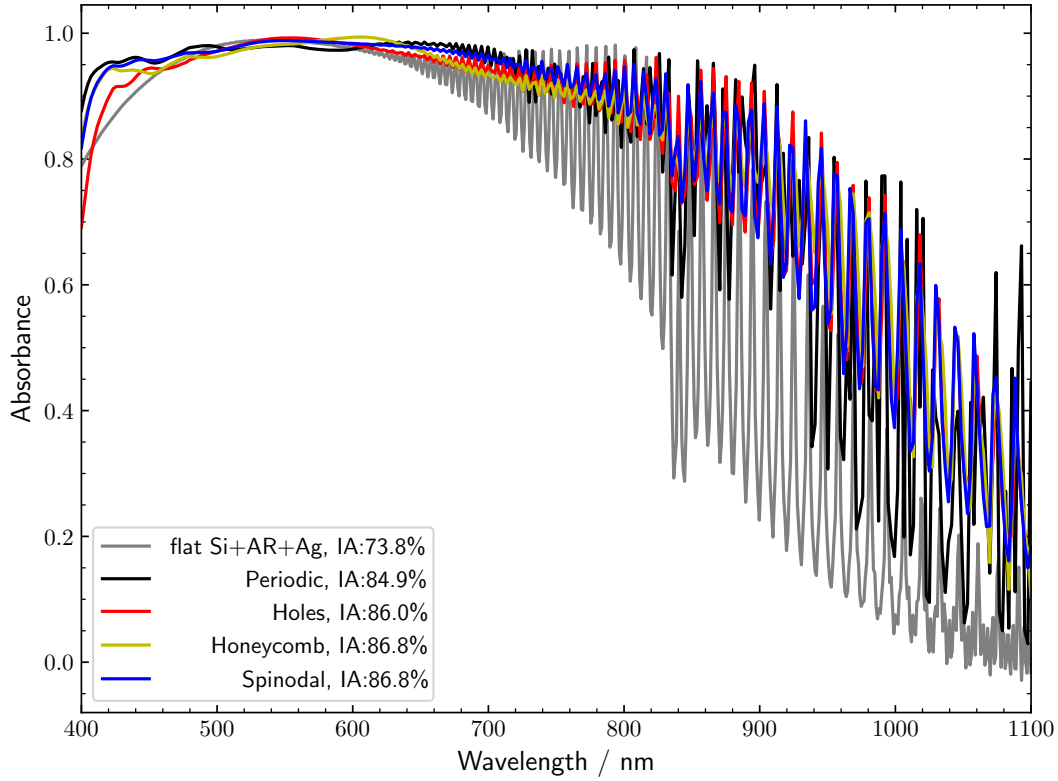


FIGURE 2.19: Comparison of absorption spectra for 10 μm slab of silicon with Ag-mirror among the different hyperuniform and Spinodal design as well as a planar reference slab.

The power monitors included in the simulation volume enable assessment of reflected power due to surface reflection and discern it from the amount reflected by the Ag-mirror at the back of the slab, as well as the fraction of power absorbed solely in the top 200 nm of the slab, where the pattern is located. The latter quantity is simply given by the difference in transmission of the monitors located just above and below the pattern, while for the former a different approach is needed. In order to suppress reflections from the back surface, the PML is placed inside the silicon layer, such that it acts as an infinitely long absorber with no further interfaces. In that case, all reflection measured in the reflection-monitor must come from the air-AR- and AR-Si-interfaces and the pattern just below. Both questions are investigated for the Spinodal pattern, while for the remaining structures only the power absorbed in the pattern is compared in fig. 2.20. From the reflection-spectra on top in fig. 2.20, it is evident that a large portion of the reflected light is due to the Ag back reflector, amounting to a difference of $\approx 5\%$ in spectrally-averaged integrated reflection (IR) between the infinite- and 10 μm -slab with Spinodal pattern. The reduction of

integrated reflection when the Spinodal pattern is applied to a $10\text{ }\mu\text{m}$ -slab is approximately 14 %. In all cases, the reflected portion increases strongly with the incident wavelength above $\lambda \approx 700\text{ nm}$ and needs special attention when designing light trapping structures of this kind. The fraction of power absorbed in the pattern itself is visualized in the lower graph of fig. 2.20, where for the first time the optimized periodic structure yields higher spectrally-averaged, integrated absorption values than the HUD holes and HUD honeycomb. Interestingly, the increased absorption of roughly 3 % of the Spinodal over the unpatterned case, where also only the top $\approx 200\text{ nm}$ are analyzed, is achieved in spite of the about 50 % less silicon present due to the AR-infiltrated pattern of the Spinodal. An explanation for this observation next to in-plane diffraction by the pattern could come from the sub-wavelength confinement of the wavefunction to the Si-parts of the structure.

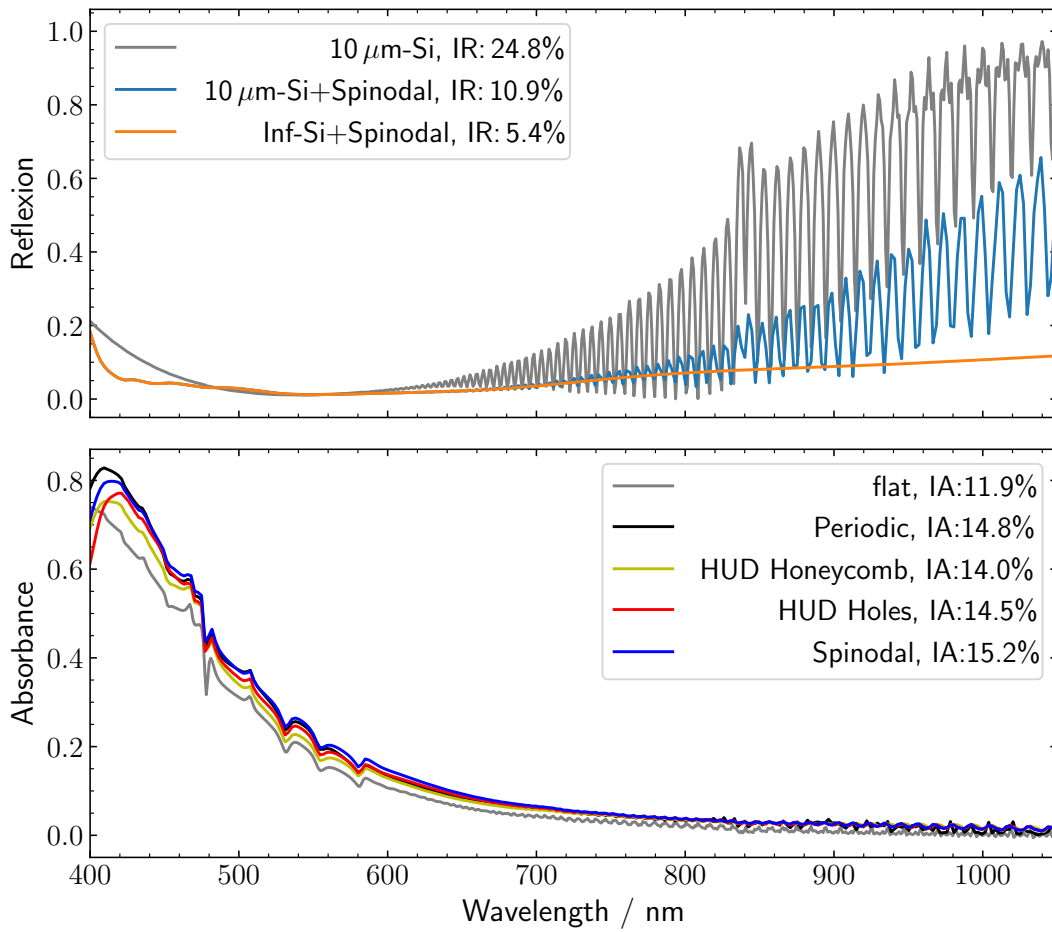


FIGURE 2.20: Analysis of surface reflection (left) and power absorbed in the patterned layer alone (right). The spectrally-averaged integrated absorption for given in the legend in percent corresponds only to the fraction absorbed in the patterned layer.

This concludes the investigation of light-trapping with hyperuniform disordered gratings from a theoretical and numerical perspective and the following chapter describes the fabrication of actual devices towards evaluating their performance on the laboratory scale.

Chapter 3

Manufacturing hyperuniform patterns substrates

In this chapter, methods for fast fabrication of large area hyperuniform disordered structures on top of ultra-thin silicon wafers and thin IBC solar cells are described. Patterning at the nano scale is afforded by substrate conformal imprint lithography (SCIL), a stamping technique capable of creating feature sizes below 10 nm over large areas by combining the advantages of high resolution of hard stamps with the conformality of soft stamps [75][76]. A SCIL stamp is fabricated in layers of different elasticity on top of a master wafer previously patterned with the desired nanostructure. The stamp is utilized to imprint a layer of resist applied to a substrate on which the pattern is to be reproduced, where the resist contains silicon dioxide precursors in this work. After imprinting, the resist converts to a porous SiO₂ layer through evaporation of contained solvents. Subsequently, the stamp can be separated from the substrate and the latter remains with the patterned silicon dioxide mask. With a reactive-ion etch, the pattern is transferred from the mask into the substrate and afterwards the residual layer of SiO₂ can be removed by wet chemical means, such as dipping in low-concentrated HF. Automated SCIL systems capable of handling up to 200 mm wafers are commercially available and the technique is also suitable for implementation in roll-to-roll or similar high-throughput manufacturing processes [76][77].

The chapter is organized as follows: Firstly, the challenge of handling thin, fragile substrates is overcome through development of a suitable bonding procedure (sec. 3.1). Secondly, the steps for fabricating the master wafers (sec. 3.2) and SCIL stamps (sec. 3.3), and producing patterns on thin, fragile substrates (sec. 3.4) are described. Subsequently, the process of transferring the imprinted structure using multi step reactive-ion etching is explained (sec. 3.5), followed by a section on removal of the residual resist layers (sec. 3.6), which concludes the primary fabrication procedure. In the final section 3.7, fabrication results are summarized and discussed. Ultimately, appropriate passivation of the patterned surface and subsequent application of an anti-reflection layer are needed to achieve a full device. These last steps are, however, beyond the scope of this thesis.

3.1 Thin wafer handling systems

In order to enable safe handling of the thin substrates and thinned-down IBC solar cells, several options of temporary bonding to thick carriers were investigated. Bonding options are primarily classified by their use of a bonding agent, such as an

adhesive or contact forming substance. If a third material is to remain in-between the surfaces to be bonded, the method is referred to as indirect. In case the bonding surfaces are in direct contact, the term 'direct bonding' is used. Two commonly used options that are special cases of the latter are anodic direct bonding and electrostatic bonding.

In anodic bonding, a device is bonded to a sodium-rich glass carrier, e.g. Pyrex glass. An electric potential is applied across the bonding interface after the surfaces to be bonded have been brought in close proximity and heated just below the glass' transition temperature. The resulting electric field causes (mainly sodium) ions present in the glass to drift towards the interface and thereby partially screen the applied field. Remaining voids at the interface will cause a larger voltage drop than areas already in contact, and the increased field strength 'pulls together' the surfaces from the edges of voids, resulting in a very homogeneous contact across the entire interface [78]. Anodic bonding is mainly used for permanent bonding applications, such as micro-electromechanical systems (MEMS) or similar devices [79][80]. Choosing an appropriate set of parameters and materials, i.e. applied voltage and temperature, time and annealing conditions, also reversible bonds may be formed this way [81].

In electrostatic bonding, use of a potential difference between either substrate and carrier, or different sections on the latter cause electrostatic attraction between the two surfaces to be bonded. Depending on the materials, AC or DC signals may be used and also carriers with large dielectric constants can be employed that retain a charged and thus bonded state long after the external power supply has been removed [82]. Both anodic and electrostatic bonding were considered for the purpose of bonding thin silicon wafers for this project, but their successful application for temporary bonding requires in-depth studies of the individual case as well as specialized equipment, which was not readily available.

Several options of direct bonding are tested using both thick- and ultra-thin Si-wafers and subsequently assessed by eye, after which debonding is attempted and qualitatively compared. Among these trials, for example O_2 -plasma is used to activate the surfaces prior to bonding, annealing at intermediate temperatures ranging from 70° C to 200° C of the bonded stack was tested, the use of a slowly evaporating contact forming agent, such as IPA or H_2O , or a mixture of the two are also investigated. Furthermore, the "Peel-and-Stick" [83] mechanism, which relies on the susceptibility of the critical adhesion energy of a metal-SiO₂ interface to humidity, was attempted in reverse by bonding Si to Ni-coated Si wafer with water and subsequent dehydration in a nitrogen desiccator. Some photographs corresponding to these experiments are found in the bonding related appendix B. These experiments are in general not reproducible in terms of safe handling thin substrates during the steps and achieving bonded states that appear identical to the eye. The environmental conditions controlling for example the evaporation of contact forming agents would require a dedicated desiccator, whose humidity and temperature can be arbitrarily set. Pre-treatment of the UTSi, on the other hand, with e.g. oxygen plasma, requires a bond by itself, since the thin substrates cannot simply be placed inside a vacuum chamber due to their low weight. Full-area, reversible direct bonding of Si to glass and glass to glass has been shown and investigated for thick, 500 μm substrates with the use of oxygen plasma activation and subsequent annealing [84], such that this route could be pursued further, if suitable equipment becomes available. Debonding is performed by inserting a blade into the interface, after immersing the bonded stack in a solvent that reduces the bonding strength, such as DI-water or ethanol, for many hours up to several days. This mechanical stress, at any rate, may cause

the ultra-thin substrates to break more easily, since the fracture strength strongly depends on the thickness of the silicon [85]. Another uncertainty exists about direct bonding concerning long-term storage, since the bonding force will not necessarily stay the same over extended periods of time, but can both degrade or increase in strength, depending on the initial bond quality and external factors that determine which of the various bonding mechanisms, e.g. van-der-Waals, covalent bonding, mechanical interlocking, become dominant in the individual case [86].

Indirect bonding featuring an adhesive layer are a viable alternative leading to reproducible conditions, but require means of applying first the adhesive at a predefined thickness with little tolerance. Spin coating as a means for applying the adhesive layer is superior to tapes and waxes applied by hand, due to increased uniformity and higher thermal stability [87]. Experiments in which a layer of PMMA (Poly (methyl methacrylate)) was spin-coated onto a quartz carrier and subsequently a thin substrate was placed onto the PMMA, followed by a baking step, were already performed at AMOLF by the photonic materials group [88]. Placing the UTSi onto the PMMA, such that the entire surface achieves sufficient proximity, however, has proven very difficult and small air bubbles trapped at the interface expand during the baking step and cause local deformations of the thin substrate (See fig. B.9 in appendix B).

For this work, an optimized indirect bonding procedure was developed to tackle these issues and allow for both homogeneous application of pressure and add a path for air to escape from the interface during bonding and baking. This approach features a specially developed mount for the spin coater, which allows for the UTSi to be coated with PMMA (or an alternative adhesive) instead of the carrier. By this method, the mount can serve as a flat, rigid backing for making contact with the carrier, while trapped air can escape at the circumference of the thin substrate during the application of pressure and heat.

The membrane mount is thus the only tool in contact with the membrane prior to achieving the bond, which decreases the chance of damage compared with the multi-step pre-treatments described in the direct bonding section. The mount serves to fixate the substrate during spin coating via a vacuum chuck built into the spin coater. For this purpose, a porous filter material is placed at the mount's center, which serves to both reduce and distribute the applied pressure difference evenly across a large portion of the substrate's surface. Different filter materials were tested and compared, with surface roughness and hardness of the material being the two most critical properties determining the resulting flatness of the substrate when the vacuum pump is turned on. A photograph of two well-performing mounts are shown in fig. 3.1, where the left-hand prototype is made from PEEK (Polyether ether ketone), 50 mm in diameter featuring a protrusion of approx. 1 mm height and 24 mm diameter placed in the center of the mount. In the center of the protrusion, a hole of 10 mm diameter is fitted with a nylon filter material spanning the entire thickness of the mount. On the right-hand side of fig. 3.1, a mount made from aluminum with similar dimensions is shown, which features a filter piece made from brass in the center protrusion with a diameter of approx. 20 mm. The use of both alumina and brass affords the mount a higher temperature stability compared to the nylon variant, where in the latter an epoxy-based adhesive was used with a temperature stability up to 70 °C [89]. In addition, the brass filter retains the low surface roughness achieved through extensive polishing much longer due to its superior hardness in contrast to the nylon filter. Optionally, for both mounts an extra spacing material can be used as an inter-layer between mount and substrate, which mitigates remaining irregularities and furthermore prevents direct bonding of the membrane to the PEEK- or or

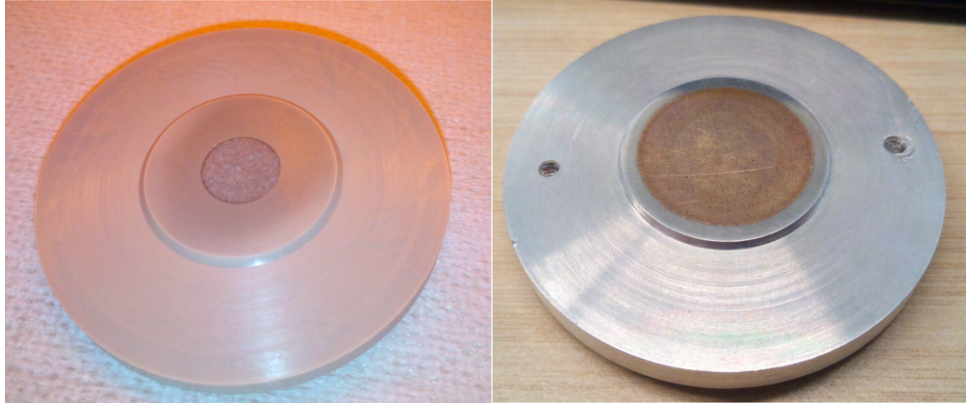


FIGURE 3.1: Membrane mounts for spin coating adhesives on ultra-thin substrates and solar cells. Left: Mount made from PEEK with 10 mm diameter nylon filter piece in the center, through which an applied under pressure serves to flatten the substrate against the mount. Right: Mount made from aluminum with a larger brass filter piece in the center protrusion.

aluminum rim of the mount. Especially with the PEEK mount, direct bonding can become an issue as the highly polished surface and present oxygen species therein, together with the applied pressure comprise a bonding-promoting environment for the membrane. In fact, direct bonding of PEEK and glass with prior plasma activation has emerged as an encapsulation replacement for titanium in medical implants and similar applications [90]. Experiments with a sheet of lens-polishing paper as a spacing layer (see fig. B.1 in appendix B) show at least equivalent surface flatness after turning on the vacuum pump, and the release of the membrane after spin coating is facilitated substantially. The detailed step-by-step procedure for bonding UTSi wafers and thinned IBC cells is found in appendix B and an excerpt highlighting critical steps concerning the preparation of samples for texturing is given in sec. 3.4, after necessary steps for obtaining substrate conformal imprint lithography (SCIL) stamps are described in the following sections sec. 3.2-3.3.

3.2 Master fabrication with electron-beam lithography

Electron beam lithography (EBL) is a structuring technique using a focused source of electrons to selectively expose a polymeric resist with nanometer-scale resolution. During exposure, the beam traverses the substrate in a point-by-point fashion (rastering) and deposits a predetermined amount of charge on every pixel of pattern, while being blanked on positions where the resist is not to be exposed. Although the wavelength of the electrons is small ($\lambda = 8 \text{ pm}$ for 25 kV electrons), the minimum spot-size is limited by the e-source dimensions, Coulomb-repulsion, electron focusing optics and scattering of electrons by the surface. Especially the last named factor is strongly dependent on the electron current, where a current of $2 \mu\text{A}$ already leads to spreading of 100 nm due to interaction aberration [91]. The higher a resolution is required, the lower the current must be and consequentially the longer every pixel needs to be exposed in order to reach a charge necessary for cross-linking (or breakage of cross-links) of the polymeric resist. EBL is thus a technique that is capable of producing 5-7 nm features, but in addition to its necessity for high vacuum and conductivity of the substrate, it requires substantial amounts of time to fabricate

large-area structures, due to the point-based exposure scheme and parameter limitations [92].

Dosage tests for exposure parameter calibration

For every combination of structure, patterning dimensions, and substrate, the parameters for obtaining a 1:1 copy of the design in the resist layer need to be determined by a series of dosage tests, where the charge per pixel is varied around the value provided in the datasheet of the polymeric resist. In this work, the positive-tone resist AR-P CSAR6200.09 is used, which has a nominal dose of $65 \text{ } (\mu\text{C} / \text{cm}^2)$ [93]. The dose tests are comprised of nine fields each with $100 \times 100 \text{ } \mu\text{m}^2$ or $150 \times 150 \text{ } \mu\text{m}^2$ dimensions on 200 nm resist on top of 500 μm thick silicon. In-between the silicon and resist layer, an ultra-thin adhesion layer of HDMS (hexamethyldisilazane or Bis(trimethylsilyl)amine) is spin coated, which promotes bonding of the hydrophobic polymer resist to the hydrophilic native silicon-dioxide layer on the Si wafer [94]. On top of the electron-beam resist, an additional layer for improved conductivity [95] of approx. 60 nm is spin-coated in order to reduce charging of the resist during exposure. The nine fields are each produced with different charge dosages on the same substrate, developed according to table 3.1 and etched as explained later in sec. 3.5 using reactive ions. After etching, the patterned wafer is cleaned from resist residuals first in a low-pressure oxygen-plasma system (Pico [96]) for 20 min and subsequently with a base-piranha solution ($\approx 10 \text{ } \%$ wt.) at $78 \text{ } ^\circ\text{C}$ for 10 min.

TABLE 3.1: Development of the positive-tone electron-beam resist AR-P CSAR6200.09. As an alternative for step 2, n-Amyl-Acetat may also be used with the same parameters. Except for O-Xylene, which diffuses slowly through PP, other solvents can be stored for re-use in appropriate containers.

Step #	time / s	Chemical	Comment	Disposal
1	10	H ₂ O	Rinse conducting layer	Org. low-halogen
2	60	Penta-Acetat	Remove resist	Org. low-halogen
3	6	O-Xylene	Remove residuals	Org. low-halogen
4	15	MIBK: IPA	Ratio 9:1	Org. low-halogen
5	15	IPA	Cleaning	Org. low-halogen
6	10	N ₂ -gas	Drying	-

Electron microscope images of a dosage test series on the honeycomb structure after etching and cleaning are displayed in fig. 3.2.

Surface analysis with electron microscopy

Evaluation of the obtained structures is conducted using a scanning electron microscope (SEM) [97][98]. The SEM creates surface maps by first exciting the material with electrons, in this case of 5 keV and at 86 pA. Upon excitation the material ejects electrons itself and these "secondary electrons" with energies of a few eV are recorded by the system at every pixel it scans, where more recorded electrons result in higher brightness of the spot (pixel) [99]. Areas where the the surface is further away from the electron tip, e.g. the valleys of a structure, appear darker due to the smaller solid angle and increased path-length to the detector, which makes

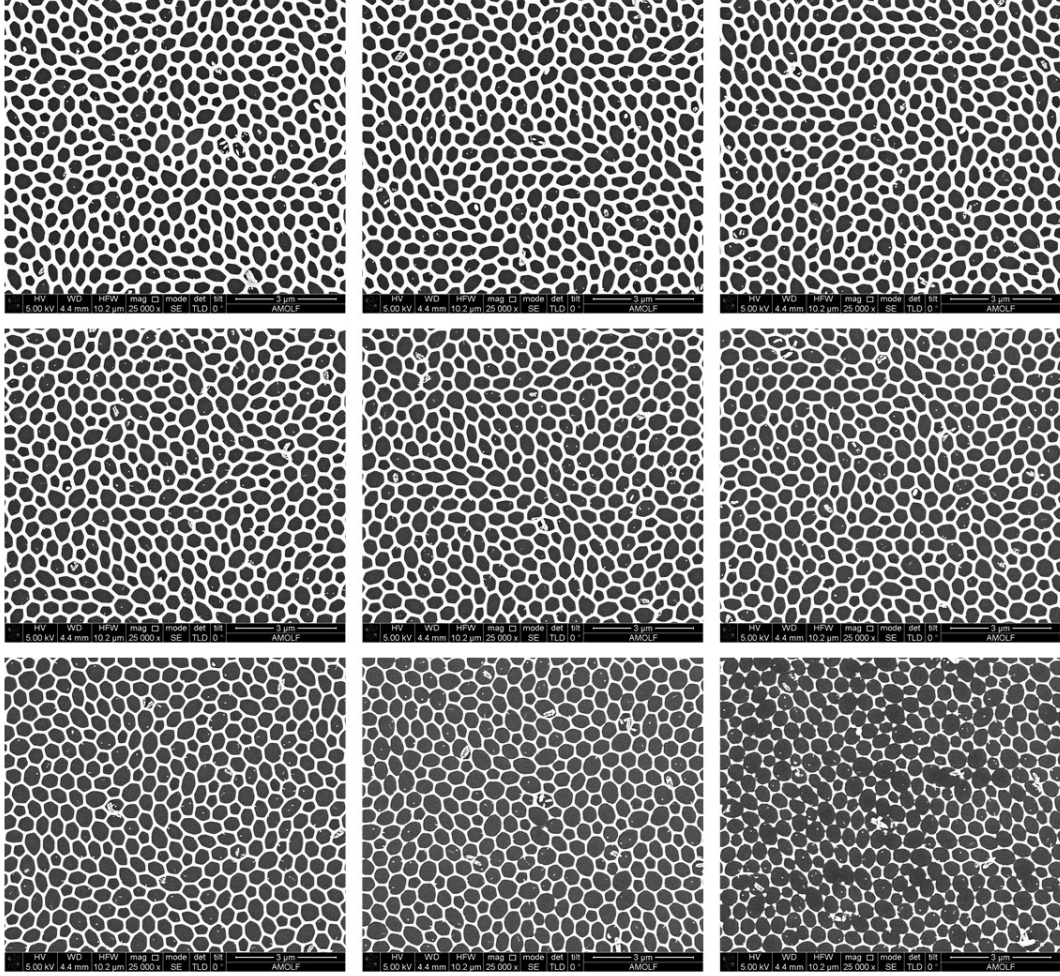


FIGURE 3.2: Scanning electron microscope images HUD Honeycomb for different charge dosages ranging from $100 \mu\text{C}/\text{cm}^2$ in the top-left corner to $180 \mu\text{C}/\text{cm}^2$ in the bottom right, in $10 \mu\text{C}/\text{cm}^2$ -increments. The exposed areas appear dark and correspond to the valleys of the structure, while the remaining silicon walls appear bright and become narrower with higher doses, until eventually the walls become discontinuous in the case of the highest doses. Each of the nine images shows a roughly $10 \times 10 \mu\text{m}^2$ area, the accelerator voltage of the electron column was set to 5 kV at 86 pA. The contrast and brightness are adjusted to facilitate distinction between top level and valleys.

scattering or (re-)absorption by the walls more likely to occur. As a consequence, it is possible to distinguish the top surface of the substrate from the bottom of the valleys by setting a brightness threshold. At the edge-features of the structure, i.e. where vertical walls are located, defects like dangling bonds are more likely to occur, which increases the local density of states and hence more secondary electrons can be generated. These regions may appear brighter than the top surface and render the discrimination between the two levels more difficult when setting the threshold. A strategy for obtaining reproducible results in spite of this complication is provided in appendix C.

Once the threshold is set, the filling fraction of silicon, which serves as the first figure of merit, can be calibrated using an image processing tool of choice, where in

this case the free software "ImageJ" was used [100]. Secondly, a map of spatial frequencies of the SEM image is generated through a fast-Fourier-transform algorithm provided with the image processing tool, which produces a set of magnitude- and phase maps of the original image. Subsequently, a radially-averaged profile is extracted from the magnitude map using a plugin for ImageJ [101]. A spatial calibration obtained from the dimensions of the original image allows for the absolute frequency of each pixel in the radial profile to be determined, while the recorded intensities are normalized to the region of interest $5 \mu\text{m}^{-1} < k < 30 \mu\text{m}^{-1}$, where k denotes the spatial frequency. Both area fraction and radial profile are extracted from all dosage test fields and compared with the properties of the design file, which for this purpose is processed in exactly the same way as the SEM images.

The second figure of merit is given by the standard deviation of the measured radial profiles from the one obtained from the design file. This is achieved by interpolating the profile from the design and computing the squared difference of intensities at each point of the radial profile obtained from the SEM image. The figure of merit is then given as:

$$\text{FOM} = \sqrt{\frac{\sum_k^N (I_s(k) - I_d(k))^2}{N}}, \quad (3.1)$$

where k denotes the spatial frequency, N corresponds to the number of points in the interval of interest $k \in [5, 30] \mu\text{m}^{-1}$, and $I_s(k) / I_d(k)$ denote the normalized intensity at frequency k of the sem image / design image, respectively. Exemplary plots for determining the correct dose for exposure of the honeycomb pattern is given in fig. (3.3) and (3.4), where in this case the silicon filling fraction of the top layer corresponds to the thickness of the walls comprising the honeycomb network. From the figures the dose factor value with the best compromise for filling fraction and deviation in the radial profile is chosen for exposing the SCIL master wafer. The error in filling fraction is estimated from taking two slightly different thresholds of the same image and computing the difference in resulting filling fraction, as explained in appendix C. The radial-profile error is estimated similarly and amounts to approximately $\pm 1\%$ for the second figure of merit, which is also shown in appendix C.

Speeding up the exposure of a $20 \times 20 \text{ mm}^2$ area.

In general, exposing a pattern with EBL and positioning it on the substrate is done via a position list in the controlling software. Each pattern or instance thereof corresponds to a line in the position list and the list items are written sequentially. For each entry the sample stage is first driven to the starting position of the field, then the design data is decomposed and translated into instructions for the stage drive and beam blanker, and lastly these instructions are executed, which results in the structure actually being written.

In order to expose a large area with a small design, the same is multiplied and positioned in a raster, where for each instance the decomposition of the design is repeated, which creates a large computational overhead and significantly slows down the patterning procedure.

Alternatively, one would capture the decomposed design in form of a large binary file, which holds the instructions for writing one instance of the pattern. With the help of a script, these instructions can directly be fed to the pattern generator over and over again without any dead times due to computation. All that is necessary

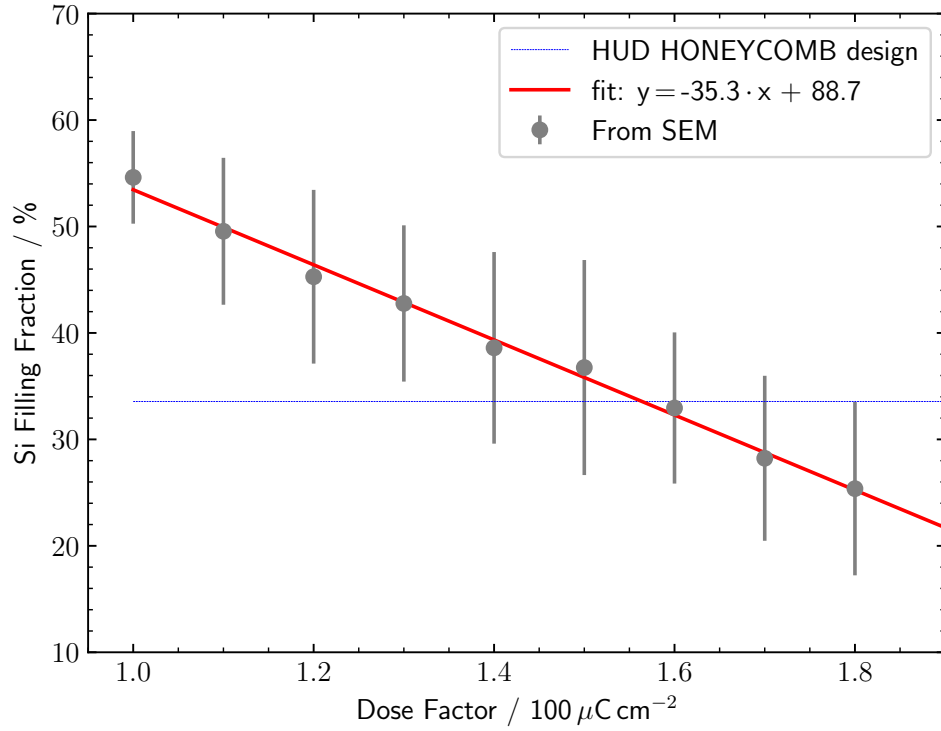


FIGURE 3.3: Silicon filling fraction of HUD Honeycomb for different charge dosages ranging from $(100 - 180) \mu\text{C}/\text{cm}^2$. Column mode: MC60.

is to insert instructions for moving the stage according to the raster in-between the individual exposures. This technique is called dump-file exposure (DFE).

The dump file is generated according to the parameters of the exposure, namely the beam current, desired dosage, step size, and area-filling mode. From these parameters, the dwell time per pixel is calculated and the design is broken down into pixels with a pitch equal to the step size, but only at locations where the beam is not blanked and the resist to be exposed. The area filling mode controls the beam's trajectory in areas where pixels are located, the most common choices being concentric or longitudinal, corresponding to an inward/outward spiral motion in case of the former or a 'line-by-line' progression for the latter.

The dwell time per pixel is found via the equation below:

$$\text{Dosage} = \frac{\text{current} \cdot \text{dwelltime}}{\text{stepsize}^2}. \quad (3.2)$$

In order to expose a structure in the shortest possible time, the dwell time should be minimized, while current and step size should be chosen as large as possible. In practice, the dwell time cannot be smaller than 60 ns due to the maximum blanking speed of the beam, the current can only be set by the column mode, which has relatively coarse increments (LC40 0.22 nA; LC60 0.5 nA; MC40 1 nA; MC60 2.5 nA; HMC40 5.5 nA;...), and the step size should be small enough to accurately reproduce the design. Furthermore, the beam speed is limited by the manufacturer's recommendation to about 100 mm/s. At any rate, dump-file exposures exceeding the beam speed recommendation have been performed successfully up to about 270 mm/s and were also employed in exposing the SCIL master wafers.

The dimensions of the unit cell for DFE is critical for the total exposure duration,

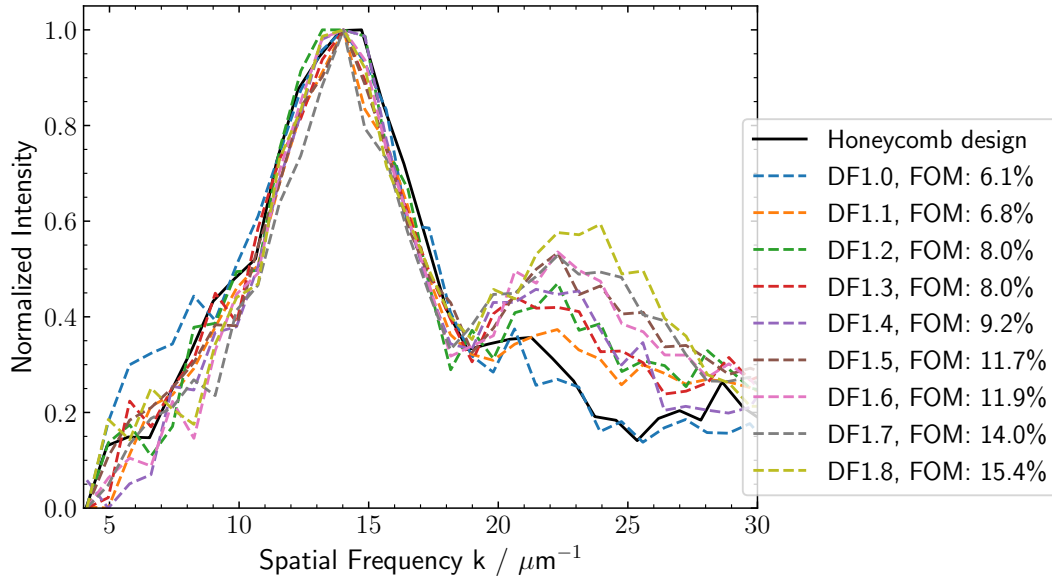


FIGURE 3.4: Radial profile of fourier-transformed SEM images and design file. FOM provided in the legend in percent as calculated with eq. (3.1) for different charge dosages $DF \cdot 100 \mu\text{C cm}^{-2}$. Column mode: MC60.

since they determine the number of matrix elements to be written as well as the file size of the dump file, which needs to be transferred and read repeatedly. The maximum dimensions are limited by the maximum write-field size of the system, which in this case is $500 \mu\text{m}$. After each stage move, a short pause called the "stitch wait" is inserted, which by default takes 500 ms and allows for the stage to settle before the exposure resumes to improve the quality of the stitching boundaries. Experiments in which the unit cell dimensions, stitch wait, or step size were varied, are summarized with their duration per mm^2 of patterning in table 3.2.

For each test exposure the number of unit cells and thus number of stitches was at least nine and the column mode MC60 was chosen, which corresponds to about 2.5 nA beam current.

TABLE 3.2: Patterning time per mm^2 -area (T mm^{-2}) vs. step size, unit cell dimensions (Dim.), and DFE file size for different structures. The column mode MC60 corresponds to a beam current of approx. 2.5 nA.

Structure	Step size / nm	Dim. / μm^2	file size / MB	T mm^{-2} / min
Spinodal	12.5	100×100	214	20
Spinodal	12.5	100×100	214	21.4
Spinodal	12.5	100×100	214	7.8
Spinodal	12.5	100×100	214	7.47
Spinodal	12.5	200×200	850	5.58
Honeycomb	12.5	150×150	1400	15.9
Honeycomb	12.5	150×300	2200	16.6
Honeycomb	12.5	300×300	3000	47
Honeycomb	15	150×150	1400	11.95
Honeycomb	15	300×300	2000	10.1

Since the total area is 400 mm^2 , a time of 5 min per mm^2 corresponds to roughly

33 h of exposure, while a value of 16 min already takes 106 h and thus more than four full days for which the system needs to be reserved. Another factor involved in the long term exposure is the stability of the beam current, which according to the manufacturer deviates by less than 5 % per hour. This tolerance linearly influences the actual dosage delivered via eq. (3.2), which in turn can vary quite a bit, when the exposure lasts several days. The honeycomb, HUD holes and periodic patterns could not be optimized to achieve the roughly 5 min per mm^2 of the Spinodal exposure, and the next higher column mode HMC40 ($\approx 5.5 \text{ nA}$) is chosen for exposing them. Another series of patterning time trials via dump-file exposure are displayed in table 3.3 for the HMC40 column mode.

TABLE 3.3: Patterning time per mm^2 -area ($T \text{ mm}^{-2}$) vs. step size, unit cell dimensions (Dim.), and DFE file size for the honeycomb-structure. The column mode HMC40 corresponds to a beam current of approx. 5.5 nA.

Structure	step size / nm	Dim. / μm^2	File size / MB	$T \text{ mm}^{-2} / \text{min}$
Honeycomb	15	300×300	2050	3.9
Honeycomb	20	300×300	1230	7.57
Honeycomb	15	450×450	4700	4.05
Honeycomb	18	450×450	3310	10.93

The duration per mm^2 ($T \text{ mm}^{-2}$) of patterning shown in table 3.3 show peculiar dependencies on both step size and unit cell dimension, where for example between line 1 and 2, one would expect the time to decrease due to fewer steps required at larger step sizes, yet the opposite behavior is observed. This makes optimizations hard to predict and a series of parameters necessarily needs to be tested for every individual structure in order to obtain the desired patterned area in the shortest possible time. After exposure, the master wafer is processed as described for the dosage tests above, i.e. developed and etched to a depth of 120 nm, followed by removal of the residual resist layers through ashing and immersion in a base piranha solution. At this stage, the soft stamp may be fabricated from the master mold.

3.3 Stamp fabrication

After the silicon master featuring the final pattern has been obtained and cleaned, from it a SCIL stamp is made through a molding procedure developed initially by Mark Verschuuren [75] and subsequently optimized for the AMOLF NanoLab [102]. The fabrication of the stamp was performed by Dimitry Lamers, who is also responsible for optimized instructions and the author takes no credit for this part of the process. The following points summarize the fabrication procedure:

- Cleaning the master wafer (O_2 -plasma, base-piranha, O_2 -plasma)
- Apply Fluoro-monolayer to the master
- Spin-coat X-PDMS on master (hard mask)
- Spin-coat I-PDMS on master (intermediate mask)
- HF-treat the willow-glass carrier
- Prime the willow-glass with Dow Corning primer [103]

- Apply PDMS (soft mask) to the willow-glass
- Bond the glass to the coated master in a thermally-assisted bonding tool
- Separate the master from the stamp with IPA

3.4 Preparation of samples and SCIL imprint

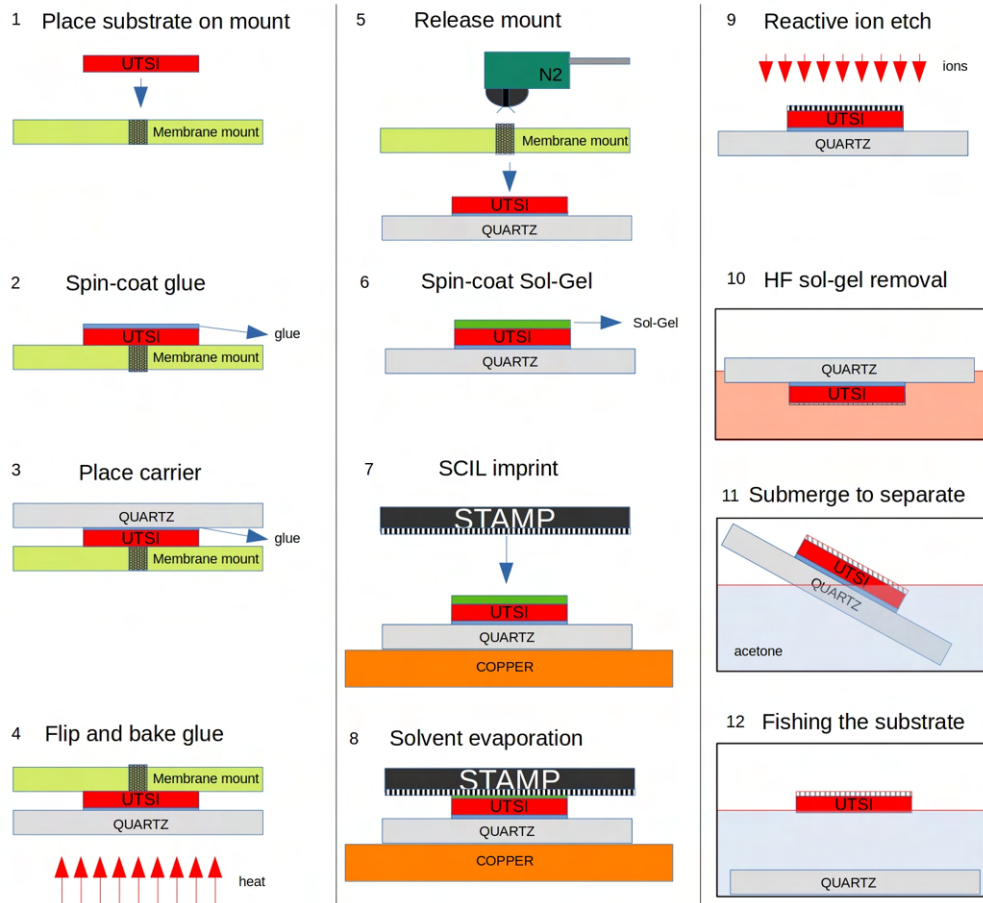


FIGURE 3.5: Exemplary process flow chart of bonding an ultra-thin substrate "UTSI" to a carrier "QUARTZ" (1-5), imprinting the substrate with a SCIL stamp (6-8), using reactive-ion etch for pattern-transfer into the substrate (9), removing residual resist (10), and dissolving the adhesive to retrieve the free-standing substrate (11-12). The procedure as visualized is applicable when the Al-mount is used and in case of the PEEK mount, steps (4) & (5) are exchanged, where the use of the reverse-blow with N₂ is optional in both cases. Step (9) summarizes the three individual etch steps explained in sec. 3.5, and between (11) and (12) an additional bath in IPA is useful to rinse the substrate from acetone residue.

Fig. 3.5 shows a process flow chart for the steps outlined below, beginning with bonding of the thin substrate to a carrier, followed by spin coating the resist and imprinting the same with a SCIL stamp. Subsequently, reactive-ion etching transfers the pattern from the resist layer into the substrate, after which an HF step removes the residual resist. Additional processes on the bonded stack, e.g. passivation and

application of an anti-reflective coating can now be executed and concluded with debonding the substrate by submersion in a suitable solvent, after which the substrate can be separated from the carrier by sliding into a bath of H₂O at a shallow angle.

During the patterning step by soft conformal imprint lithography a force needs to be applied in order to distribute the sol-gel into the grooves of the stamp and remove it from the protrusions of the same. At the time of the imprint, the solvents present in the sol-gel cause an adhesion to both the silicon substrate to be imprinted and the stamp surface, while capillary forces pull the sol-gel into the grooves of the latter. After evaporation of the solvents and due to selenization of the stamp surface, the hydrophilic SiO₂-remainder and the hydrophobic PDMS stamp exhibit much weaker adhesion than observed at the substrate-sol-gel interface, which allows removal of the stamp without alterations of the sol-gel structure previously obtained. The stress inflicted to the membrane during the imprint procedure needs to be countered by a flat, sturdy back support, which also serves to keep the substrate from sticking to the stamp at the time of separation. Temporarily bonding the thin silicon wafers or IBC solar cells to a suitable substrate using an appropriate adhesive proves itself as a reliable solution as previously explained in section 3.1. If no carrier is used, the thin wafer will stick to the stamp after solvent evaporation and likely break upon separation trials. A complete set of step-by-step instructions of the bonding procedure is found in appendix B, of which the following highlights important considerations.

In order to transfer the substrate to a (quartz-) carrier, the latter is placed onto the membrane and mount directly after spin coating the adhesive and a light application of pressure is used to make homogeneous contact and remove air from the interface. When a spacer is used, the adhesion should already be sufficient to lift off the carrier with the substrate attached while leaving behind the mount. The carrier is flipped and placed onto a hotplate with the substrate facing up for a duration of 180 s at 120 °C. Without a spacer and when using the aluminum mount, the entire stack consisting of mount, membrane, and carrier can be taken from the spin coater, flipped and baked on the hotplate using equivalent conditions (as shown in fig. 3.5). The applied heat will release the mount from the membrane through thermal expansion, since the coefficients of linear thermal expansion for aluminum/brass differ from those of glass/silicon by about a factor of 3-4 [104]. The same technique is not suitable for the release of thinned IBC solar cells from the aluminum mount, since the cells contain both metal and silicon and tend to bend in the longitudinal direction of their metallic bus bars. In this case, the transfer to the carrier can be aided by application of over-pressure through the backside of the mount, such that the pressure gradient is reversed with respect to the situation on the spin coater. This will release the IBC cell (or UTSi) with a pressure wave expanding from the center towards the circumference of the bonded interface and result in an equally homogeneous and void-free contact. The following baking step is performed progressively on the cells, starting from 50 °C for 5 min and finishing at 100 °C in 10 °C-steps with a duration of 5 min each, counted after the hotplate reached the current temperature step. This way, the resulting bonding strength of the hardening PMMA that stays superior to the temperature-induced bending of the cell. The optimum thickness of the PMMA layer employed for bonding was found to be around 400 nm in case of a bare silicon substrate and (800-1000) nm for bonding the IBC cells, which have higher surface irregularities due to the parylene-coated inter-digitated contacts on the backside. The optimum results as a trade-off between conformality to the substrate and a minimum edge-bead, where the former decreases with thinner layers and the latter increases with layer thickness, resulting in inhomogeneity of thickness from the center

to the edge of the layer.

Imprinting the substrate/cell is performed by first placing the carrier with the substrate facing upwards on the spin coater and applying the sol-gel with spin parameters given in table 3.4. Subsequently, the stack is quickly placed onto an extremely flat surface, backed by a thick, rigid base. Afterwards, the stamp is aligned above the substrate and slowly brought into contact with the same, until its weight is entirely supported by the substrate-carrier stack. Pressure is applied onto the stamp beginning from one edge of the pattern and expanded to the opposite edge in a wave-like motion. While in automated SCIL devices, compressed air is used to produce the pressure-wave, the same can be achieved using the experimenter's finger (preferably thumb) at lab-scale imprints yielding comparable results. The wave-like motion is repeated 3-4 times with increasing pressure, until no trapped air remains throughout the patterned region of the stamp.

The rotation speed of 2400 RPM given in table 3.4 is calibrated to result in a thick-

TABLE 3.4: Parameters for spin coating the sol-gel onto thin substrates for SCIL imprint. No gear set is used in this case (open bowl).

Step #	Time / s	Rotation / RPM	Acceleration / RPM s^{-1}	Lid closed (y/n)
1	5	-	-	y
2	10	2400	1000	y
3	-	-	-	n

ness of (50 – 60) nm, which for a pattern with 50 % silicon filling fraction (Spinodal pattern) results in approximately (100-120) nm high structures, thus utilizing about the entire depth of the grooves present in the stamp. For patterns with different filling fractions, i.e. HUD-Honeycomb $\approx 33\%$, HUD holes $\approx 72\%$, slightly lower or higher rotation speeds can be chosen to obtain a mask of equivalent aspect ratio.

The solvents present in the sol-gel evaporate quickly, such that the stamp can already be released from the substrate after curing in air for approximately 8-10 min. For this step, the stamp is lifted and flipped over with the substrate/carrier still attached, such that the latter is facing up. Upon bending the glass sheet carrying the SCIL stamp, the edges of the rigid substrate-carrier stack separate from the circumference of the stamp and a pair of closed tweezers inserted in-between stamp and carrier release the bond across the entire interface solely through their restoring force, after which the substrate-carrier stack can readily be picked up. The stamp is cleaned and made ready for reuse by rinsing the same first with de-ionized water, followed by ethanol, and H_2O once more, before it is blown dry with a nitrogen gun. The imprinted samples are now set for etching with RIE.

3.5 Reactive-ion etching for pattern transfer

Reactive-ion etching (RIE) is a plasma etching technique featuring a gaseous etchant that produces volatile products from reactions with a solid. Next to the chemical reactions, a number of additional mechanisms are active in RIE to facilitate the removal of material. The plasma discharge produces both ions and excited neutrals, which cause ionization, excitation, and dissociation of the target material. In contrast to wet etching where liquid etchants are used, plasma etching allows for fabrication of high aspect ratio structures, due to an unprecedented degree of achievable anisotropy [91]. Where diffusion limits with liquid etchants become problematic, straight walls are required and underetching must be prohibited, reactive-ion

etching is often the instrument of choice. The required vacuum on the other hand, together with little margin for parameter deviations like mixture, temperature and flow rates render RIE usually slower and more expensive than wet-chemical techniques.

Reactive-ion etching is used for etching three different layers in the course of fabricating the HUD-patterned surfaces presented in this work. The largest depth and highest degree of anisotropy are required for the final step, the silicon etch of 200 nm depth.

Pure silicon is typically and most easily etched by halogens, like fluorides, chlorides, and bromides. The Si-halogen compounds are volatile at room temperature and the reactions from Si-Si bonds to these compounds are thermodynamically favored, such that additional ion bombardment is only employed to increase anisotropy [91].

The RIE system utilized for this work is the PlasmalabPRO 100 [105][106]. The system features two individual ion generators/accelerators, a radio frequency (RF) electrostatic generator up to 300 W and an inductively-coupled plasma (ICP) generator up to 3 kW input power. The etch recipe for silicon was previously optimized by the AMOLF-NanoLab staff [107] and uses an HBr/O₂ mixture of 48 sccm : 2 sccm ratio and flow rates at a temperature of 60 °C. The oxygen content helps both to achieve straight walls by passivating silicon in the direction normal to the plasma acceleration and by breaking Si-Si bonds through bombardment in the direction parallel to it. The silicon etch is initiated by a short chloride plasma etching step to remove the native SiO₂ layer, which is hardly being attacked by the subsequent bromide-oxygen mixture. All parameters of the silicon etch are summarized in table 3.5.

TABLE 3.5: Parameters of Si-etch in PlasmalabPRO 100 RIE etcher. Initiation by Cl₂ removes the native oxide layer. Flush purges the remaining Cl₂ from the chamber and replace it with the HBr/O₂-mixture of the main etch, pump re-establishes the chamber vacuum before the main etch "Si-etch" commences. The main etch speed was calibrated at 3.4 ± 0.2 nm/s for the structures under consideration.

Step	Time / s	Gases	Flow / sccm	RF pow. / W	ICP pow. / kW
Init	11	Cl ₂	50	30	750
Flush	60	HBr:O ₂	48:2	0	0
Pump	60	-	-	0	0
Si-etch	60	HBr:O ₂	48:2	30	750

For samples imprinted with a SCIL stamp, the resulting etch mask is not comprised of a polymeric resist as in the case of dosage tests and master fabrication by electron-beam lithography, but instead consists of a porous SiO₂-layer on top of the native oxide layer of the silicon substrates. The imprint removes most of the sol-gel from the protruding parts of the pattern on the stamp, which gets pushed and pulled into the grooves of the same as explained before, yet a residual layer of sol-gel remains in place and converts to porous silicon dioxide during evaporation of the solvents. This layer needs to be removed as well as the underlying native oxide. SiO₂ is removed by the initiation step with Cl₂ as mentioned above, but the different quality of oxide present in these layers results in different etch rates for the native oxide and residual layer and is not calibrated on the RIE system utilized. Another etch recipe specifically optimized for removing the residual sol-gel layer employs a 1 : 1 mixture of CHF₃ and Ar at low forward power of 67 W RF and zero ICP, with the

temperature in chamber set to 20 °C. Both flow rates are set to 25 sccm and the resulting etch rate is calibrated at (0.5 ± 0.3) nm of porous SiO₂ per second. It is found by experiment that the etch rate for native oxide with this recipe is significantly lower, where in addition also the quality of native SiO₂ exhibits a strong influence on the rate of removal of the same. For these reasons, both CHF₃/Ar- and Cl₂- etch steps are retained in the recipe for etching SCIL-imprinted samples, where the former is calibrated to remove the residual layer and the latter to remove the native oxide, before commencing the bromide etch into the silicon. The duration for removing the residual sol-gel layer of the structures reliably is found to be (120 ± 10) s.

3.6 Removal of residual imprint-resist layers

After transfer of the pattern from the SiO₂ mask into the silicon using reactive-ion etching as explained in the previous section, the residual silicon dioxide of the mask is removed by dipping the sample into hydrofluoric acid (HF) at 1 % concentration for 90 s. Afterwards, the sample is rinsed by short immersion in H₂O, followed by IPA and blow dried with a nitrogen gun.

An attempt to circumvent the use of HF involves spin coating a thin layer of a polymeric resist in-between the native oxide on the silicon and the sol-gel layer to be imprinted with SCIL. This would allow the lifting off the remainder of the SiO₂-mask on top of the resist in a less dangerous solution such as acetone, if for example PMMA is used here as well. Such attempts were unsuccessful when using either 200 nm or 350 nm of PMMA layer thickness, owing to a change of the composition of the PMMA during RIE, which renders the PMMA insoluble in acetone afterwards.

3.7 Results and Discussion

The bonding of thin substrates and solar cells using the special mounts and methods described in the previous sections as well as the appendix B reflects the current state of knowledge and may possibly be improved in order to further minimize the chance of breaking the substrate during the process. Engaging in optimizations is mainly limited by the availability of suitable test substrates, i.e. mono-crystalline wafers of 10 µm thickness and 2.54 mm in diameter, which are most prone to damage during bonding and at the same time very expensive and difficult to obtain. An alternative for obtaining a number of bonded test substrates at once, though at lower bonding quality, is to glue large sheets of thin Si foil to a suitable wafer using an adhesive of choice. Up to a diameter of 6 inches, a carrier wafer can easily be spin coated with e.g. PMMA and then flipped and placed onto a sheet of thin foil. After cutting around the wafer edge, the same can be placed onto a hotplate for curing the PMMA. The process will most likely deform the foil from degassing of the adhesive in some places, but the overall yield still warrants the procedure. 20 µm thick Si foil bonded this way was obtained from the photonic materials group at AMOLF and used for imprints described later in this section.

The special spin coating mounts made from PEEK featuring a nylon filter piece in the center perform well after their surface has been polished to a very high degree, but retain this state only for a short time and need to be polished again after a few uses, if over pressure is applied through the back of the mount, or chemicals are used for cleaning or to facilitate substrate release. The aluminum mount with a brass filter as the center piece on the other hand is the first of its kind and dimensions of its features can still be optimized in later versions, but it shows remarkable performance with

somewhat thicker substrates of $30\text{ }\mu\text{m}$ with the release through thermal expansion and is more resistant to chemicals than the nylon counterpart.

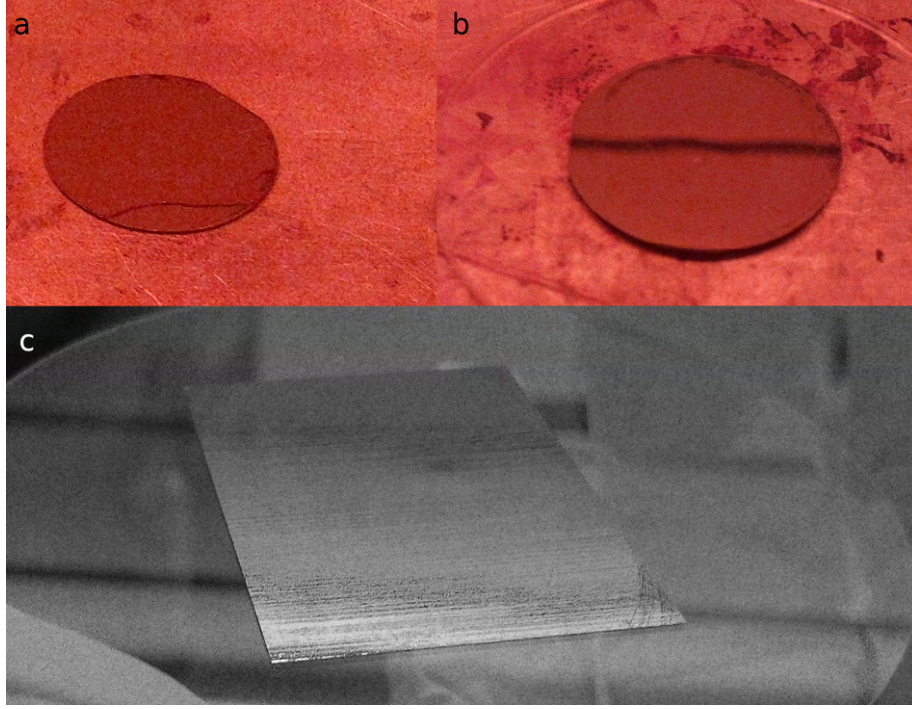


FIGURE 3.6: Ultra-thin silicon substrates ($\varnothing 2.54\text{ mm}$) and a thinned IBC solar cell bonded to quartz wafers. **a** A $10\text{ }\mu\text{m}$ membrane baking on the hotplate on a 3-inch quartz wafer of $500\text{ }\mu\text{m}$ thickness. **b** $30\text{ }\mu\text{m}$ membrane bonded to a 2-inch quartz wafer of 1.6 mm thickness on hotplate. **c** Large piece of an IBC cell $\approx (80 - 100)\text{ }\mu\text{m}$ absorber thickness and dimensions roughly $36 \times 48\text{ mm}^2$ in the plane of the cell bonded to a 3-inch quartz wafer. Residual PMMA is visible around the circumference in **b**, which is removed before spin coating the imprint resist.

Of critical importance is the difference in diameter of the center protrusion of the mount and the substrate. The substrate needs to extend about a millimeter beyond the rim of the protrusion in order to prevent the spin-coated adhesive from entering the interface between mount and substrate at the circumference of the same. The overhang will cause a small amount of adhesive to be deposited on the underside of the substrate from the slight vacuum created there but not result in the substrate being glued to the mount. After bonding to the carrier, the residual PMMA in this case can be washed off with acetone/IPA when spinning on the spin coater with open lid at low RPM. A $10\text{ }\mu\text{m}$ - (**a**) and a $30\text{ }\mu\text{m}$ -thin substrate (**b**), as well as a piece of thinned IBC cell (**c**) bonded to quartz wafers are shown in the photographs in fig. 3.6.

The dosage tests performed in the course of making the master wafer for SCIL with electron-beam lithography may be compared among each other by introduction of another figure of merit, which is given by considering the characteristic HUD values k_1, k_2 . The ideal radial profile in the surface-parallel momentum plane is given by a gate function that equals one when $k_1 < k < k_2$ and zero otherwise, where k is the in-plane spatial frequency. The third figure of merit is then given as well via eq. (3.1), where now $I_d(k) \rightarrow I_g(k)$, the intensity distribution of the design values is

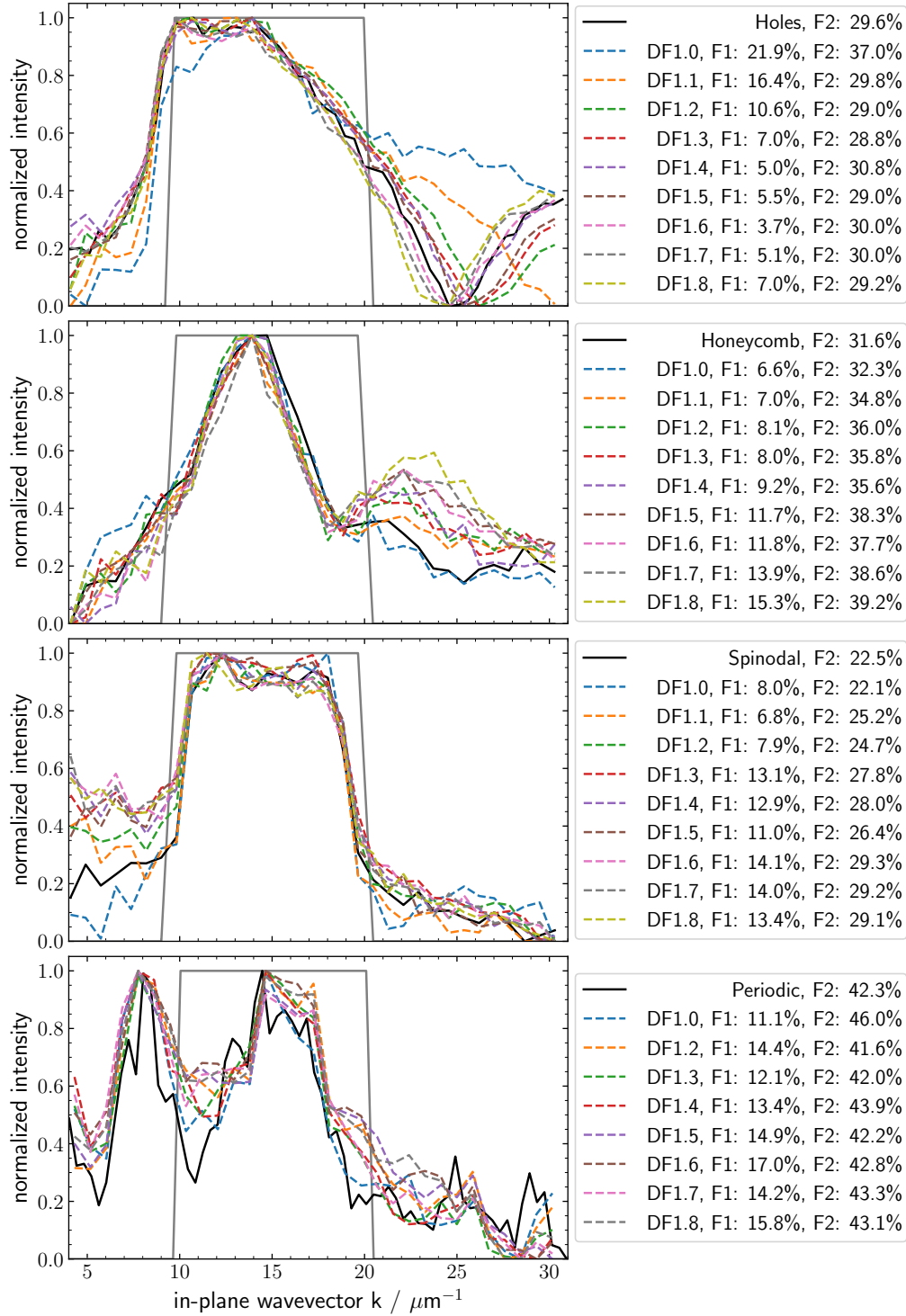


FIGURE 3.7: Comparison of momentum-space radial profiles among the different design structures and to a gate function (grey) defined by considering the characteristic HUD values k_1, k_2 . The figure of merits, F1 and F2 are defined via eq.(3.1), where for F1, $I_d(k)$ corresponds to the design's intensity function and for F2 to a gate function, where $I_d(k) = 1 \forall k \in [k_1, k_2] \wedge I_d(k) = 0$ else.

replaced by the intensity of the gate function defined above. The results for all four structures are displayed together in fig. 3.7 where "F1" denotes the figure of merit calculated from the design values and "F2" the one just described.

From the third figure of merit given in the legends in fig. 3.7, the least deviation from the gate function is achieved by the Spinodal pattern with 22.5 %, followed by the HUD holes design with 29.6 %. As expected, the optimized periodic structure shows the largest deviation, since it is not from the stealthy hyperuniform class and exhibits significant intensity also below the critical wavevector k_1 . Between the HUD holes and the HUD honeycomb, the radial profile of the latter deviates more from a square shape and receives a third figure of merit of 31.6 %. From the legends found in fig. 3.7, it can be deduced that a dose factor of about 1.4-1.5 very accurately reproduces the intensity profile of the design in most of the different structures, which also corresponds to the best match in Si filling fraction as seen in fig. 3.3 for honeycomb and fig. C.6-C.8 in appendix C for the remaining structures. As a consequence, a dose of about $(145 \pm 10) \mu\text{C cm}^{-2}$ is set for the exposure of all master wafers.

With the SCIL stamp featuring the Spinodal pattern fabricated first, a number of imprints on a variety of substrates are performed. From the manufacturing process, some particles may remain on the pattern or in the grooves thereof and are removed by one or two initiation imprints on regular 500 μm thick silicon wafers. Afterwards, the stamp is ready-to-use and an imprint on a readily bonded thin substrate, including curing of the resist and stamp-sample separation, can be executed inside of 15 min. The first imprint on 10 μm thick, one inch silicon wafer is depicted in fig. 3.8a, where the amount of sol-gel used could not be fully taken up by the grooves. In combination with a short curing time of only 6 min and too little pressure applied during the imprint, the stamp slid laterally across the membrane when separation of the two was attempted, which removed the imprint in some regions visible at 2 in fig. 3.8a and 3.8c. Consequently, a longer curing duration of 9 min was introduced and different spin parameters given in table 3.4 adopted for subsequent imprints, which prevented the issue from occurring again.

The IBC cell shown in fig. 3.6 is imprinted with the improved parameters and shows a full area replica of the structure on the stamp. The IBC-cell thinning procedure involving HNA, a mixture of acetic : nitric : hydrofluoric acid (ratio 8:3:1), unveils the crystal facets visible as diamonds or pyramids in fig. 3.8c that are up to about 50 μm large. The DIC microscope image in fig. 3.8d confirms that most of the pyramids are imprinted nonetheless through the high degree of conformality achievable with SCIL.

An approximately $30 \times 50 \text{ mm}$ piece of 20 μm thick Si foil bonded to a large 6-inch wafer as explained above is cleaved and imprinted with the Spinodal stamp. Following the RIE etch, where a Si-etch duration of 70 s was employed, the sample is examined with SEM before and after it is dipped in HF. Fig. 3.9a shows the sample on the SEM-mount with the $(2 \times 2) \text{ cm}^2$ patterned area in the center being highlighted through specular reflection, while in fig. 3.9b a 20x magnified DIC microscope image of the same pattern is displayed (scale bar is 100 μm). The dark grid lines in b are due to the large-area electron-beam lithography process using dump-file exposure, as explained in sec. 3.2, where the stitching of adjacent fields of unit cell size $(200 \times 200) \mu\text{m}$ in this case is only accurate to about (20-30) nm. As a result, the pattern is minutely stretched in these regions, leading to a strong interference in optical microscopy, while in SEM they appear only slightly brighter with respect to

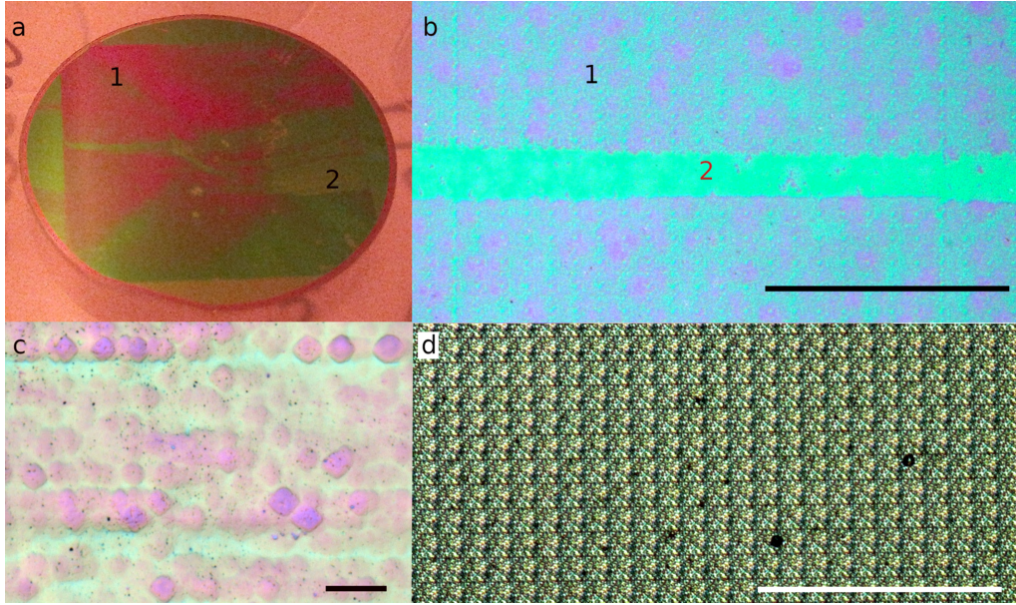


FIGURE 3.8: Spinodal SCIL imprints on 10 μm Si membrane (**a** and **b**) and IBC solar cell shown in fig.3.6 (**c** and **d**). **a** Imprinted area is specularly reflected in a reddish color at **1** and a region of unsuccessful imprint is located at **2**. **b** Bright-field optical microscope image of **a** at 20x magnification showing imprinted pattern at **1** and non-imprinted areas at **2**. **c** 5x magnified bright-field image of IBC solar cell with large pyramids visible from the HNA-etch that thinned down the cell to $\approx (50 - 80) \mu\text{m}$. The stamp is capable of conformally imprinting also on the large pyramids as shown in the 20x magnified DIC-image in **d**. All scale bars are 100 μm and correspond to 10x the unit cell dimension of the Spinodal pattern, visible as an array of squares in **b** and **c**.

the rest of the area. Scanning-electron microscope images before and after dipping the sample in HF for 90 s are displayed in fig. 3.9c and **d**, respectively, where the scale bar corresponds to 500 nm distance in both cases. The structure depth in **c** is about $(350 \pm 10) \text{ nm}$ and the residual sol-gel can be seen as a bright layer forming the top-surface. After HF-treatment, the SiO_2 -remainder as well as the native oxide is removed and consequently less contrast is seen in the post-HF SEM image in **d**. The depth in this image is calibrated at $(430 \pm 10) \text{ nm}$ and the circular particles are found throughout the pattern at each location that was imaged and assumed to be SiO_2 -particles adsorbed to the surface when removing the sample from the HF bath. The increase in depth from before and after the HF dipping remains to be evaluated by repetition on another sample using equal conditions, but would in any case be unexpected and the discrepancy is tentatively attributed to inhomogeneity of the etch depth across the sample as well as inaccuracy of the pixel-based measuring technique with the SEM at different inclinations (30° in **c** and 35° in **d**).

From a top view SEM image of the sample shown in fig. 3.9, the radially-averaged profile of k-space intensity as described in sec. 3.2 is obtained and compared to the design using both figures of merit from above in fig. 3.10. From the legend in the same figure, it is concluded that the structure replicated on the thin substrate using the SCIL stamp deviates about 17% on average from the design file, while the Si filling fraction is calibrated at $(61 \pm 3\%)$, about 7% higher than the designed value.

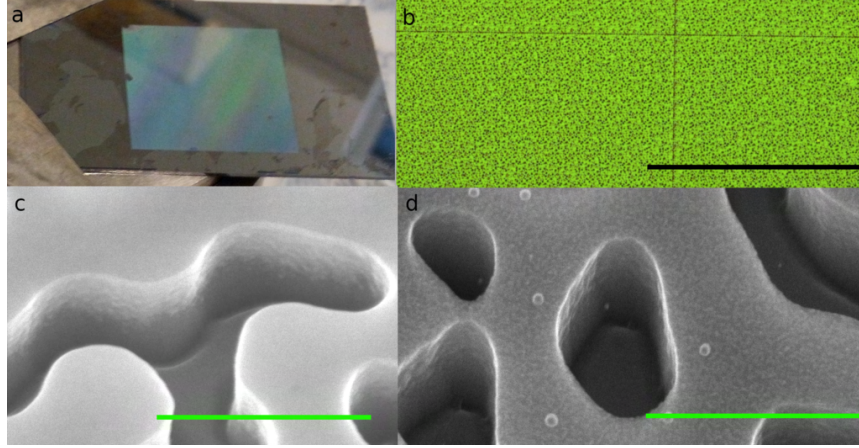


FIGURE 3.9: A photograph **a**, an optical microscope image **b**, and two SEM images **c** and **d** of a 20 μm thick Si foil imprinted with Spinodal stamp. The Si foil bonded to a 1 mm thick-Si carrier shows specular reflection in the patterned area in **a**. The DIC-microscope image of the patterned area in **b** shows grid lines from EBL stitching during the master exposure intersecting the scale bar. The same corresponds to 100 μm . **c** SEM image after etching and prior to the removal of residual resist with HF. **d** SEM image after HF-treatment. scale bars in **c** and **d** are 500 nm.

In particular, the frequency range below $k = 10 \mu\text{m}^{-1}$ shows significantly increased normalized intensity compared with the design values.

The sample is debonded from its thick carrier wafer by immersion in acetone for

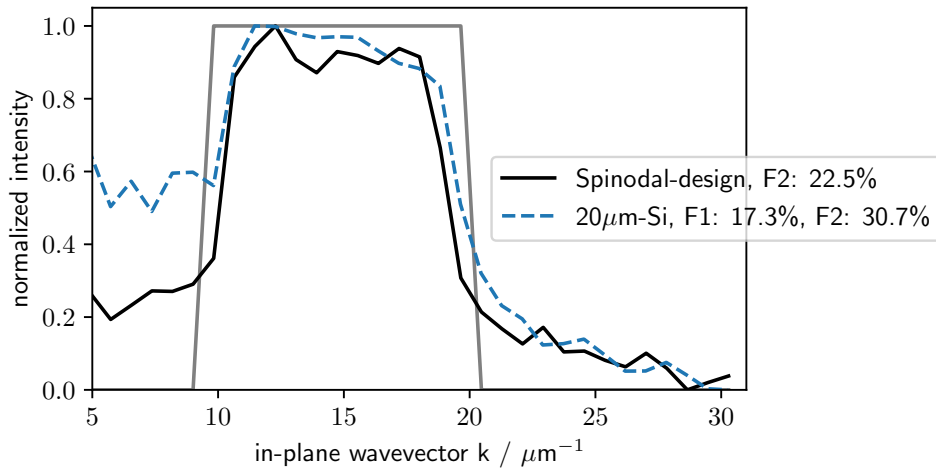


FIGURE 3.10: Normalized intensity versus in-plane wavevector of Fourier-transformed SEM image from Spinodal pattern on 20 μm Si foil (dashed line), compared with the radial profile of the design (solid line). $F1$ corresponds to std-deviation between the curves, while $F2$ denotes the deviation to a gate function shown in grey.

24 h and transferred to a microscope cover glass, to which it is directly bonded using IPA as a contact forming agent. After the IPA evaporation in air, the glass with patterned membrane can be optically characterized in its bare state. The reflection- and transmission- measurements depicted in fig. 3.10 were performed by Bsc Jelena

Dolecek, who as her master project investigates into effective surface passivation of the hyperuniform structures fabricated on thin substrates presented in this thesis. Without an anti-reflective coating and the surface being left in the state after HF-dipping, the transmission through the sample is lowered by about 4 % compared with an unpatterned reference foil to a value of 6 %, while reflection is reduced by approximately 20 % through application of the texture. These values were found by integrating over the convolution of the measured spectra with the AM1.5 spectrum in the wavelength range $\lambda \in [400, 1050]$ nm as before. Absorbance is calibrated via $A = 1 - T - R$ and reached an integrated, spectrally averaged value of 80 % in case of the patterned foil, while the reference absorbed 56 %. Also shown in fig. 3.11 as dotted lines are results from FDTD simulation of 20 μm silicon with 200 nm Spinodal pattern and without anti-reflective coating on top of a SiO_2 carrier. In this simulation, the transmission monitor is placed inside the SiO_2 layer 50 nm from the Si- SiO_2 interface and the simulation area in the plane of the silicon is $(2 \mu\text{m})^2$. The difference in transmission can be attributed to the idealization in the simulation, since in the experiment there are additional interfaces arising from the direct bonding to a microscope cover slip with IPA and the thickness of the cover slip of 150 μm , behind which transmission is recorded. The patterned layer on top of the Si-foil of the experiment is about 2 times thicker than in the simulation, causing a difference also in reflection in addition to the experimental uncertainties. As a result, the spectrally averaged absorption is 11 % higher in the experiment with the patterned foil compared to the simulated value, but all graphs show very similar trends and indicate good agreement between experiment and simulation, despite the mentioned influences.

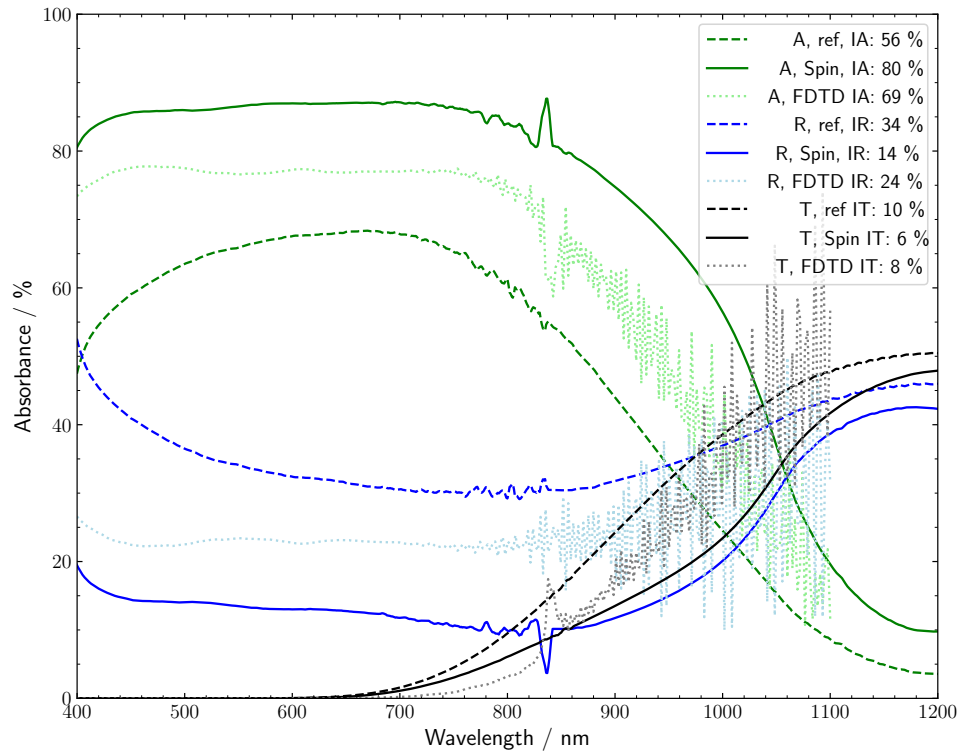


FIGURE 3.11: Absorbance measured optically with UVVIS-spectrometer on native 20 μm Si foil (ref) and compared with Spinodal-imprinted 20 μm Si foil (Spin), for which both samples are directly bonded to a microscope cover glass. Spectrally averaged absorption/reflection/transmission ($IA/IR/IT$) is found through convolution with AM1.5 irradiance data [43]. Also shown as dotted lines and in lighter colors are FDTD simulation results of a 20 μm Si slab on glass (SiO_2) and with Spinodal pattern in the top 200 nm of the silicon layer, which is not infiltrated and covered with anti-reflective coating in this case.

Chapter 4

Conclusion & Outlook

The goal to develop a feasible approach for quickly obtaining large-scale, hyperuniform patterns on ultra-thin Si substrates and thinned IBC solar cells and facilitate their (optical) characterization was accomplished. The approach relies on temporary bonding of the fragile substrates to a transparent carrier, for which a special tool was invented that ensures homogeneous contact throughout the bonding region and protects the device from breaking during the procedure. Substrate conformal imprint lithography (SCIL) was chosen as a means for imprinting nanostructures in a short time, which reproduced the design over 4 cm^2 -areas on ultra-thin devices with a standard deviation of about 17 %, obtained through Fourier-analysis, while the filling-fraction differed by approximately 7 %. The master wafers required for making SCIL-stamps were fabricated using electron-beam lithography, which was optimized to complete the exposure of 4 cm^2 in under two days. Several multi-step, reactive-ion etch recipes were investigated and a reliable procedure for obtaining arbitrary structure-depths of hyperuniform patterns on SCIL-imprinted devices deduced. The patterned devices in their bonded state can be processed further akin to standard wafers without major limitations after a single-step HF treatment to remove the residual imprint resist, and debonding from the carrier can be performed at any time to retrieve the free-standing substrate.

Preliminary optical characterization of a $20\text{ }\mu\text{m}$ thick silicon slab after patterning and debonding yielded an absorbance enhancement of approximately 46 % over an unpatterned reference case, where absorption is still expected to improve substantially when an anti-reflection coating is applied. As seen in fig 2.17 for a bare slab of $10\text{ }\mu\text{m}$ thickness, applying an anti-reflective coating to the front surface increased absorption by about 44 %.

Molding SCIL stamps from the HUD master wafers fabricated in the course of this project was not fully completed in the available time and so far, experiments could only be carried out with the Spinodal stamp, which was completed first. Both remaining hyperuniform stamps have been fabricated in the meantime and test imprints on thick substrates allow the conclusion that their performance can be expected equivalent to the Spinodal one, such that a stamp with the optimized periodic pattern is the only one yet to be made. An ongoing project into effective surfaces passivation of HUD-patterned thin-films will make use of all stamps available now in order to pattern the substrates used for passivation experiments according to the procedure presented in this work.

The absorbance in slabs with hyperuniform patterns estimated via coupled-mode theory predict a significant absorption enhancement also for $10\text{ }\mu\text{m}$ thick absorbers, though the targeted structure factor with characteristic HUD values k_1, k_2 of the investigated textures was optimized for $1\text{ }\mu\text{m}$ thickness. The predicted optimum k_1, k_2 values depend on the mode data used for evaluating the absorbance, and the values

previously obtained in [35] were not exactly recovered by any of the inquired waveguide configurations. The investigation into the coupled-mode theory approach can be expanded to improve certain estimates, e.g. the number of channels, and the resulting implications and predictions further compared with FDTD simulations featuring HUD structures of varying characteristic values k_1, k_2 , which in turn would allow a conclusion on both the theoretical approach as well as the set of mode data employed.

From fig. 2.16, it can be deduced that reducing Fabry-Pérot oscillations increases absorption, which is accomplished by employing a hyperuniform pattern. Another light trapping mechanism involving multi-resonant absorption has shown capability to exceed the lambertian limit in some cases [19]. Positioning resonant scatterers in an array with hyperuniform spatial distribution would combine both effects and open up the possibility of "flattening" the FP-oscillations even further, and in addition could be tailored to target a wavelength range, where many photons of the solar spectrum are available. So far, only a structure etched into the absorber has been considered, though patterning the anti-reflection coating or the back-reflector could in principle provide similar enhancement of absorbance with less fabrication steps required. Also, a combination of patterned layers on front- and backside could be considered, where each layer targets a specific portion of wavelengths or incident angles for more complete absorption. Furthermore, the hyperuniform patterns offer new perspectives for tandem cells, where a secondary ultra-thin PV cell with larger bandgap is placed on top of a silicon cell. With a HUD-structure situated at their mutual boundary, corresponding parts of the incident solar spectrum would be selectively reflected or transmitted through a tunable, built-in photonic bandgap.

Acknowledgements

This thesis was written during the ongoing pandemic in the year 2020-2021 and the lab work herein presented was made possible only by the conjoint effort of the great people at AMOLF, who worked wonders to keep the workplace accessible for a reduced number of people and making available all equipment for use in a safe and organized fashion. The contribution of all departments at AMOLF to the possibility of doing experimental physics and developing new processes during this crisis of unprecedented global scale is awe inspiring and deserves many special thanks. Not all of these dedicated people can be named in this acknowledgment and the names mentioned here were either directly involved in my project or have made essential contributions to the success of the same. Beginning with my wise and wonderful project leader, Esther Alarcon-Llado, I would like to thank you for picking me and providing me with all your capable support from day one. You have made valuable contributions not only to all parts of this thesis but also to my personal growth and I want to thank you especially for aiding to build my confidence and turning me into a better scientist with every discussion that we held. To my supervisor, Nasim Tavakoli, I owe profound thanks for giving life to the idea of my project and supplying a seemingly endless stream of positive reinforcement, capable support, as well as creative ideas to tackle emerging problems. Thanks to Albert Polman for valuable discussions and insights as well as the bridges you built in these trying times to connect me and my research with others in the field. Thank you Stefan Tabernig for perfecting the thinning of IBC cells and supplying them in ample quantities for experiments in this work, as well as your support in many situations. Thanks to Dion Ursem for valuable design input, suggestions and manufacture of the spin-coating mounts. Thanks to Dimitry Lamers for fabricating the SCIL stamps and giving training and tips for many clean-room processes, and for further training and insightful discussions also thanks to Bob Drent, Igor Hoogsteder, Yorick Bleiji, Mark Aarts, Femius Koenderink, Tom Veeken, Andrea Cordaro, and Jente Vandersmissen. Last but not least, I want to thank all current and former members of the 3D Photovoltaics group at AMOLF for their support, kindness and efforts to counter isolation and disconnection brought about by the total lockdown during several months of the project.

Bibliography

- [1] J. H. Perkins, "Special report on renewable energy sources and climate change mitigation: 2011. intergovernmental panel on climate change, working group iii—mitigation of climate change.," *Cambridge University Press, Cambridge, England.*, 2012. DOI: 10.1017/s1466046612000233.
- [2] United Nations / Framework Convention on Climate Change, "Adoption of the paris agreement, 21st conference of the parties," *Report of the Conference of the Parties to the United Nations Framework Convention on Climate Change (21st Session,Paris)*, 2015.
- [3] *Renewable power generation by technology in the sustainable development scenario, 2000-2030*, IEA, 2021. [Online]. Available: <https://www.iea.org/reports/solar-pv> (visited on 08/07/2021).
- [4] Z. Liu, S. E. Sofia, H. S. Laine, M. Woodhouse, S. Wiegbold, I. M. Peters, and T. Buonassisi, "Revisiting thin silicon for photovoltaics: A technoeconomic perspective," *Energy & Environmental Science*, 2020. DOI: 10.1039/c9ee02452b.
- [5] Our World In Data, *Installed solar energy capacity*, 2021. [Online]. Available: <https://ourworldindata.org/grapher/installed-solar-pv-capacity> (visited on 08/07/2021).
- [6] SEIA Comms Team, *A Look Back at Solar Milestones of the 2010s*, 2020. [Online]. Available: <https://www.seia.org/blog/2010s-solar-milestones> (visited on 08/17/2021).
- [7] E. Bellini, *How solar parks change landscape perception*, 2020. [Online]. Available: <https://www.pv-magazine.com/2020/02/06/how-solar-parks-change-landscape-perception/> (visited on 08/07/2021).
- [8] C. Flatt, *Solar power becomes nightmare for some klickitat county residents*, 2021. [Online]. Available: <https://crosscut.com/environment/2021/05/solar-power-becomes-nightmare-some-klickitat-county-residents> (visited on 08/04/2021).
- [9] S. M. Nir, *He set up a big solar farm. his neighbors hated it*, New York Times, 2020. [Online]. Available: <https://www.nytimes.com/2020/03/18/nyregion/solar-energy-farms-ny.html> (visited on 08/04/2021).
- [10] S. Bhattacharya and S. John, "Beyond 30% conversion efficiency in silicon solar cells: A numerical demonstration," *Scientific Reports*, 2019. DOI: 10.1038/s41598-019-48981-w.
- [11] P. H. Wang, R.-E. Nowak, S. Geißendörfer, M. Vehse, N. Reininghaus, O. Sergeev, K. von Maydell, A. G. Brolo, and C. Agert, "Cost-effective nanostructured thin-film solar cell with enhanced absorption," *Applied Physics Letters*, 2014. DOI: 10.1063/1.4901167.

- [12] R. Cariou, W. Chen, I. Cosme-Bolanos, J.-L. Maurice, M. Foldyna, V. Depauw, G. Patriarche, A. Gaucher, A. Cattoni, I. Massiot, S. Collin, E. Cadel, P. Pareige, and P. R. i Cabarrocas, "Ultrathin PECVD epitaxial si solar cells on glass via low-temperature transfer process," *Progress in Photovoltaics: Research and Applications*, 2016. DOI: 10.1002/pip.2762.
- [13] V. Benda and L. Černá, "PV cells and modules – state of the art, limits and trends," *Heliyon*, 2020. DOI: 10.1016/j.heliyon.2020.e05666.
- [14] A. Bozzola, M. Liscidini, and L. C. Andreani, "Photonic light-trapping versus lambertian limits in thin film silicon solar cells with 1d and 2d periodic patterns," *Optics Express*, 2012. DOI: 10.1364/oe.20.00a224.
- [15] A. Gaucher, A. Cattoni, C. Dupuis, W. Chen, R. Cariou, M. Foldyna, L. Lalouat, E. Drouard, C. Seassal, P. R. i Cabarrocas, and S. Collin, "Ultrathin epitaxial silicon solar cells with inverted nanopyramid arrays for efficient light trapping," *Nano Letters*, 2016. DOI: 10.1021/acs.nanolett.6b01240.
- [16] S. Jeong, M. D. McGehee, and Y. Cui, "All-back-contact ultra-thin silicon nanocone solar cells with 13.7% power conversion efficiency," *Nature Communications*, 2013. DOI: 10.1038/ncomms3950.
- [17] M. S. Branham, W.-C. Hsu, S. Yerci, J. Loomis, S. V. Boriskina, B. R. Hoard, S. E. Han, and G. Chen, "15.7% efficient 10- μ m-thick crystalline silicon solar cells using periodic nanostructures," 2015. DOI: 10.1002/adma.201405511.
- [18] J. H. Petermann, D. Zielke, J. Schmidt, F. Haase, E. G. Rojas, and R. Brendel, "19%-efficient and 43 μ m-thick crystalline si solar cell from layer transfer using porous silicon," *Progress in Photovoltaics: Research and Applications*, 2011. DOI: 10.1002/pip.1129.
- [19] I. Massiot, A. Cattoni, and S. Collin, "Progress and prospects for ultrathin solar cells," *Nature Energy*, 2020. DOI: 10.1038/s41560-020-00714-4.
- [20] A. Bozzola, M. Liscidini, and L. C. Andreani, "Broadband light trapping with disordered photonic structures in thin-film silicon solar cells," *Progress in Photovoltaics: Research and Applications*, 2013. DOI: 10.1002/pip.2385.
- [21] A. Chremos, "Design of nearly perfect hyperuniform polymeric materials," *The Journal of Chemical Physics*, 2020. DOI: 10.1063/5.0017861.
- [22] M. Kelly, "In the eye of a chicken, a new state of matter comes into view," *Princeton University News*, 2014. [Online]. Available: <https://www.princeton.edu/news/2014/02/24/eye-chicken-new-state-matter-comes-view> (visited on 07/21/2021).
- [23] S. Torquato and F. H. Stillinger, "Local density fluctuations, hyperuniformity, and order metrics," *Phys. Rev. E*, 2003. DOI: 10.1103/physreve.68.041113.
- [24] C. E. Zachary and S. Torquato, "Hyperuniformity in point patterns and two-phase random heterogeneous media," *Journal of Statistical Mechanics: Theory and Experiment*, 2009. DOI: 10.1088/1742-5468/2009/12/p12015.
- [25] G. Zhang and S. Torquato, "Realizable hyperuniform and nonhyperuniform particle configurations with targeted spectral functions via effective pair interactions," *Phys. Rev. E*, 2020. DOI: 10.1103/PhysRevE.101.032124.
- [26] Y. Jiao, T. Lau, H. Hatzikirou, M. Meyer-Hermann, J. C. Corbo, and S. Torquato, "Avian photoreceptor patterns represent a disordered hyperuniform solution to a multiscale packing problem," *Physical Review E*, 2014. DOI: 10.1103/physreve.89.022721.

- [27] A. Gabrielli, M. Joyce, and F. S. Labini, "Glass-like universe: Real-space correlation properties of standard cosmological models," *Phys. Rev. D*, 2002. DOI: 10.1103/physrevd.65.083523.
- [28] C. E. Zachary, Y. Jiao, and S. Torquato, "Hyperuniform long-range correlations are a signature of disordered jammed hard-particle packings," *Phys. Rev. Lett.*, 2011. DOI: 10.1103/physrevlett.106.178001.
- [29] A. Mayer, V. Balasubramanian, T. Mora, and A. M. Walczak, "How a well-adapted immune system is organized," *PNAS*, 2015. DOI: 10.1073/pnas.1421827112.
- [30] M. A. Klatt, J. Lovrić, D. Chen, S. C. Kapfer, F. M. Schaller, P. W. A. Schönhöfer, B. S. Gardiner, A.-S. Smith, G. E. Schröder-Turk, and S. Torquato, "Universal hidden order in amorphous cellular geometries," *Nature Communications*, 2019. DOI: 10.1038/s41467-019-08360-5.
- [31] R. D. Batten, F. H. Stillinger, and S. Torquato, "Classical disordered ground states: Super-ideal gases and stealth and equi-luminous materials," *Journal of Applied Physics*, 2008. DOI: 10.1063/1.2961314.
- [32] M. Florescu, S. Torquato, and P. J. Steinhardt, "Designer disordered materials with large, complete photonic band gaps," *PNAS*, 2009. DOI: 10.1073/pnas.0907744106.
- [33] S. Gorsky, W. A. Britton, Y. Chen, J. Montaner, A. Lenef, M. Raukas, and L. D. Negro, "Engineered hyperuniformity for directional light extraction," *APL Photonics*, 2019. DOI: 10.1063/1.5124302.
- [34] H. Zhang, H. Chu, H. Giddens, W. Wu, and Y. Hao, "Experimental demonstration of luneburg lens based on hyperuniform disordered media," *Applied Physics Letters*, 2019. DOI: 10.1063/1.5055295.
- [35] N. Tavakoli, R. Spalding, P. Koppejan, G. Gkantounis, C. Wang, R. Röhrich, E. Kontoleta, A. F. Koenderink, R. Sapienza, M. Florescu, and E. Alarcon-Llado, "Over 65 % sunlight absorption in a 1 μm si slab with hyperuniform texture," *Research Square*, 2020. DOI: 10.21203/rs.3.rs-69198/v1.
- [36] S. Johnson and J. Joannopoulos, "Block-iterative frequency-domain methods for maxwell's equations in a planewave basis," *Optics Express*, 2001. DOI: 10.1364/oe.8.000173.
- [37] D. T. Lee and B. J. Schachter, "Two algorithms for constructing a delaunay triangulation," *International Journal of Computer & Information Sciences*, 1980. DOI: 10.1007/bf00977785.
- [38] M. M. Milošević, W. Man, G. Nahal, P. J. Steinhardt, S. Torquato, P. M. Chaikin, T. Amoah, B. Yu, R. A. Mullen, and M. Florescu, "Hyperuniform disordered waveguides and devices for near infrared silicon photonics," *Scientific Reports*, 2019. DOI: 10.1038/s41598-019-56692-5.
- [39] J. W. Cahn, "On spinodal decomposition," *Acta Metallurgica*, 1961. DOI: 10.1016/0001-6160(61)90182-1.
- [40] J. W. Cahn, "Phase separation by spinodal decomposition in isotropic systems," *The Journal of Chemical Physics*, 1965. DOI: 10.1063/1.1695731.
- [41] Z. Ma and S. Torquato, "Random scalar fields and hyperuniformity," *Journal of Applied Physics*, 2017. DOI: 10.1063/1.4989492.

- [42] D. M. Florescu, *Theoretical nanophotonics and quantum optics group*, 2021. [Online]. Available: <http://personal.ph.surrey.ac.uk/~mf0014/research.html> (visited on 07/19/2021).
- [43] nrel.gov, *Am1.5 solar spectrum irradiance data*. [Online]. Available: <https://www.nrel.gov/grid/solar-resource/spectra.html> (visited on 06/30/2021).
- [44] Z. Fan, Q. Lin, S.-F. Leung, and Q. Zheng, "Roll-to-roll fabrication of flexible thin film solar cells on low cost three-dimensional nano-textured substrates," *ECS Meeting Abstracts*, 2013. DOI: 10.1149/ma2013-02/26/1965.
- [45] W. Soppe, H Borg, B. Van Aken, C Devilee, M Dörenkämper, M. Goris, M. Heijna, J Löffler, and P Peeters, "Roll to roll fabrication of thin film silicon solar cells on nano-textured substrates," *Journal of nanoscience and nanotechnology*, 2011. DOI: 10.1109/INEC.2010.5424681.
- [46] S. H. Ahn and L. J. Guo, "Large-area roll-to-roll and roll-to-plate nanoimprint lithography: A step toward high-throughput application of continuous nanoimprinting," *ACS Nano*, 2009. DOI: 10.1021/nn9003633.
- [47] T. Fließbach, *Elektrodynamik. Lehrbuch zur Theoretischen Physik II*, German, 6th ed. Heidelberg: Springer Spektrum, 2012, ISBN: 978-3-8274-3035-9/hbk; 978-3-8274-3036-6/ebook.
- [48] E. Hecht, *Optik*, 7th ed., K. Lippert, Ed. De Gruyter, 2018, ISBN: 9783110526646.
- [49] G. T. Reed and A. P. Knights, *Silicon Photonics*. Wiley & Sons, 2004. DOI: 10.1002/0470014180.
- [50] A. Ghatak, K. Thyagarajan, and M. Shenoy, "Numerical analysis of planar optical waveguides using matrix approach," *Journal of Lightwave Technology*, 1987. DOI: 10.1109/jlt.1987.1075553.
- [51] Beer, "Bestimmung der absorption des rothen lichts in farbigen flüssigkeiten," *Ann. d. Phys.*, 1852. DOI: 10.1002/andp.18521620505.
- [52] A. Naqavi, F.-J. Haug, C. Battaglia, H. P. Herzig, and C. Ballif, "Light trapping in solar cells at the extreme coupling limit," *Journal of the Optical Society of America B*, 2012. DOI: 10.1364/JOSAB.30.000013.
- [53] D. Redfield, "Multiple-pass thin-film silicon solar cell," *Applied Physics Letters*, 1974. DOI: 10.1063/1.1655344.
- [54] J. G. Mutitu, S. Shi, C. Chen, T. Creazzo, A. Barnett, C. Honsberg, and D. W. Prather, "Thin film solar cell design based on photonic crystal and diffractive grating structures," *Optics Express*, 2008. DOI: 10.1364/oe.16.015238.
- [55] S. Fan and J. D. Joannopoulos, "Analysis of guided resonances in photonic crystal slabs," *Phys. Rev. B*, 2002. DOI: 10.1103/physrevb.65.235112.
- [56] H. Haus, *Waves and fields in optoelectronics*. Prentice-Hall, 1984, ISBN: 9780139460531.
- [57] Z. Yu, A. Raman, and S. Fan, "Fundamental limit of nanophotonic light-trapping in solar cells," *PNAS*, 2010. DOI: 10.1073/pnas.1008296107.
- [58] X. Sheng, S. G. Johnson, J. Michel, and L. C. Kimerling, "Optimization-based design of surface textures for thin-film si solar cells," *Optics express*, 2011. DOI: 10.1364/OE.19.00A841.
- [59] P. Wang and R. Menon, "Simulation and analysis of the angular response of 1d dielectric nanophotonic light-trapping structures in thin-film photovoltaics," *Optics Express*, 2012. DOI: 10.1364/OE.20.00A545.

- [60] J. Buencuerpo, L. E. Munioz-Camuniez, M. L. Dotor, and P. A. Postigo, "Optical absorption enhancement in a hybrid system photonic crystal – thin substrate for photovoltaic applications," *Optics Express*, 2012. DOI: 10.1364/oe.20.00a452.
- [61] P. W. Anderson, "Absence of diffusion in certain random lattices," *Phys. Rev.*, 1958. DOI: 10.1103/PhysRev.109.1492.
- [62] C. Kittel, *Introduction to Solid State Physics*. WILEY, 2004, ISBN: 047141526X.
- [63] M. A. Green, "Lambertian light trapping in textured solar cells and light-emitting diodes: Analytical solutions," *progress in Photovoltaics: Research and Applications*, 2002. DOI: doi.org/10.1002/pip.404.
- [64] Prof. Dr. Femius Koenderink, *Personal correspondence*, 2021. [Online]. Available: <https://amolf.nl/people/femius-koenderink> (visited on 08/07/2021).
- [65] Lumerical, Inc., *Lumerical FDTD and FEEM*, Version: 2021-R1.2-2621-dc09d2e-imp-2019.8.254, 2021. [Online]. Available: <https://www.lumerical.com/products/> (visited on 07/07/2021).
- [66] M. A. Green, "Self-consistent optical parameters of intrinsic silicon at 300k including temperature coefficients," *Solar Energy Materials and Solar Cells*, 2008. DOI: 10.1016/j.solmat.2008.06.009.
- [67] M. Polyanskiy, *Database for material constants*, refractiveindex.info, 2021. [Online]. Available: <http://refractiveindex.info> (visited on 07/07/2021).
- [68] A. Lambertz, *Modesolver and absorption python script*, [github.com](https://github.com/shibmaster/modesolver-absorption), 2021. [Online]. Available: <https://github.com/shibmaster/modesolver-absorption> (visited on 08/17/2021).
- [69] A. Lambertz, *Modesolver and absorption python script readme*, 2021. [Online]. Available: <https://shibmaster.github.io/modesolver-absorption/> (visited on 08/17/2021).
- [70] [surf.nl](https://www.surf.nl/en/dutch-national-supercomputer-cartesius), *Dutch supercomputer cartesius website*. [Online]. Available: <https://www.surf.nl/en/dutch-national-supercomputer-cartesius> (visited on 07/27/2021).
- [71] E. Yablonovitch, "Statistical ray optics," *J. Opt. Soc. Am.*, 1982. DOI: 10.1364/JOSA.72.000899.
- [72] S. Collin and M. Giteau, "New limits for light-trapping with multi-resonant absorption," *IEEE 7th World Conference on Photovoltaic Energy Conversion (WCPEC) (A Joint Conference of 45th IEEE PVSC, 28th PVSEC & 34th EU PVSEC)*, 2018. DOI: 10.1109/pvsc.2018.8547477.
- [73] K. X. Wang, Y. Guo, and S. Fan, "Wave optics light-trapping theory: Mathematical justification and ultimate limit on enhancement," *Journal of the Optical Society of America B*, 2019. DOI: 10.1364/josab.36.002414.
- [74] R. Paschotta, *Article on free spectral range*, 2021. [Online]. Available: https://www.rp-photonics.com/free_spectral_range.html (visited on 08/07/2021).
- [75] M. Verschuuren, *Substrate conformal imprint lithography for nanophotonics*. Utrecht University, 2010, ISBN: 9789074445931.
- [76] M. A. Verschuuren, M. Megens, Y. Ni, H. van Sprang, and A. Polman, "Large area nanoimprint by substrate conformal imprint lithography (SCIL)," *Advanced Optical Technologies*, 2017. DOI: 10.1515/aot-2017-0022.
- [77] J. Thirumalai, Ed., *Micro/Nanolithography*. IntechOpen, 2018, ISBN: 1789230306.

- [78] U. Aljancic, D. Resnik, D. Vrtacnik, M. Mozek, and S. Amon, "Silicon-glass anodic bonding.," *Inf. Midem-J. Microelectron. Electron. Compon. Mater.*, 2004.
- [79] A. C. Lapadatu and H. Jakobsen, "Anodic bonding," in *Handbook of Silicon Based MEMS Materials and Technologies*, Elsevier, 2015. DOI: 10.1016/b978-0-323-29965-7.00030-0.
- [80] W. H. Teh, A. Trigg, C. H. Tung, R. Kumar, N. Balasubramanian, and D. L. Kwong, "200 mm wafer-scale epitaxial transfer of single crystal si on glass by anodic bonding of silicon-on-insulator wafers," *Applied Physics Letters*, 2005. DOI: 10.1063/1.2011772.
- [81] J. A. Plaza, E. González, J. Esteve1, M. M. Visser, D. T. Wang, and A. Hanneborg, "Cathodic debond of anodically bonded silicon to glass wafers," *Electrochemical and Solid-State Letters*, 1999. DOI: 10.1149/1.1391157.
- [82] P. Ramm, *Handbook of Wafer Bonding*, J. J.-Q. Lu and M. M. Taklo, Eds. John Wiley & Sons, 2012, ISBN: 3527326464.
- [83] C. H. Lee, J.-H. Kim, C. Zou, I. S. Cho, J. M. Weisse, W. Nemeth, Q. Wang, A. C. T. van Duin, T.-S. Kim, and X. Zheng, "Peel-and-stick: Mechanism study for efficient fabrication of flexible/transparent thin-film electronics," *Scientific Reports*, 2013. DOI: 10.1038/srep02917.
- [84] C. Wang, H. Fang, S. Zhou, X. Qi, F. Niu, W. Zhang, Y. Tian, and T. Suga, "Recycled low-temperature direct bonding of si/glass and glass/glass chips for detachable micro/nanofluidic devices," *Journal of Materials Science & Technology*, 2020. DOI: 10.1016/j.jmst.2019.11.034.
- [85] N. Palavesam, C. Landesberger, and K. Bock, "Investigations of the fracture strength of thin silicon dies embedded in flexible foil substrates," in *2014 IEEE 20th International Symposium for Design and Technology in Electronic Packaging (SIITME)*, IEEE, 2014. DOI: 10.1109/siitme.2014.6967042.
- [86] A. Plößl, "Wafer direct bonding: Tailoring adhesion between brittle materials," *Materials Science and Engineering: R: Reports*, 1999. DOI: 10.1016/s0927-796x(98)00017-5.
- [87] R. Puligadda, S. Pillalamarri, W. Hong, C. Brubaker, M. Wimplinger, and S. Pargfrieder, "High-performance temporary adhesives for wafer bonding applications," *MRS Online Proceedings Library*, 2006. DOI: 10.1557/proc-0970-y04-09.
- [88] AMOLF, *Photonic materials group*. [Online]. Available: <https://amolf.nl/research-groups/photonic-materials> (visited on 08/04/2021).
- [89] bison.nl, *Epoxy glue 2-component datasheet*. [Online]. Available: <https://www.bison.nl/content/dam/boltonadhesives/products/import/48/nl/6305950/50.pdf> (visited on 08/04/2021).
- [90] F. Awaja, S. Zhang, N. James, and D. R. McKenzie, "Plasma activation and self bonding of PEEK for the use in the encapsulation of medical implants," *Plasma Processes and Polymers*, 2010. DOI: 10.1002/ppap.201000018.
- [91] S. Franssila, *Introduction to Microfabrication*. WILEY, 2010, ISBN: 9780470749838.
- [92] E. Tocce, S. Liliensiek, M. Wilson, B. Yanez-Soto, P. Nealey, and C. Murphy, "Engineering the biophysical properties of basement membranes into biomaterials: Fabrication and effects on cell behavior," in *Comprehensive Biomaterials*, Elsevier, 2011. DOI: 10.1016/b978-0-08-055294-1.00053-2.

- [93] Allresist GmbH, *E-beam-resist-ar-p-6200 datasheet*. [Online]. Available: <https://www.allresist.com/portfolio-item/e-beam-resist-ar-p-6200-series-csar-62/> (visited on 08/04/2021).
- [94] Microchemicals GmbH, *Substrate preparation (for imprint resist)*. [Online]. Available: https://www.microchemicals.com/technical_information/substrate_cleaning_adhesion_photoresist.pdf (visited on 08/04/2021).
- [95] Allresist GmbH, *Protective coating ar-pc 5091.02 (electra 92)*, online. [Online]. Available: <https://www.allresist.com/portfolio-item/protective-coating-ar-pc-5091-02-electra-92/> (visited on 08/04/2021).
- [96] AMOLF NanoLab, *Low-pressure oxygen-plasma-system pico*. [Online]. Available: <https://amolf.nl/low-pressure-oxygen-plasma-system-pico> (visited on 08/04/2021).
- [97] AMOLF NanoLab, *FEI Helios Nanolab 600 (Scanning Electron Microscope)*. [Online]. Available: <https://amolf.nl/low-pressure-oxygen-plasma-system-pico> (visited on 08/04/2021).
- [98] ThermoFischer, *Sem system: Helios nanolab 600i datasheet*. [Online]. Available: <https://www.fei.com/documents/helios-nanolab-600i-datasheet/#gsc.tab=0> (visited on 08/04/2021).
- [99] A. Nanakoudis, "Scanning electron microscopy explained," *ThermoFischer Scientific*, 2019. [Online]. Available: <https://www.thermofisher.com/blog/microscopy/what-is-sem-scanning-electron-microscopy-explained/> (visited on 08/04/2021).
- [100] W. Rasband, *ImageJ Documentation, Online Wiki*, U.S. National Institutes of Health. [Online]. Available: https://imagejdocu.tudor.lu/faq/general/what_is_imagej (visited on 08/04/2021).
- [101] P. Baggethun, *Radial-profile extraction ImageJ plugin*, 2009. [Online]. Available: <https://imagej.nih.gov/ij/plugins/radial-profile.html> (visited on 08/04/2021).
- [102] D. Lamers, "Fabrication recipe for scil stamp," *AMOLF NanoLab, Amsterdam*, 2016. [Online]. Available: https://wiki.amolf.nl/NC/index.php/SCIL_stamp_fabrication_recipe (visited on 08/04/2021).
- [103] DOWSIL, *Dow corning primer datasheet*, 2017. [Online]. Available: <https://www.buildsite.com/pdf/dowcorning/DOWSIL-Primer-C-Product-Data-1799975.pdf> (visited on 08/04/2021).
- [104] Engineering ToolBox, *Coefficients of linear thermal expansion*, 2003. [Online]. Available: https://www.engineeringtoolbox.com/linear-expansion-coefficients-d_95.html (visited on 08/04/2021).
- [105] AMOLF NanoLab, *Oxford plasmapro100 cobra, reactive ion etcher*, 2021. [Online]. Available: <https://amolf.nl/oxford-plasmapro100-cobra> (visited on 08/04/2021).
- [106] OXFORD, *Oxford plasmapro100 cobra, reactive ion etcher*, 2021. [Online]. Available: <https://plasma.oxinst.com/products/icp-etching/plasmapro-100-cobra-icp> (visited on 08/04/2021).
- [107] NanolabNL, *AMOLF NanoLab web-presence on nanolabnl.nl*. [Online]. Available: <https://nanolabnl.nl/locations-contact/amsterdam/> (visited on 08/04/2021).

Appendix A

Mode solver and absorption with HUD-patterns

The following sections hold additional calculations and serve to give detailed instructions for replicating mode data and absorption figures of the main text (Appendix A), bond an ultra-thin substrate to a carrier using the specially made spin coating mounts and an adhesive (Appendix B), as well as obtaining the structure factor and filling fraction from SEM images (Appendix C).

Deriving the wave equation

This section includes the detailed steps to sec. 2.1.1 for obtaining the wave equation in simple media. The propagation of electromagnetic waves in vacuum and matter is described by Maxwell's equations. In the absence of free charge- ($\phi = 0$) and current- ($\vec{j} = 0$) densities, they can be simplified to eq. (A.1-A.4)[47]:

$$\vec{\nabla} \cdot \vec{E} = 0, \quad (\text{A.1})$$

$$\vec{\nabla} \cdot \vec{B} = 0, \quad (\text{A.2})$$

$$\vec{\nabla} \times \vec{E} = -\frac{\partial}{\partial t} \vec{B}, \quad (\text{A.3})$$

$$\vec{\nabla} \times \vec{B} = \frac{\partial}{\partial t} \vec{E}, \quad (\text{A.4})$$

where \vec{E} , \vec{B} denote the electric field and magnetic flux density, respectively, and c the speed of light in vacuum [47]. From eq. (A.3) and (A.4), the differential form of the wave-equation for electric and magnetic waves can be found as follows. In case of the electric field, one proceeds by taking the curl of eq. (A.3), applying Fubini's theorem, and subsequently replacing $\vec{\nabla} \times \vec{B}$ with eq. (A.4) to obtain:

$$\begin{aligned} \vec{\nabla} \times \vec{\nabla} \times \vec{E} &= -\vec{\nabla} \times \frac{\partial}{\partial t} \vec{B} = -\frac{\partial}{\partial t} \vec{\nabla} \times \vec{B}, \\ &\rightarrow \vec{\nabla} \left(\vec{\nabla} \cdot \vec{E} \right) - \nabla^2 \vec{E} = -\frac{\partial}{\partial t} \frac{\partial}{\partial t} \vec{E} \\ &\rightarrow \nabla^2 \vec{E} = \frac{\partial^2}{\partial t^2} \vec{E}, \end{aligned} \quad (\text{A.5})$$

where the vector identity $\vec{\nabla} \times \vec{\nabla} \times = \vec{\nabla} \left(\vec{\nabla} \cdot \right) - \nabla^2$ and $\vec{\nabla} \cdot \vec{E} = 0$ was used. Equivalently, one may obtain the wave equation for the magnetic induction by taking the

curl of eq. (A.4) and inserting it into eq. (A.3) to find:

$$\rightarrow \nabla^2 \vec{B} = \frac{\partial^2}{c^2 \partial t^2} \vec{B}. \quad (\text{A.6})$$

The simplest form of a solution for eq. (A.5) is given by the plane-wave equation below:

$$\vec{E}(\vec{x}, t) = \vec{E}_0 \exp [i (k_0 \vec{x} - \omega t)], \quad (\text{A.7})$$

where the free-space wavevector k_0 and frequency ω are defined by $c = \frac{\omega}{k_0} = \sqrt{\frac{1}{\epsilon_0 \mu_0}}$, with vacuum permittivity ϵ_0 , and vacuum permeability μ_0 .

Inside of a medium, eq. (A.4) takes on a different form in order to include the response of the material (i.e. polarization, magnetization, induced currents) to the propagation of electromagnetic waves:

$$\vec{\nabla} \times \vec{H} = \frac{\partial}{c \partial t} \vec{D}, \quad (\text{A.8})$$

where the relation between the magnetic field \vec{H} and magnetic flux density \vec{B} , and the relation between the electric field \vec{E} and the electric flux density \vec{D} , for a lossless, linear, homogeneous, and isotropic medium are given by:

$$\vec{D} = \epsilon_r \vec{E}, \quad (\text{A.9})$$

$$\vec{B} = \mu_r \vec{H}. \quad (\text{A.10})$$

Here, $\epsilon_r = \frac{\epsilon}{\epsilon_0}$ and $\mu_r = \frac{\mu}{\mu_0}$ denote the relative permittivity and permeability of the medium, respectively. Repeating the operations for obtaining the wave-equation as outlined above, starting now from eq. (A.8) and re-substituting \vec{H} and \vec{D} with eq. (A.9) and (A.10), respectively, equation (A.5) becomes:

$$\nabla^2 \vec{E} = \frac{\epsilon_r \mu_r}{c^2} \frac{\partial^2}{\partial t^2} \vec{E}, \quad (\text{A.11})$$

where the fraction $\frac{\epsilon_r \mu_r}{c^2}$ denotes the inverse square of the phase velocity v^{-2} of the wave in the medium, which may equivalently be expressed with the refractive index $n = \sqrt{\epsilon_r \mu_r} = \frac{c}{v}$ [48]. The plane-wave solution for eq. (A.11) takes on the form:

$$\vec{E}(\vec{x}, t) = \vec{E}_0 \exp [i (\vec{k} \vec{x} - \omega t)], \quad (\text{A.12})$$

where now the wavevector $\vec{k} = n \cdot \vec{k}_0$. Inserting eq. (A.12) into eq. (A.11) yields the dispersion relation:

$$|\vec{k}|^2 = \frac{\omega^2}{v^2} = \frac{n^2 \omega^2}{c^2}. \quad (\text{A.13})$$

The wavevector $k = \frac{2\pi n}{\lambda}$ indicates the phase-change of the wave with respect to distance in the medium, similar to ω representing the temporal change of phase.

Verifying boundary conditions through Maxwell's equations

The eigenvalue equation (2.18) in the main text was obtained through ray-optical consideration. The form of this equation can be validated through solving the wave equation (A.11) for the case of the waveguide and stipulate boundary conditions, namely continuity of fields and their first derivatives across the interface. For the electric field of a wave travelling in the positive z -direction and polarized only in the x -direction $\vec{E} = E_0 \cdot \hat{e}_x \equiv E_x$, eq. (A.12) of the plane wave simplifies to:

$$\vec{E}(\vec{x}, t) = E_x(y, z, t) = E_x e^{-ik_y y} e^{-ik_z z} e^{i\omega t}, \quad (\text{A.14})$$

where $\vec{E}(x) = \text{const}$, since the waveguide is assumed infinite in x .

When inserted into the wave equation (A.11), the left-hand side becomes:

$$\nabla^2 E_x = \partial_y^2 E_x + \partial_z^2 E_x = -\left(k_y^2 + k_z^2\right) E_x, \quad (\text{A.15})$$

and the right-hand side:

$$\frac{n^2}{c^2} \partial_t^2 E_x = -\frac{n^2}{c^2} \omega^2 E_x, \quad (\text{A.16})$$

from which and also fig. 2.1b) follows:

$$\left(\frac{n^2 \omega^2}{c^2} - k_z^2\right) E_x = (k_0 n^2 - \beta^2) E_x = k_y^2 E_x. \quad (\text{A.17})$$

The expression $(k_0 n^2 - \beta^2)$ is greater or equal zero inside the waveguide core, but since $n \approx 1$ in air and $\beta > \frac{\omega}{c}$ for total internal reflection, k_y^2 must be negative and hence k_y imaginary outside the core. The plane-wave solutions for the latter case can be written as:

$$y \geq \frac{h}{2} \rightarrow E_u(y, z, t) = e^{-k_{yu}(y - \frac{h}{2})} E_x(z, t), \quad (\text{A.18})$$

$$y \leq -\frac{h}{2} \rightarrow E_l(y, z, t) = e^{k_{yl}(y + \frac{h}{2})} E_x(z, t), \quad (\text{A.19})$$

where k_{yu} and k_{yl} are now real constants for the upper and lower air half-spaces, respectively. In the core:

$$|y| \leq \frac{h}{2} \rightarrow E_c(y, z, t) = e^{-ik_y y} E_x(z, t). \quad (\text{A.20})$$

In order to simplify solving the boundary conditions at the interfaces we will deviate from the generalized expressions and only describe the plane-wave for even modes by a cosine function, though an equivalent procedure can be performed with the odd modes featuring sine.

At the upper interface $y = h/2$, from

$$E_u = E_c \cos\left(k_y \frac{h}{2} + \phi\right) \quad (\text{A.21})$$

and from the first derivative:

$$k_{yu} E_u = k_y E_c \sin\left(k_y \frac{h}{2} + \phi\right), \quad (\text{A.22})$$

follows through elimination of E_u :

$$\tan\left(k_y \frac{h}{2} + \phi\right) = \frac{k_{yu}}{k_y}. \quad (\text{A.23})$$

Similarly, at the lower interface $y = -h/2$:

$$E_l = E_c \cos\left(-k_y \frac{h}{2} + \phi\right) \quad (\text{A.24})$$

and the first derivative:

$$k_{yl}E_l = k_y E_c \sin\left(k_y \frac{h}{2} - \phi\right), \quad (\text{A.25})$$

which leads to:

$$\tan\left(-k_y \frac{h}{2} + \phi\right) = \frac{k_{yl}}{k_y}. \quad (\text{A.26})$$

Now taking the arctan from eq. (A.23) and (A.26) and subsequently adding both, the resulting equation is:

$$k_y h + m\pi = \tan^{-1}\left(\frac{k_{yu}}{k_y}\right) + \tan^{-1}\left(\frac{k_{yl}}{k_y}\right), \quad (\text{A.27})$$

which is equivalent to eq. (2.18) divided by two, since $k_y h = \phi_t = k_0 n \cos(\theta) \cdot h$ and

$$\tan^{-1} \frac{k_{yu}}{k_y} = \tan^{-1} \frac{k_{yl}}{k_y} = \Phi_{TE}/2 = \tan^{-1} \frac{\sqrt{n_1^2 k_0^2 \sin^2(\theta) - n_2^2 k_0^2}}{k_0 n_1 \cos(\theta)} = \tan^{-1} \frac{\sqrt{\sin^2(\theta) - \left(\frac{n_1}{n_2}\right)^2}}{\cos(\theta)}.$$

Modesolver and Slab-Absorption

The python module for calculating the 1D mode data for a three-layered stack can be freely downloaded from github, along with the module that calculates the estimated absorption based on the mode data for stealthy hyperuniform point patterns.

The material constants, i.e. n, k values, of the three layers in the stack need to be provided in tabulated values for n and k individually, where the wavelength in microns composes the first column and the numerical value of n or k composes the second. This data can be easily obtained for example from refractiveindex.info, values for quartz, nitrogen, silicon, and silver from this collection of sources are already provided with the module.

Also provided is a jupyter notebook, which takes the user through every step from creating a layered stack, calculating the propagation constants as well as the estimated absorption for a variety of parameters, to plotting the results and exporting data into useful tables. Below, the relevant sections of the notebook are printed as figures, thus enabling the reader to use individually the provided modules and have the jupyter instructions as a reference manual.

The mode solver library

Let's import the library which only has the Modedata class: (Enter the Code-containing field by marking it and pressing "ENTER" and then compile by pressing "CTRL"+"ENTER")

```
python3-code
```

```
from MSclass13 import *
```

Use of tabulated data for refractive index values

The library is capable of importing the refractive index from any source, e.g. refractiveindex.info, if the data is provided in two separate text files for real and imaginary part, where the filename consists of the material and the suffix "R" or "I" for real- and imaginary, respectively. The files should each contain two columns with wavelength in microns and the respective value in column 1 and 2, respectively. If the filename cannot be found, generic values for air will be used (real=1, imaginary=0).

Example: Si: Two files: siliconR.dat and siliconI.dat.

Content: siliconR.dat

[lambda] [n] (The first row will be skipped)

0.255 10.4

0.256 10.7

... ..

Let's Create a Mode data object

python3-code

```
# Provide the wavelength bounds in microns:
# Lambda min, Lambda max, Lambda step
LambdaBounds=[0.4,1.2,.005]

# Provide the materials of upper clad, core,
# lower clad, respectively.
Layers=["air","silicon","air"]

# Provide the thickness of the waveguide in microns
Thickness=1.0

# Provide the number of significant digits to solve.
Precision=5

# Create a Modedata object m
m=Modedata(LambdaBounds,Layers,Thickness,Precision)

# Print the current status of the object
print(m)

# Generate the modedata now
m.generate()

# Export mode data to txt file "name.dat"
m.Export('name')

# Plot the dispersion diagram to a file 'disp.pdf'
m.plDisp('disp')
```

List all available functions

python3-code

```
# Print README of possible options for the object
m.help()

# Print all available sub-functions, their purpose & use
m.Fhelp()

# Print all available plot functions, their purpose & use
m.Phelp()
```


The coupled-mode theory library

Import the library for CMT calculations:

```
python3-code
```

```
from CMT01 import *
```

Import mode data from file

```
python3-code
```

```
importModes('name.dat')
```

Here, the file extension needs to be provided.

Calculate integrated absorption

There are two equations available to calculate (2.33), denoted eq7a, and eq7b, which are provided to the functions for integrated absorption, absorption spectrum, or k_1 vs. k_2 plots.

eq7a corresponds to (2.33) with (2.31), and

eq7b corresponds to (2.33) with (2.36).

Also, the path length enhancement $f_p = 1$ or $f_p = 4$ can be chosen, denoted with eq8a or eq8b, respectively. The nomenclature of the equations stems from the shortened derivation found in the full notebook available on github [68].

IA for $k_1 = 10, k_2 = 20$, via (2.33) with (2.31) and $f_p = 4$:

```
python3-code
```

```
print(IA(10, 20, eq7a, eq8b))
```

Plot absorption or absorbed fraction of the AM1.5 irradiance

In order to plot the absorption spectrum for $k_1 = 10, k_2 = 20$, via (2.33) with (2.31) and $f_p = 4$, and save it to a pdf with name "AbsVsLambda.pdf":

```
python3-code
```

```
plAbsorption(10, 20, eq7a, eq8b, name='AbsVsLambda')
```

If one wants to plot the AM1.5 spectrum and absorbed fraction thereof for $k_1 = 15, k_2 = 60$, via (2.33) with (2.36) and $f_p = 4$, and save it to a pdf with name "Am15spectrum.pdf":

python3-code

```
plSpectrum(10,20,eq7b,eq8b,name='Am15spectrum')
```

Plot heat map for absorbance against k_1 and k_2

Plot a heat map for all k_1, k_2 combinations in the range $k_{\min} = 5$ to $k_{\max} = 40$ with 0.5 increments, via (2.33) with (2.31) and $f_p = 1$, and save it to a pdf with name "heatmap.pdf":

python3-code

```
plk1k2(5,40,eq7a,eq8a,delta=0.5, name='heatmap')
```

The standard delta between k -values equals one, and depending on the chosen parameters, this generation can take a very long time.

This concludes the minimal execution of the libraries, much more elaborate explanations and additional functions are found in the notebook "Modesolver and Slab Absorption.ipynb".

Appendix B

Step-by-Step from Bonding to Patterned Devices

The following shall serve as step-wise instructions for obtaining HUD structures on fragile substrates using SCIL.

Depending on the choice of the substrate, the procedure may differ slightly between IBC cells and 10 μm -thick membranes.

Bonding

Attention: Prepare everything for the bonding procedure before opening the membrane's case, so that it stays protected and cannot be accidentally be picked up by the draft in the fumehood.

Choose a mount. For 10 μm thickness, the PEEK mount with a spacer is recommended. The same without a spacer is recommended with IBC cells. For thicker substrates, one would use the aluminum mount without spacer. Fig. B.1 shows a spacer cut from lens paper situated on the PEEK mount with a piece of (transparent) mylar for vacuum seal testing.

Find out the spin parameters for the adhesive, in this case PMMA 950 A9, 3 months old, undiluted. Spin coat a layer on cover-glass, scratch it and measure the depth. 350 nm to 400 nm thickness works well with membranes. Twice as much thickness (700-1000) nm is recommended for the IBC solar cells. Once the spin-parameters are known (around 2000 RPM with 1000 RPM/s acceleration, closed bowl, 45 s, yielded 385 nm for the above PMMA.), proceed with the special spin-coating mount.

Place the mount onto the spin-coater, optionally align the spacer with on the mount's center protrusion. Turn on the vacuum pump, but do not open the valve to the mount yet.

Run an oxygen plasma "descum" for two minutes on the carrier to activate its surface. Afterwards, place the carrier on a hotplate at 90°C until needed. Open the membrane case and lift the membrane with soft plastic tweezers that have a spatula on one end. Place the substrate centered on the protrusion (spacer), such that its rim extends beyond the protrusion around the circumference, then open the vacuum valve and check for deformations. If deformations occur and no spacer was used, it may be necessary to polish the (PEEK) mount again. If the spacer seems to be the cause, try exchanging it for another.

If no/little deformations are visible (cp. with fig. B.2), proceed to spin-coat the PMMA according to the deduced parameters for the desired thickness. Shortly before starting the program, take the carrier from the hotplate to cool it down a little before bonding. Immediately when the spin-coater lid opens, be ready to place the carrier onto the membrane. Do so carefully and without applied force initially, but



FIGURE B.1: PEEK mount with lens paper spacer cut to the outer diameter of the mount's center protrusion. On top of the spacer sits a piece of $\approx 20\text{ }\mu\text{m}$ -thick mylar and the vacuum pump is turned on.

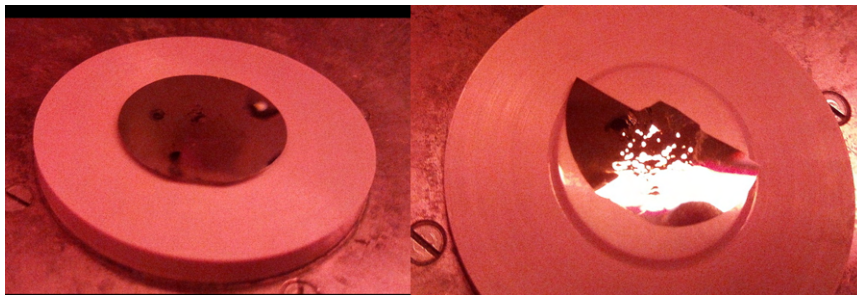


FIGURE B.2: Left: Membrane on Spin-coater mount after turning on vacuum. A flat surface is visible. Right: Deformations of a membrane when using special mount with insufficiently polished surface.

let the carrier settle by its own weight. If a transparent carrier is used, the bond quality can immediately be assessed by eye and if voids are visible, repeatedly apply light pressure to above the center of the membrane (fig. B.3), but try not to move the carrier too much in the direction parallel to the interface. If a spacer was used, the carrier with membrane attached can be lifted off of the mount immediately, flipped and placed onto a hotplate for baking at $120\text{ }^{\circ}\text{C}$ for 180 s.

Without a spacer and the PEEK mount, instead of placing the carrier onto the mount, take the mount including membrane and flip it over, then carefully place it centered onto the carrier. The direct-bonding forces between the membrane and PEEK will keep it from falling off for some time. Apply light pressure to the center of the backside of the mount to make contact between the carrier and the substrate. Now use an N_2 -gun and align its nozzle with the center hole on the backside of the mount (fig. B.4). Slowly depress the trigger to build up a little over-pressure, almost immediately the mount should slide free from the air-cushion being created beneath it, so that it can be removed from the bonded stack and the latter placed onto the hotplate

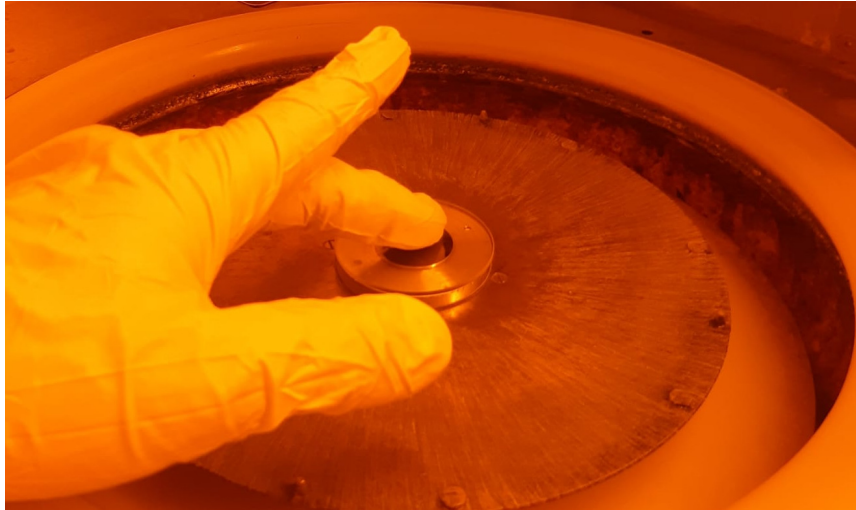


FIGURE B.3: After placing the carrier onto the substrate after spin-coating, apply light pressure to the center of the carrier above the membrane to make contact and remove voids.

(120 °C for 180 s).

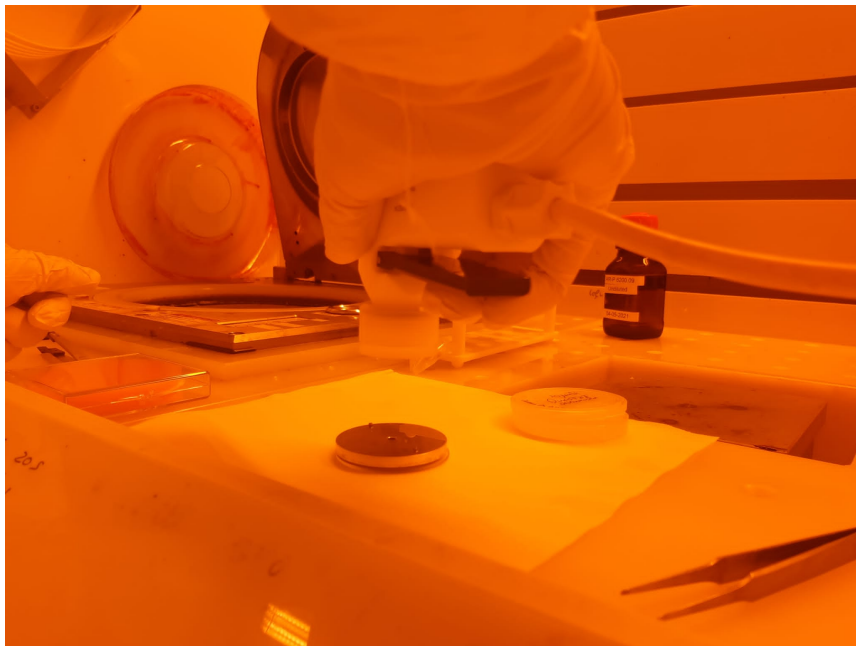


FIGURE B.4: Reverse-blow nitrogen through the mount to detach it from the membrane and flatten the latter against the carrier before baking.

With the Al-mount and spacer the procedure is equivalent to the one with spacer above. If no spacer is used and the substrate is thicker than 10 μm , thermal-expansion debonding can be attempted (fig. B.5). In that case, place the carrier onto the membrane while the latter is still attached to the mount on the spin-coater and apply light pressure. Now take the stack off the spin-coater, flip it and place it on the hotplate at 120 °C. A few seconds later an audible noise will let you know the mount is ready to

be picked up. Use two pairs of tweezers to do so, since the mount may already have reached a high temperature.

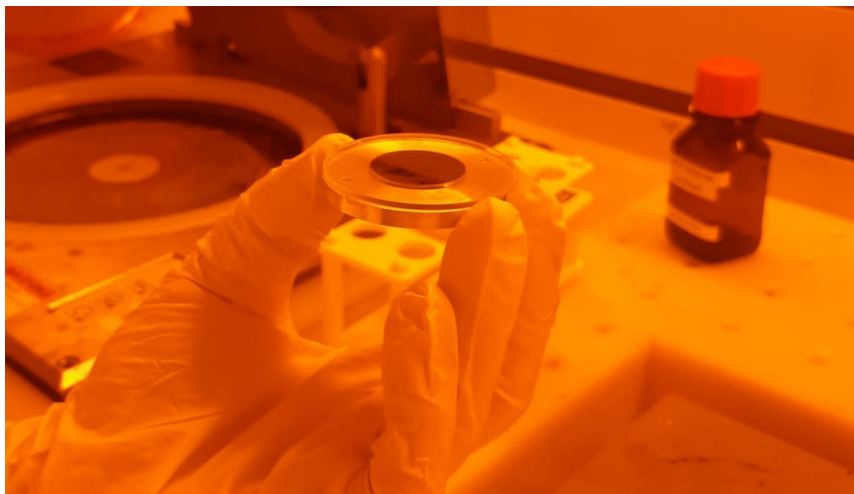


FIGURE B.5: After picking up the mount with membrane and carrier attached, flip it and place it onto the hotplate for baking the PMMA and releasing the mount from the membrane.

Continue to bake the PMMA for another three minutes.

Sometimes, residual PMMA will be visible on top of the bonded membrane, especially around its circumference. If this is the case, prepare a program on the spin-coater with open lid, and spin the carrier with membrane facing upwards at 100-300 RPM. Make sure the center of rotation aligns with the center of the membrane. Take a squirt-bottle of acetone and another of IPA. Start with squirting acetone exclusively to the center of rotation (the membrane) in a continuous stream for about 10-15 s and without a break switch to squirting with IPA at the same location, for another 10-15 s. Stop the spin and assess the situation, if not all residue was removed, repeat the procedure. If the membrane is clean, dry it with N_2 from a great distance. Now a proper bond should be obtained.

SCIL-Imprint

Prepare the SCIL-imprint station, make lots of room for all the equipment. Use a 20 mm thick copper plate (or something comparable) as a sturdy, solid backing. Apply a few droplets of IPA to the copper and place a clean 4" standard wafer onto the copper. Let the IPA evaporate to direct-bond the std-wafer to the copper, or move it around a little to accelerate the process. Acquire the sol-gel and let it warm to room temperature for at least 30 min, then transfer it to a single-use syringe and apply a 200 nm-filter cap to the syringe. Make sure to remove most of the air in the syringe after filling it. Prepare the SCIL stamp for imprint by cleaning it with water, ethanol, and water once more, before blow drying it carefully and completely.

Get ready for the imprint, where everything needs to happen consecutively without breaks. Place the carrier with substrate directly onto the spin-coater and spin the sol-gel for 10 s at 2400 RPM for Spinodal, with 1000 RPM/s acceleration and open bowl. As soon as the process is done, move the substrate onto the std-wafer and center it. Now take the glass carrier holding the stamp and flip it, so that the stamp

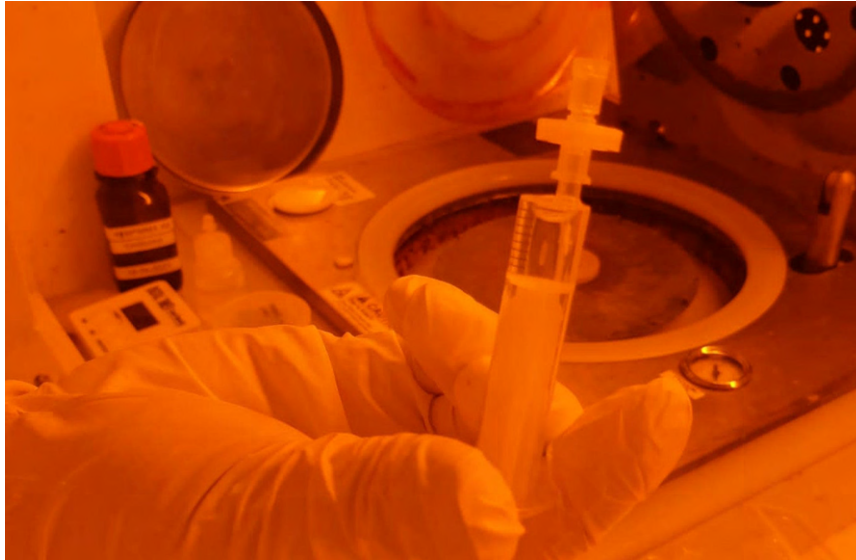


FIGURE B.6: Sol-gel filled into a syringe with $0.2\ \mu\text{m}$ filter cap. Remove as much air as possible

is facing the substrate. Find the pattern on the stamp by tilting until diffraction reveals it, then use this angle to align the pattern above the substrate and lower the stamp onto it.

Perform the "SCIL-motion", by pressing a finger (preferably thumb) onto the patterned area beginning at one edge, then rolling the finger towards the opposite side. When it can anatomically roll no further, lift it and repeat the motion from about half-way of the last rolling distance. Repeat these steps until the far edge of the pattern is reached. Now start over from the first edge and repeat the procedure with slightly increased pressure about 2-4 times, or until no air bubbles remain.

Leave everything as it is after the last repetition and start the time of 9 min for evap-

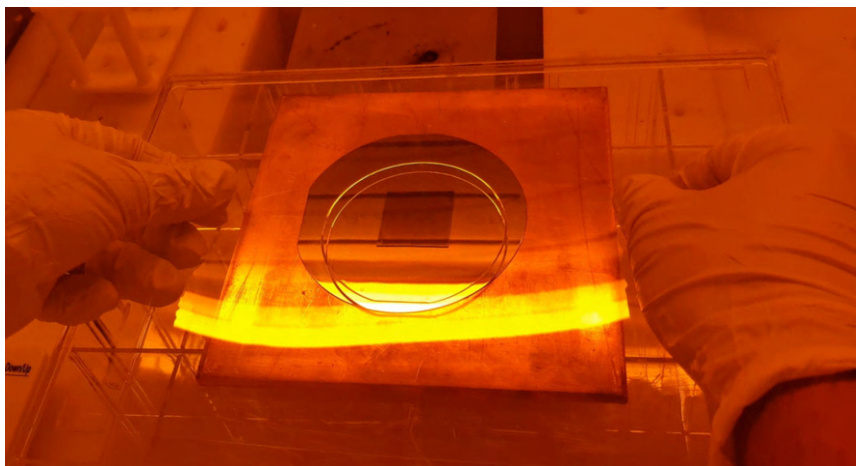


FIGURE B.7: Align the stamp and the pattern on it with the substrate on the SCIL imprint station.

oration.

Separating the stamp from the substrate is done by picking up the stamp from its willow-glass carrier and flipping it over, so that the substrate faces upwards. Now bend the glass slightly, which will cause an edge of the substrate to separate from

the stamp, outside of the patterned area. Insert a pair of closed tweezers into the gap and let the tweezers do the work of separation, then lift the tweezers until one of its legs slips out and comes above the substrate. Now close the tweezers again and pick up the substrate in a single upward motion. Congratulations, you have made just made sub-micron patterns over an area of square centimeters on a membrane!

Reactive-ion etching

Reactive-ion etching is performed as explained in the main text, sec. 3.5. The etcher used for this work requires four-inch substrates, so the smaller samples are bonded to a std-Si wafer carrier using Fomblin oil. Ultimately, if the composition of the porous SiO₂-layer from the sol-gel and the native oxide and their respective etch rates are known, a 2-step RIE could be calibrated for the procedure. At present knowledge, standard duration for the SiO₂ etches using CHF₃/Ar for the sol-gel and Cl₂ for the native oxide are retained and the Si-etch duration calibrated for the desired depth according to the etch speed of 3.4 ± 0.2 nm/s.

An inter-layer of PMMA before spin-coating the sol-gel was used in some experiments, originally for enabling lift-off of the sol-gel residual after etching, but the same also served as an "etch-stop" for the first sol-gel etch (breakthrough etch), since the PMMA is hardly attacked by CHF₃/Ar. The PMMA layer was then opened using an O₂-plasma etch step calibrated at 100 nm/min etch speed, before removing native oxide with chloride. The parameters of the O₂-plasma etch are given in table B.1.

TABLE B.1: Parameters of PMMA-etch using oxygen plasma in a PlasmalabPRO 100 RIE etcher. The etch speed is found in the order of (100 ± 10) nm/min for the structures under consideration.

Step	time (s)	Gases	Flow rate (sccm)	RF (W)	ICP (kW)
PMMA-etch	180	O ₂	25	50	0

Debonding

Debonding thin membranes should be attempted with patience, since depending on the size and thickness of the PMMA-layer, substantial amounts of time maybe necessary to allow access of the solvent to all bonded regions. With up to 24 hrs waiting time, all bonded substrates were found floating on their carriers and could be collected with ease, while premature probing with tweezers against the side of a membrane always led to cracks, when debonding was not fully completed.

Prepare a beaker with a sufficient volume of acetone, such that it does not evaporate to lay bare the substrate over night. Place the bonded stack inside the beaker with the sample facing upwards and the carrier touching the bottom of the beaker. Apply some tinfoil or similar to the top of the beaker to slow the evaporation of acetone and leave it in a fumehood. Return after 24 h.

The bonded stack will look the same upon return, but there is a layer of liquid now at the interface instead of the PMMA. Prepare a second beaker with sufficient volume of isopropyl alcohol and a third one with de-ionized water. Take a pair of tweezers with spatula and transfer the carrier including floating substrate to the beaker with IPA. Try to keep the carrier as horizontal as possible to prevent sliding of the sample - if necessary, tilt the beaker while picking up the carrier and do the same with the

new beaker during immersion of the stack.

Wait some time to allow for the IPA to replace the acetone at the interface, 5-10 min should suffice.

Repeating the procedure from before, pick up the carrier including sample from the IPA beaker as horizontally as possible and move it to the water beaker, but do not submerge it. Instead, tilt the carrier about 20° and slide it into the water beaker at a shallow angle until the surface of the water barely covers the sample. Reverse the motion until the entire sample is above the surface again, then re-approach and repeat the procedure. After a few tries, the surface tension of the water will separate the membrane from the carrier, at which point the former will be free-floating on the water surface, from where it can be recovered with a pair of suitable tweezers or another carrier.

For a new carrier, microscope coverslips have been used successfully to pick up the sample and direct-bond it to the glass through slow evaporation of the water in air afterwards.

The IBC cells on the other hand are much more sturdy and can be picked up with tweezers directly from the IPA bath following the debonding in acetone as described above.

Earlier bonding attempts

There are four different bonding cases displayed in fig. B.8. All direct-bonding attempts show bumps of residual salts in case of water, or air-inclusions in case of IPA, which remain also when a mixture of the two is employed. An attempt which was not investigated further due to incompatibility with subsequent processes is through a reverse application of Peel-and-stick mechanism [83]. The same could become useful, however, where no restrictions on exposed metal during subsequent processing apply. Fig. B.9 shows a bonding attempt without special membrane mount. The

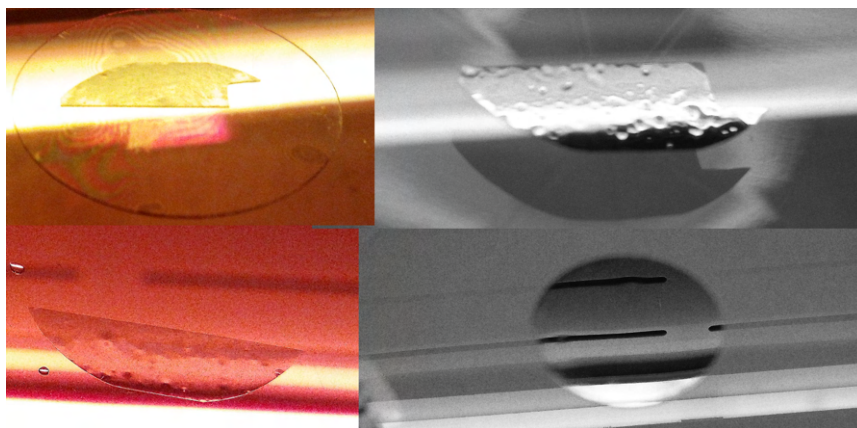


FIGURE B.8: Visual inspection of bonding with **top-left** Fomblin oil; **top-right** IPA, looking through the transparent carrier at the bond interface; **bottom-left** DI-water; **bottom-right** PMMA.

PMMA in this case was spin-coated on a quartz carrier and subsequently a $10\ \mu\text{m}$ -thick membrane placed on it, followed by the baking step. There are deformations visible near the reflection of light on the sample, which rendered this particular route

unsuitable for the SCIL imprint processing and subsequent analysis, since the influence of the deformations cannot be easily resolved.

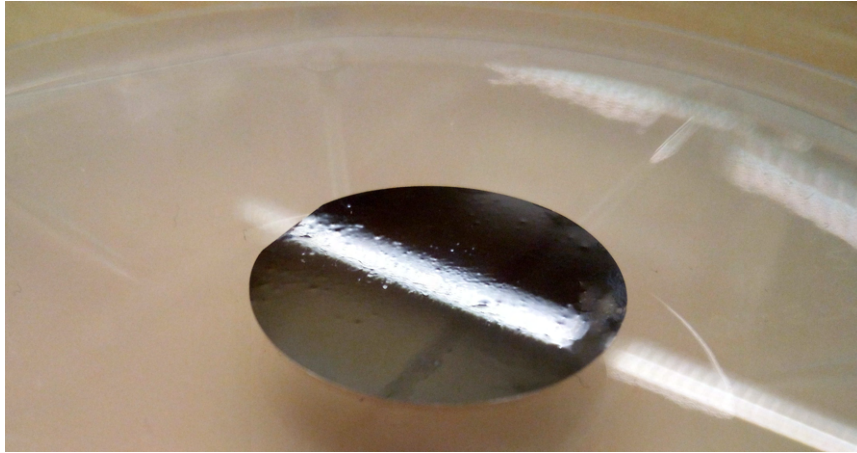


FIGURE B.9: 10 μm -thick membrane bonded to quartz by spin-coating PMMA on quartz and subsequently placing the sample on it, followed by baking. Close to the reflection in the center of the sample, bumps and deformations from degassing PMMA are visible and the bond quality is more comparable to the attempts in fig. B.8.

Appendix C

Analysis of SEM images

In this chapter, the procedure for obtaining Si filling fractions and radial profiles from SEM images is explained. Additional graphs referenced in the main text are also found here.

Taking images with SEM

Data extraction is substantially simplified and most reproducible if one already optimizes contrast and brightness at the time of taking images with the electron microscope.

Obviously, a properly focused image is always necessary, which is most easily accomplished when the sample and its surface exhibit good conductivity.

When the image is properly focused, adjustments of brightness and contrast can help setting a height-threshold later in the processing software. If the contrast is set too high, edges located at the walls connecting top- and lower level of the structure will record the highest brightness values as in fig. C.1. This will lead to an increased contrast also on the top level, potentially rendering certain regions almost as dark as the lower level, thus making the distinction more difficult. A strategy is to start with an intermediate contrast and subsequently lower the brightness until only few places of the structure remain visible. At this brightness value, reducing contrast can lead to a very homogeneous appearance of the top surface with edges no longer being overexposed. Keep the contrast at this value and successively increase brightness again, until the top surface is clearly distinguishable from the valleys of the structure, where the latter remains as dark as possible. Often times this procedure already allows capture of images with proper illumination, but can in any case be aided with minute adjustments of brightness and contrast.

Fig. C.2 shows an SEM-excerpt and its brightness histogram, where only one broad peak is visible. This is an example showing a structured polymeric resist of low conductivity, which is unsuitable for proper analysis. The SEM image showing a honeycomb structure in fig. C.3 was adjusted to exaggerate the effect of splitting the low contrast peak in fig. C.2 into two, one of which is located at the center of the histogram shown in lower fig. C.3 and corresponds to the valleys, while the walls (top level) receive the maximum brightness value. Setting a threshold in this case is substantially facilitated in comparison to fig. C.2.

Processing SEM images with ImageJ

After opening the SEM images with the software [100] or a comparable program, a threshold is set using the brightness histograms shown as examples in fig. C.2 and C.3. When the images were properly adjusted at the time of taking them with the

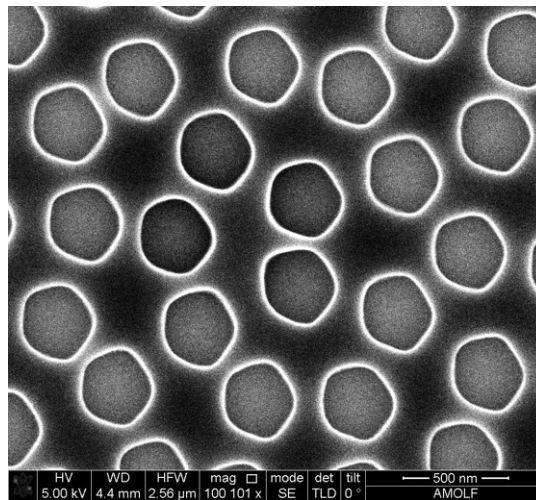


FIGURE C.1: SEM image excerpt showing pentagram-shaped holes etched into silicon. The contrast is set too high, which leads to the edges being most bright and also bright spots occurring inside of the holes.

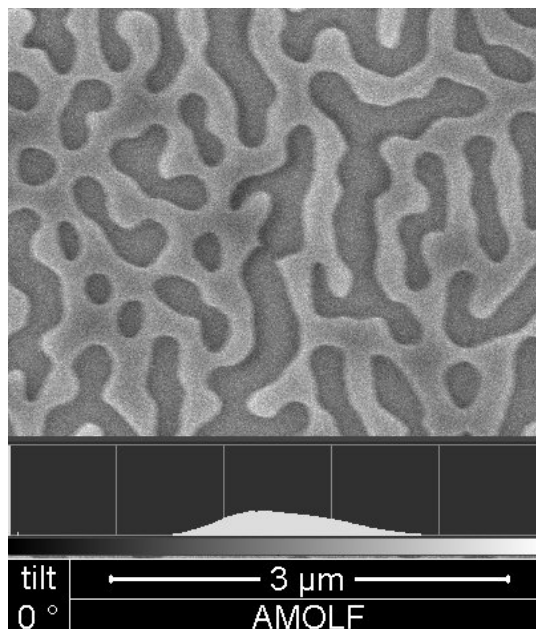


FIGURE C.2: SEM image excerpt including brightness histogram showing no distinguishable levels.

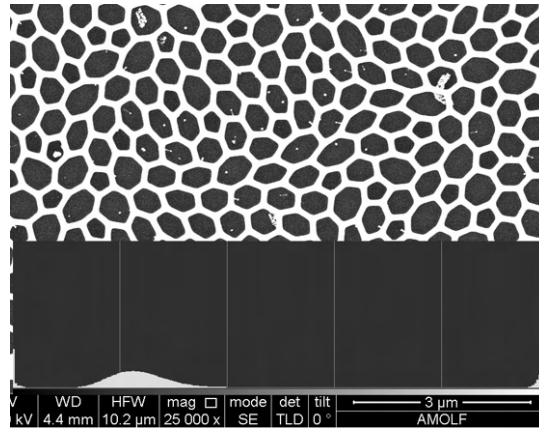


FIGURE C.3: SEM image of honeycomb structures with high brightness and low contrast, making the distinction between top level and valleys easier. A histogram of brightness values shown at the bottom reveals a peak in the center corresponding to the valleys, while the walls are represented at the maximum brightness value.

SEM, two distinct peaks corresponding to the two height levels are visible. The threshold corresponds to two 8-bit values, which enclose the part of the histogram being set to one, while the part of lower brightness outside the threshold receives a value of zero. The upper threshold value is always set to 255, corresponding to the maximum brightness present in the image, while the lower value is chosen somewhere in the center between the peaks. In many cases, the minimum in-between the peaks is broad and flat, such that reproduction of a certain value for the lower threshold is somewhat arbitrary. In order to avoid the introduction of this situation, the threshold setting is performed twice on each image, which also produces an estimated error for the subsequent measurements.

The analysis performed on the images to obtain either filling fractions or structure factors requires circular selections of an area within the images. The circular selections are always taken at the center with equal radii, in order to minimize the discrepancies.

Fig. C.4 and C.5 show screenshots of the software tools for taking the threshold, where in both cases the same image was analyzed, but a different lower threshold value chosen. The difference between the values is low in this example, and both are placed left and right on the steps directly adjacent to the minimum in-between the peaks.

Also displayed in both figures is the circular selection with equal radii of 415 pixels.

Obtaining filling fractions

After setting the thresholds and making the circular selection, the image is cropped to the latter and an automated measurement routine of the program returns the fractions of pixels yielding a brightness value of one, which corresponds to the silicon filling fraction. From both images shown above (fig. C.4 and C.5), the filling fraction amounts to 78.79 % and 76.06 %, respectively. The arithmetic mean of these values is used as the measurement result, while the difference between both values is taken as an estimated error for the measurement.

The filling fraction versus dose factor for the honeycomb structure is given in the

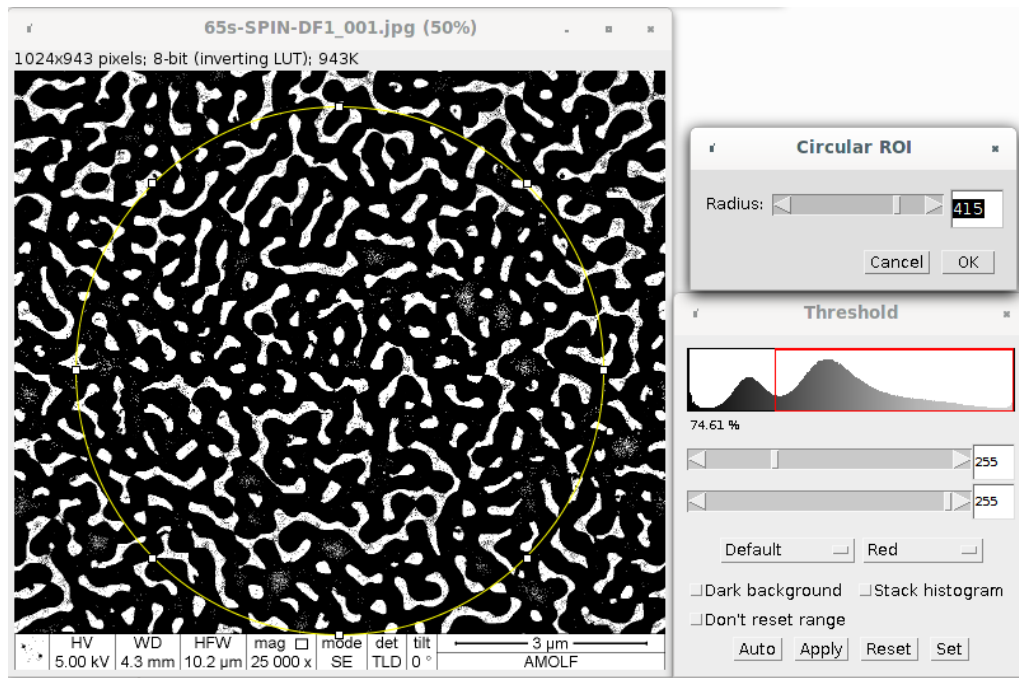


FIGURE C.4: Screenshot of ImageJ while taking the threshold for top level / valley distinction of a Spinodal pattern. The upper threshold is fixed at 255 (max), and the lower is set on the first step left from the minimum between the brightness peaks.

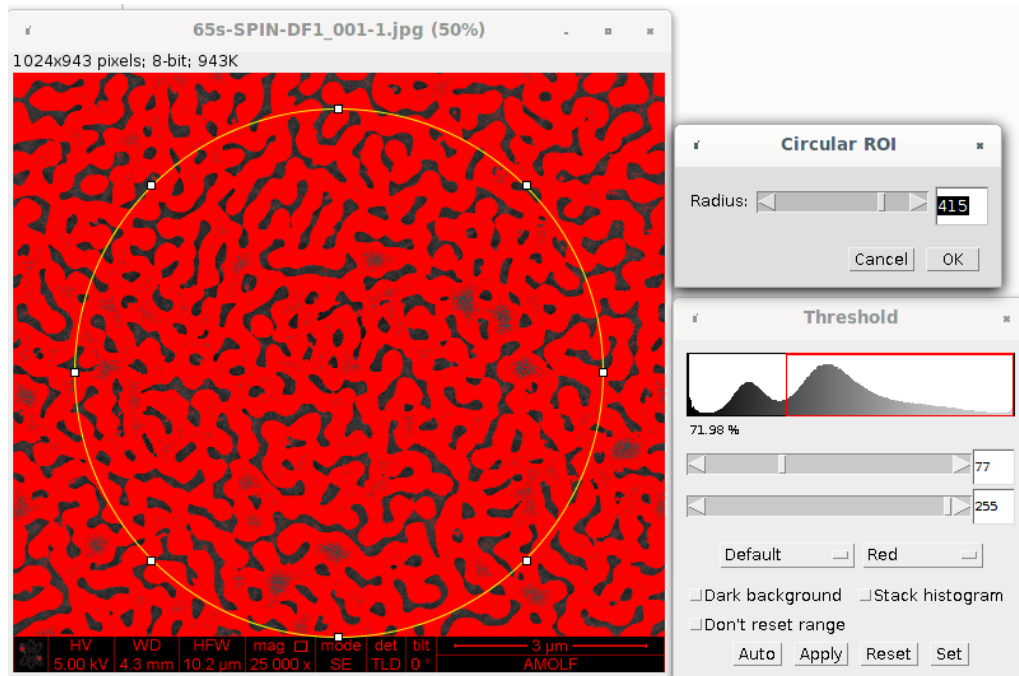


FIGURE C.5: Screenshot of ImageJ while taking the threshold for top level / valley distinction of a Spinodal pattern. The upper threshold is fixed at 255 (max), and the lower is set on the first step right from the minimum between the brightness peaks, in order to gauge the error of this method. Note that the top level in this image is highlighted in red.

main text in fig. 3.3 and for the remaining structures found in the graphs below, fig. C.6 - C.8.

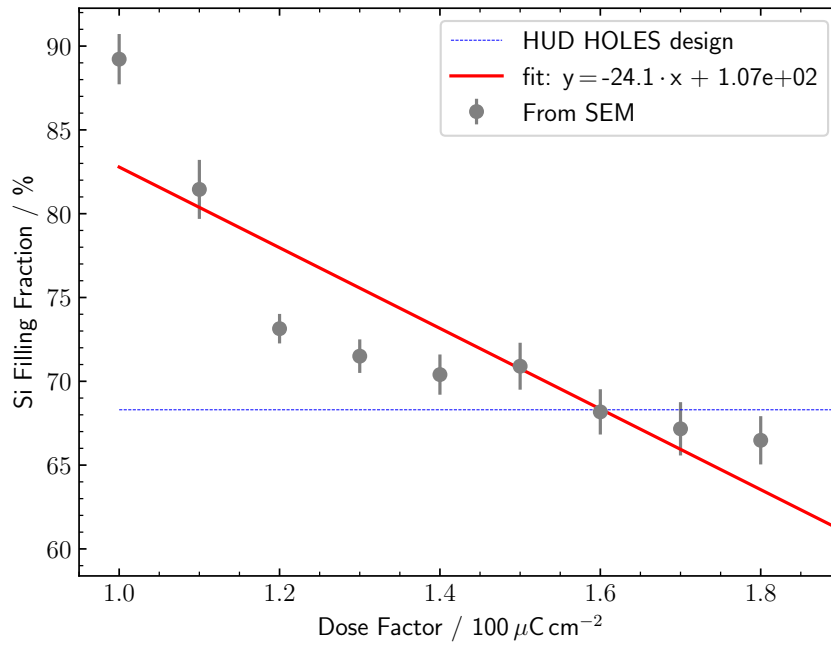


FIGURE C.6: Silicon filling fraction of HUD Holes structure for different charge dosages ranging from (100 – 180) $\mu\text{C}/\text{cm}^2$. Column mode: MC60.

Obtaining structure factor

With a threshold taken and the image cropped to a circular selection, a Fourier-transformed image using an included FFT algorithm can be obtained. For the calibration of spatial frequencies, both the real pixel width in meters and the pixel-size of the cropped image are needed. ImageJ allows to set a length calibration, which facilitates reading values in the unit of meters directly before and after the Fourier transformation. In the FFT image, the center pixel corresponds to a frequency of $\frac{2\pi}{\infty}$, and its adjacent pixel to $\frac{2\pi}{\text{dimension}}$, the second from the center to $\frac{2\pi}{\text{dimension}/2}$, the third to $\frac{2\pi}{\text{dimension}/4}$, *et cetera*, where the dimension is given from the length in pixels (or calibrated distance) of the previously cropped image.

In order to obtain the radially-averaged profile, another circular selection this time of the FFT-image is required. Next, a plugin for the software [101] is activated, which allows for size-adjustments and positioning of the circular selection, before the averaged-profile is calculated via confirming the selection. If a spatial calibration was used, the unit of this profile is given in (distance/cycle) and in the opposite case the unit is calculated by using the relation between pixels and distance in real space, as outlined above. The structure factors of all patterns used for this work are summarized in fig. 3.7 in the main text. Fig. C.9 below shows an extracted radial profile from a honeycomb image in the software. For the structure factors presented in the main text, the dual image processing was omitted, and instead the lower threshold value set to the 8 bit number representing the center minimum between the peaks of top level and valleys. In order to estimate the error of the structure factor method, the dual image method is performed on the Spinodal structure at DF=1.4, which shows about the largest error of the filling fraction determination among all patterns

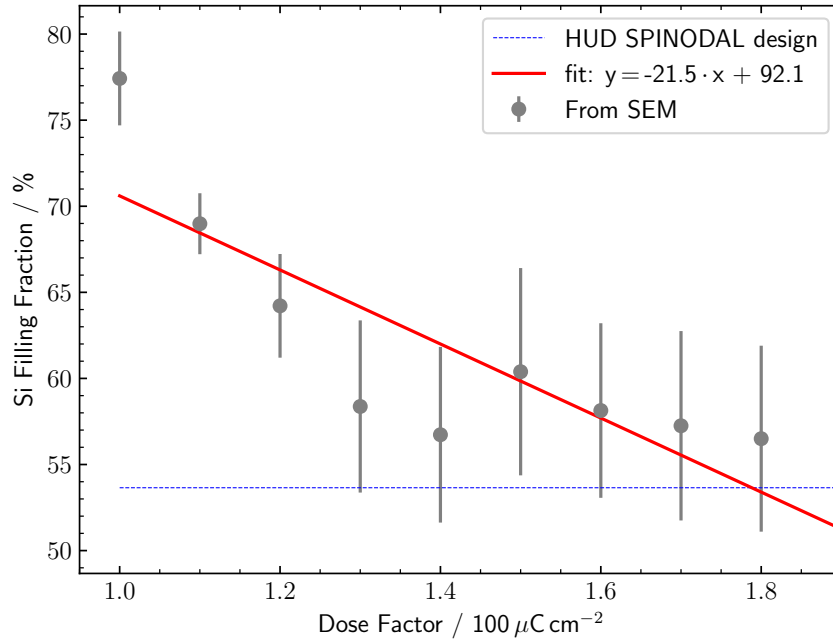


FIGURE C.7: Silicon filling fraction of Spinodal structure for different charge dosages ranging from $(100 - 180) \mu\text{C}/\text{cm}^2$. Column mode: MC60.

as shown in fig. C.7. From these two images, an upper limit for the error of the radial profile is assumed, which amounts to $\pm 1\%$ for the second figure of merit (3.1) with respect to the design, and $\pm 1.4\%$ for the third FOM with respect to the gate function, as seen in the respective graph in fig. C.10.

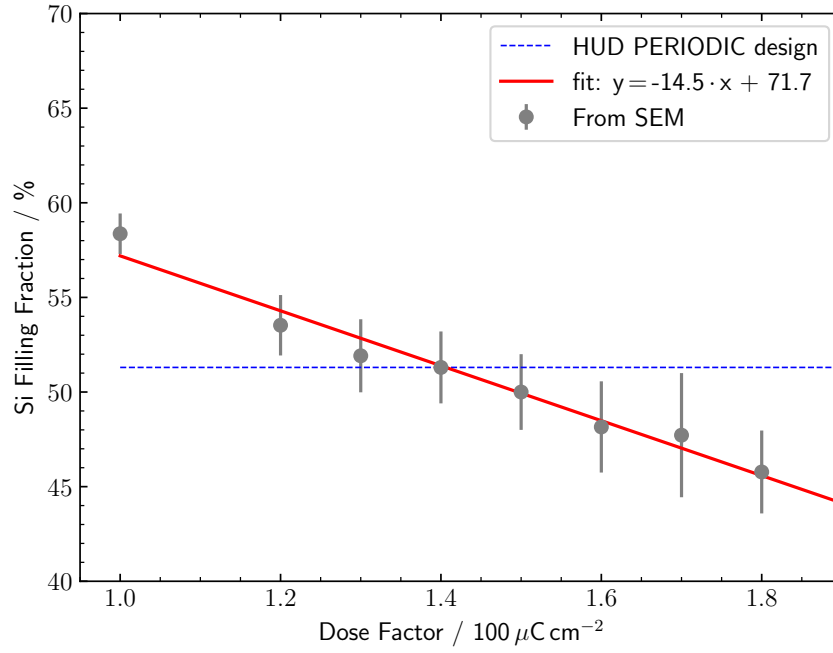


FIGURE C.8: Silicon filling fraction of optimized periodic structure for different charge dosages ranging from $(100 - 180) \mu\text{C}/\text{cm}^2$. Column mode: HMC40.

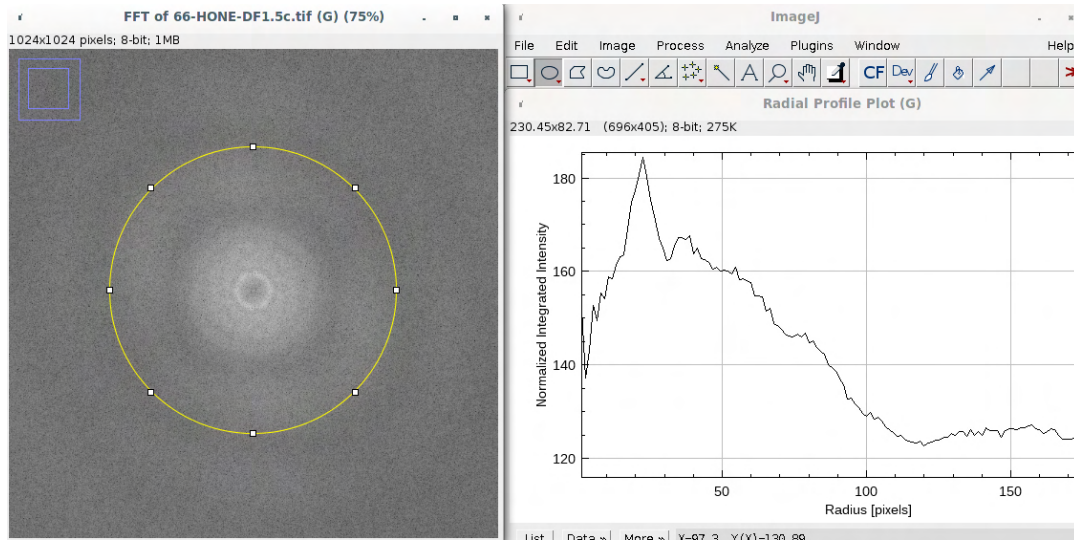


FIGURE C.9: Fourier-transformed SEM image of a honeycomb structure (left) and from it the radially-averaged profile (right) extracted using a plugin [101] for the ImageJ [100] software.

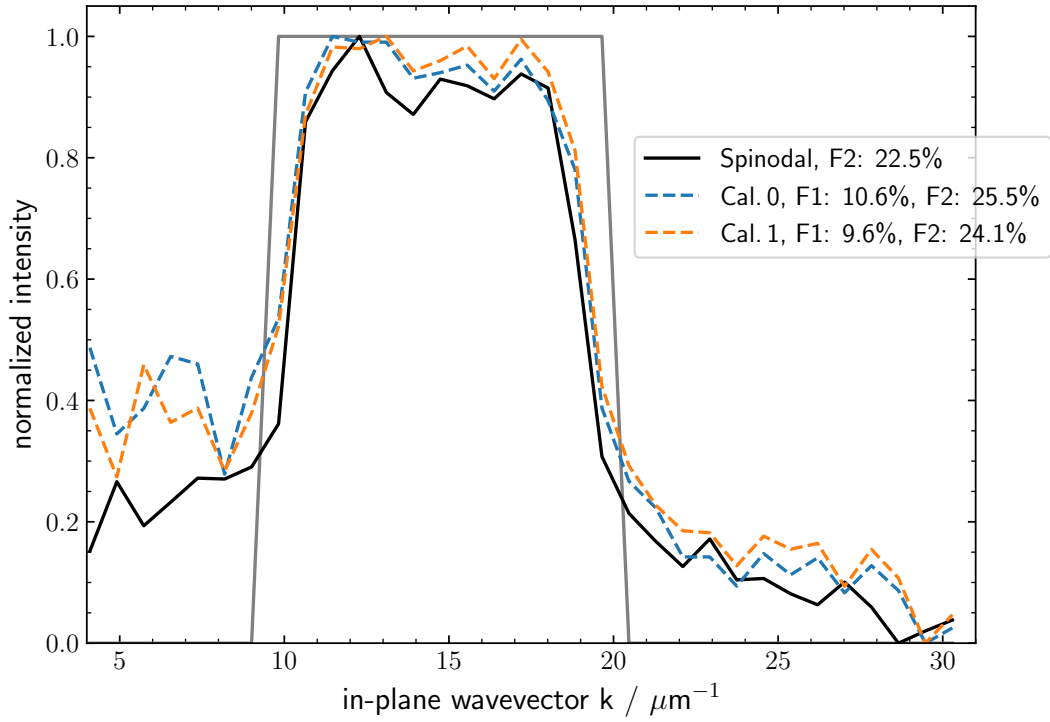


FIGURE C.10: Estimation of the error for determining the structure factor via the SEM method. The dual images produced according to the section about filling fraction above are compared to the design values using the figures of merit, where Cal. 0/1 correspond to the min/max values for the threshold setting. The Spinodal pattern is chosen at a dose of 1.4, which shows among the largest error in the filling fraction determination.